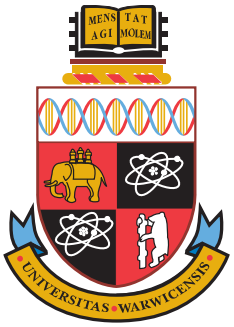

QUANTITATIVE ANALYSIS OF CHLOROPLAST PROTEIN TARGETING

Michael Kok Keng Li

Submitted to the University of Warwick

for the degree of

DOCTOR OF PHILOSOPHY

Research carried out within the following departments

MOLECULAR ORGANISATION AND ASSEMBLY IN CELLS

Doctoral Training Centre

Department of Biological Sciences

Mathematics Institute

Centre for Scientific Computing

September 2009

Preface

The final five months of the writing of this thesis were spent in Hayes, London Borough of Hillingdon while employed at the European research laboratories of a large information technology group of companies with extensive experience in supercomputing. It was my work undertaken during the course of this thesis that made the appointment possible, and I hope the non-confidential portion of the experience gained has resulted in a better rounded piece of work.

Michael Li, Hillingdon 2009

Data from this thesis has been published in

- E. Vladimirou, **M. Li**, C. P. Aldridge, L. Frigerio, M. Kirkilionis and C. Robinson. "Diffusion of a membrane protein, Tat subunit Hcf106, is highly restricted within the chloroplast thylakoid network", *FEBS Letters*, **583**:3690–3696, **2009**.
- M. Kirkilionis, M. Domijan, M. Eigel, E. George, **M. Li** and L. Sbano. "A definition of cellular interface problems", *Membrane Computing. Lecture Notes in Computer Science*, **5391**:36–62, Springer-Verlag, **2009**.

The manuscript "Key influence of the thylakoid signal peptide on diffusion and targeting of a Tat substrate in chloroplasts" is in preparation.

Contents

Acknowledgements

I would like to thank my supervisors Colin and Markus for their guidance and support over the last few years, Alison and all the hard working people who drive MOAC forward, and a whole list of people too numerous to name (a great many people from Biological Sciences, the Centre for Scientific Computing, the Mathematics Institute and MOAC).

- Funding from **Engineering and Physical Sciences Research Council** (EPRSC) grant EP/C512863/1, *"Doctoral Training Centre - University of Warwick"* (held by Professor Alison Rodger).
- Equipment from **Biotechnology and Biological Sciences Research Council** (BBSRC) grant BB/C00437X/1, *"Determination of the spatial and temporal parameters governing protein translocation pathways"* (held by Professor Colin Robinson, Dr. Markus Kirkilionis and Dr. Lorenzo Frigerio).
- HPC facilities and support from the **Centre for Scientific Computing** (CSC) at the University of Warwick.
- Software from the **Free Software Foundation, Inc**; contributors to the Linux kernel; **Gentoo Foundation, Inc**; **Canonical Ltd**; **Argonne National Laboratory** and **Kitware, Inc**.

Declaration

With the exception of clearly indicated collaborative research, this thesis is the candidate's own work and has not been submitted for a degree at another university.

Attention is drawn to the fact that the copyright of this thesis rests with its author. This copy of the thesis has been supplied on condition that anyone who consults it is understood to recognise that its copyright rests with its author and that no quotation from the thesis and no information derived from it may be published without the author's written consent.

The right of Michael Li to be identified as author of this work has been asserted in accordance with the Copyright, Designs and Patents Act 1988.

Abstract

This thesis presents the first use of the **Partition of Unity Method** in quantifying the spatio-temporal dynamics of a fluorescent protein targeted to the **chloroplast twin-arginine translocation** pathway.

The **fluorescence loss in photobleaching** technique is applied in a modified fashion to the measurement of substrate mobilities in the chloroplast stroma. Our *in vivo* results address the two suggested protein targeting mechanisms of membrane-binding before lateral movement to the translocon and direct binding to the translocon.

A **high performance computing C/C++ implementation** of the Partition of Unity Method is used to perform simulations of fluoresence loss in photobleaching and allow a compelling comparison to photobleaching data series. The implementation is both mesh-free and particle-less.

List of Figures

List of Tables

Part I

Introduction and Preliminaries

Chapter 1

Introduction

This thesis advances chloroplast protein targeting research by looking at the largely neglected spatio-temporal behaviour of the protein targeting substrate *in vivo* and reports the application of advanced computational mathematics to the study of fluorescence microscopy data. Mathematics and computer simulation are increasingly used to give a quantitative treatment of dynamic biological processes such as protein targeting and our research takes this approach.

1.1 Chloroplast Protein Targeting

Protein targeting, the mechanism used to transport a protein from one location to another, is essential for all living things and is important in the vital metabolic processes; including both photosynthesis (Cline and Henry, 1996) and cellular respiration (Neupert and Herrmann, 2007; Subramani et al., 2000). In this thesis, we have only addressed protein targeting in the chloroplast, the plant organelle responsible for photosynthesis. Proteins are synthesized on ribosomes as nascent polypeptide chains that may need to undergo various modifications, perhaps at an intermediate location, before arriving at the final destination where the protein performs its function. (Wickner and Schekman, 2005)

Chloroplast protein targeting is of special interest as chloroplasts are believed to originate from endosymbiotic ancestors of cyanobacteria. Chloroplasts have two envelope membranes separating the interior of the organelle from the cytosol. These two envelope membranes surround the internal photosynthetic membranes: the thylakoids. (Staehelin, 2003)

The chloroplast has a reduced genome (Sugiura, 1989; Race et al., 1999; Leister, 2003) and must import a large proportion of its proteins from the plant cell cytosol (Soll and Schleiff, 2004). Proteins are targeted to the chloroplast by an N-terminal polypeptide extension, a transit peptide, which allows interaction with proteinaceous components in the chloroplast

envelope. Translocation into the chloroplast is dependent on nucleotide triphosphates for energy (Flügge and Hinz, 1986). Proteins destined for the chloroplast may end up in one of six compartments (Cline and Henry, 1996; Keegstra and Cline, 1999)

1. outer envelope membrane
2. intermembrane space (Vojta et al., 2007)
3. inner envelope membrane
4. chloroplast stroma
5. thylakoid membrane
6. thylakoid lumen

Several pathways are present for the sorting of proteins to and across the thylakoid membrane as shown in figure 1.1. There are currently two known pathways, the Sec and Tat pathways, for soluble proteins targeted to the thylakoid lumen; and two, the signal recognition particle (SRP) dependent pathway and the "spontaneous" insertion pathway, for thylakoid integral membrane proteins. (Jarvis and Robinson, 2004) Nuclear-encoded proteins that function in the thylakoid lumen must be synthesized with a bipartite N-terminal polypeptide extension: a transit signal, for entry to the chloroplast, followed immediately by a second signal peptide for sorting within the chloroplast (Mould et al., 1991b; Cline et al., 1992). No consensus sequence has been identified in the stromal targeting signal which

range in length from 30 to in excess of 100 amino acid residues (Keegstra and Cline, 1999).

1.2 Tat Cell Biology

Our primary interest is the twin-arginine translocation (Tat) pathway, named for the highly conserved twin-arginine motif in the signal peptide (Chaddock et al., 1995). The finding that the precursors to the 33 kDa and 23 kDa subunits (pre33k and pre23k respectively) of the photosynthetic oxygen-evolving complex have different requirements for import into isolated thylakoids (Mould et al., 1991a; Cline et al., 1992) led to the recognition that there were multiple mechanisms for translocation across the thylakoid membrane (Cline et al., 1993; Robinson and Klösgen, 1994).

Stromal extract and ATP were found to be required for import of pre33k into isolated thylakoids whereas import of pre23k did not require stromal extract or ATP but instead relied on the proton gradient, ΔpH, component of the proton motive force across the thylakoid membrane. (Mould et al., 1991a; Cline et al., 1992)

1.2.1 Twin-Arginine Signal Peptide Motif

It was soon recognized that signal peptides targeting the novel ΔpH-driven, ATP-independent pathway possessed a twin-arginine motif immediately preceding the hydrophobic region (Chaddock et al., 1995) which further distinguished the Twin-Arginine Translocation pathway of pre23k from the Sec-type pathway of pre33k (Mant et al., 1995). A study of bacterial signal peptides uncovered a consensus (S/T)-R-R-x-F-L-K motif (the amino acid at position marked "x" does not matter) possessed by percursors which bind certain redox cofactors (Berks, 1996) although other properties are important and increasing the hydrophobicity of the TorA signal peptide can re-route the protein to the Sec pathway (Cristóbal et al., 1999). Highly hydrophobic residues, denoted ϕ, in the +2 and +3 positions relative to the twin-arginine motif were shown to be important for import into thylakoids (Brink et al., 1998) leading to the suggestion, when taken together with the consensus motif for bacterial signal peptides of co-factor-binding substrates, of a (S/T)-R-R-x-ϕ-ϕ motif (Cristóbal et al., 1999).

Caveats and exceptions abound when features of the Tat pathway are described. The bacterial consensus motif phenylalanine residue of preSufI; precursor of a protein, SufI, with homology to multicopper oxidases but lacking ten of the 12 consensus copper-binding sites; was seen to be important but conservative substitution with similarly hydrophobic leucine was

possible, and replacement of the glutamine in the +4 position relative to the twin-arginine with the consensus lysine unexpectedly retarded translocation (Stanley et al., 2000). Substitution of the twin-arginine motif of preSufI with "KR" was seen to reduce but not block translocation (Stanley et al., 2000)

1.2.2 Chloroplast and *Escherichia coli* Tat Components

A mutation in the maize gene *hcf106* was found to interfere with the targeting of pre23k (Voelker and Barkan, 1995) and the predicted Hcf106 amino acid sequence was found to be homologous to hypothetical bacterial proteins with homology limited to the single predicted membrane-spanning domain and the approximately 40 residues of the region predicted to form an amphipathic helix (Settles et al., 1997).

The alternative naming of "Membrane Targeting and Translocation" was suggested for the Tat pathway although the implicated *Escherichia coli* three gene operon *mttABC* (Weiner et al., 1998) was later found to have the four genes *tatABCD*, and an unlinked *tatE* gene was identified (Bogsch et al., 1998; Sargent et al., 1998) with translation product TatE overlapping in functionality with TatA (Sargent et al., 1998). The *tatB* gene is homologous to the *hcf106* gene and the *tatA* gene is homologous to a maize *tha4* gene, important for thylakoid assembly (Walker et al., 1999). In contrast,

TatD is a cytoplasmic protein with magnesium-dependent DNase activity but neither over-expression nor deletion (Settles and Martienssen, 1998, unpublished data) had any apparent effect on Tat export (Wexler et al., 2000). The identification of TatC (Mori et al., 2001) allowed homologues to be identified in the cyanobacterium *Synechocystis* PCC6803 and *Arabidopis* leading to the confirmation of cpTatC, the chloroplast TatC, as an important integral membrane protein for the ΔpH-dependent Tat pathway (Mori et al., 2001).

TatA is an 89 amino acid protein with predicted amino-terminal hydrophobic α-helix, to residue 20, joined with a short hinge region to the longer amphipathic helix which extends to residue 42 (Sargent et al., 1998; Lee et al., 2002). It was found that TatA could be truncated by 40 amino acids from the carboxyl-terminus without abolishing translocation (Lee et al., 2002). TatB is a 171 amino acid protein with predicted amino-terminal hydrophobic α-helix, also extending to residue 20, followed by a helical portion extending to residue 81 which is at least partially amphipathic (Sargent et al., 1998; Lee et al., 2002). Truncation of 70 amino acids from the carboxyl-terminus of TatB was possible without abolishing translocation as measured by trimethylamine N-oxide reductase activity of the Tat substrate TorA (Lee et al., 2002). TatC is a 258 amino acid protein predicted to have six transmembrane helices with both the amino-terminus and carboxyl-terminus in the cytoplasm (Sargent et al., 1998). Site-directed mutagenesis has been used to show the cytoplasmic amino-terminus and first cytoplasmic loop of TatC to be particularly important (Buchanan et al.,

2002; Allen et al., 2002).

1.2.3 Chloroplast and *Escherichia coli* Tat Properties

A variety of distinguishing features of the Tat pathway were identified including the ability to transport folded proteins (Creighton et al., 1995; Clark and Theg, 1997; Hynds et al., 1998), the existence of a quality control mechanism (Santini et al., 1998) and the transport of hitchhiker proteins (Rodrigue et al., 1999).

Translocation of Folded Proteins

The intermediate form, after removal of the chloroplast envelope transit peptide, of pre23k was shown to be tightly folded as judged by resistance to the protease trypsin yet still import competent (Creighton et al., 1995). Bovine pancreatic trypsin inhibitor (BPTI) chemically linked to the carboxyl-terminus of a different Tat substrate pre17k, the 17 kDa subunit of the oxygen-evolving complex of photosystem II, was shown to import into thylakoids, and import was blocked when the ionophores nigericin and valinomycin were used to abolish both the ΔpH and $\Delta\psi$, the electrical potential, components of the proton motive force (Clark and Theg, 1997) mimicking an experiment to show unfolding is required for import of a

chimeric substrate with chemically linked BPTI into isolated mitochondria (Jascur et al., 1992).

Dihydrofolate reductase (DHFR) is tightly folded when bound to the inhibitor methotrexate, and the translocation of a Sec-dependent plastocyanin precursor and DHFR fusion across the thylakoid membrane was shown to be blocked when methotrexate was present (Endo et al., 1994). In contrast, the chloroplast Tat pathway was shown to translocate a pre23k-DHFR fusion across the thylakoid membrane even with methotrexate bound (Hynds et al., 1998).

Translocation of Hitchhiker Proteins

The trimethylamine N-oxide (TMAO) reductase, a molybdenum cofactor binding protein, of *Escherichia coli* was found to be translocated across the cytoplasmic membrane by a Sec-independent mechanism and mutations preventing correct cofactor insertion blocked translocation (Santini et al., 1998). A similar quality control mechanism was apparent where the *Escherichia coli* Tat substrate hydrogenase 2 small subunit HybO was found to require the large subunit HybC, which possesses no signal sequence, for co-translocation in a hitchhiker fashion and either subunit alone would remain in the cytoplasm (Rodrigue et al., 1999).

Quality Control and Proofreading

Although the Tat pathway will transport truncated and misfolded dihydrofolate reductase when fused to the carboxyl-terminus of pre23k (Hynds et al., 1998), a number of quality control or proofreading mechanisms are present. The mutual requirement of the HybO and HybC for Tat-dependent export is complemented by the chaperones HybE and HyaE which prevent premature targeting (Dubini and Sargent, 2003) in a manner which relies on the native HybO signal peptide (Jack et al., 2004). Signal peptide binding quality control was also shown for the *E. coli* respiratory enzyme trimethylamine N-oxide reductase, TorA, a Tat substrate with a signal peptide which is bound by the cytoplasmic chaperone TorD to allow efficient cofactor insertion (Jack et al., 2004; Hatzixanthis et al., 2005).

A more direct involvement of the Tat pathway in quality control and proofreading was suggested when TatA/E and TatD appeared to be involved in the degradation of misfolded proteins (Matos et al., 2008, 2009). Cysteine residues involved in binding iron-sulphur ligands were mutated to alanine in the NrfC subunit of the formate-dependent nitrite reductase complex and degradation of these misfolded mutants was thought to be dependent on TatA/E (Matos et al., 2008) and TatD (Matos et al., 2009), but the high rate of protein degradation and turn-over seen was due to differing expression levels and misfolded NrfC is thought to be degraded in a Tat-independent manner (Lindenstrauss et al., 2010).

Integration of Membrane Proteins

The thylakoid integral membrane protein Pftf, with homology to bacterial zinc-dependent protease FtsH, was shown to depend on *hcf106* for insertion into the thylakoid membrane although the twin-arginine of the Pftf precursor signal peptide could be mutated to twin-lysine without affecting integration (Summer et al., 2000).

1.2.4 Chloroplast and *Escherichia coli* Tat Mechanism

The mechanism of translocation is not well understood but appears to be broadly similar in *E. coli* and plant chloroplasts (Robinson and Bolhuis, 2001). A range of studies have looked at the roles of the individual components and complexes to understand the mechanism of translocation.

The *E. coli* genes *tatA* and *tatB* were shown to have different functions as deletion of *tatB* alone was sufficient to block transport of a number of Tat substrates, and *Helicobacter pylori tatA* was able to complement an *E. coli tatA* deletion strain but not a *tatB* deletion strain (Sargent et al., 1999). The roles of *tha4* and *hcf106* were distinguished instead by showing Tat substrate binding to the thylakoid membrane was inhibited by antibodies to Hcf106 but not by antibodies to Tha4, suggesting that Tha4 functions later in the translocation process (Ma and Cline, 2000).

The absence of TatB was shown to result in rapid degradation of TatC suggesting TatC complexes are stabilized by TatB (Sargent et al., 1999). An interaction between TatA and TatB was also demonstrated and large complexes of approximately 600 kDa were isolated by gel filtration (Bolhuis et al., 2000). The TatAB complex found may also have contained TatC as a greater level of purification identified TatABC complexes, solubilized in the detergent digitonin, of approximately 600 kDa containing TatA and TatB in equal amounts but varying amounts of TatA (Bolhuis et al., 2001). TatAB complexes were independently obtained with the same size estimate of approximately 600 kDa and negative stain electron microscopy showed a double-layered ring structure (Sargent et al., 2001). Non-denaturing blue polyacrylamide gel electrophoresis (BN-PAGE) was used to give a smaller size estimate of approximately 370 kDa for the TatABC complex (Oates et al., 2005).

Hcf106 was shown to be important for precursor binding at an early stage of the transport process as antibodies to Hcf106 reduced precursor binding whereas antibodies to Tha4 did not (Ma and Cline, 2000). A cpTatC-Hcf106 complex was found to act as a receptor for Tat substrates and form complexes of around 700 kDa in size which were not associated with Tha4, as found by BN-PAGE and immunoblotting (Cline and Mori, 2001). In agreement with this, site-specific crosslinking was used to show the entire length of the preSufI signal peptide interacted with TatB, only the residues near the twin-arginine motif interacted with TatC and association with TatA was only found when a pH gradient was present (Alami

et al., 2003). Similarly the twin-arginine signal peptide and pH gradient is necessary for recruiting Tha4 to the Hcf106-cpTatC receptor complex (Mori and Cline, 2002).

Unexpected, affinity chromatography purified hexahistadine tagged TatA was found to form complexes over a broad range of apparent molecular weights (de Leeuw et al., 2002) and protease accessibility suggested the carboxyl-terminus is located in the cytoplasm (Porcelli et al., 2002).

At rest in the chloroplast, Hcf106-cpTatC complexes are believed to remain separate from Tha4 complexes until a Tat substrate precursor binds to the Hcf106-cpTatC receptor, in the presence of a pH gradient, and Tha4 complexes are recruited (Mori and Cline, 2002). The situation is believed to be similar in *E. coli* with TatABC complexes containing only a minor amount of TatA separate from the major population of homo-oligomeric TatA complexes (Bolhuis et al., 2001; Robinson and Bolhuis, 2004); or TatBC complexes entirely separate from TatA complexes (Bolhuis et al., 2001; Berks et al., 2005; McDevitt et al., 2006), and that isolated TatABC and TatAB complexes are found with overexpression (Oates et al., 2005) but not at native expression levels (McDevitt et al., 2006).

After Tat substrate translation and co-factor insertion, the Tat signal peptide is believed to be unstructured in an aqueous environment before forming a partially α-helical structure in the hydrophobic environment of the membrane (Miguel et al., 2003).

The membrane binding step, shown to be energy-independent without requirement for soluble factors, was suggested to depend on protein-protein interactions as antibodies to Hcf106 reduced membrane binding and protease treatment of thylakoid membranes abolished binding (Ma and Cline, 2000). Tight interaction of Tat substrates with artificial *E. coli* phospholipid bilayers (Shanmugham et al., 2006) and liposomes, together with the finding of translocase-independent intermediates, suggested a different model with unassisted membrane insertion of the signal peptide, perhaps in a loop conformation (Fincher et al., 1998), as the first step (Hou et al., 2006).

Although Tha4 is only cross-linked to the precursor and Hcf106-cpTatC receptor under transport conditions, reversible assembly of the translocation machinery could also be initiated by the signal peptide without the mature domain (Mori and Cline, 2002). The signal peptide is believed to initiate homo-oligomerization of Tha4 in the thylakoid membrane (Dabney-Smith et al., 2006) and recruitment of TatA in *E. coli*, for which homo-oligomeric complexes of a broad range of sizes are present even without transport (Oates et al., 2005), and both Tha4 and TatA are believed to facilitate translocation perhaps by forming channel of various sizes according to the substrate (Gohlke et al., 2005).

The details of the translocation step remain a mystery and studies reported in the literature propose different possibilities: gated pore, iris-like, gating-pushing, targeting-insertion-opening mechanisms (Brüser and

Sanders, 2003) and cpTatC pulling substrates through a patch of Tha4 (Cline and McCaffery, 2007).

Protease accessibility experiments showed a stromal localization of the carboxyl-terminus of Hcf106 (Settles et al., 1997) and Tha4 (Walker et al., 1999), and a corresponding cytoplasmic localization of the TatA carboxyl-terminus (Porcelli et al., 2002). Notwithstanding the cytoplasmic localization of the TatA carboxyl-terminus, removal of the transmembrane section to form ΔTMS-TatA showed the remaining portion of TatA is able to interact with membrane bilayers and insert into phospholipid monolayers (Porcelli et al., 2002).

Protease accessibility to a carboxyl-terminally positioned, tobacco etch virus protease cleavage site showed the TatA carboxyl-terminus is accessible from both the cytoplasm and the periplasm demonstrating dual localization (Gouffi et al., 2002). Dual localization of the TatA carboxy-terminus was independently confirmed, and site-specific mutagenesis further showed that the TatA amino-terminus is found in the cytoplasm rather than in the periplasm (Chan et al., 2007) as usually assumed. TatA was suggested to have a single transmembrane span resting state, demonstrated using an uncoupler to abolish the ΔpH across the cytoplasmic membrane, with amino-terminus in the cytoplasm and carboxyl-terminus in the periplasm; whereas TatA in the active state was suggested to have two transmembrane spans, so that charged and polar residues can line a water-solvated pore and enable translocation (Chan et al., 2007).

1.2.5 *Bacillus subtilis* Tat Components

The distinction between *tatA/tha4* and *tatB/hcf106* is especially important when considering other organisms with homologues of these genes (Wu et al., 2000; Yen et al., 2002). For example, the Gram-positive bacteria *Bacillus subtilis* possesses two Tat pathways, *tatAdCd* and *tatAyCy* (Jongbloed et al., 2000, 2004). The TatAdCd translocase, which currently only has one known substrate, was demonstrated to translocate the phosphodiesterase PhoD whereas TatCy was not required which suggested *B. subtilis* TatC has substrate specificity (Jongbloed et al., 2000). The TatAyCy translocase, similarly only has one known substrate, was shown to translocate YwbN which has similarity to putative iron-dependent peroxidases (Jongbloed et al., 2004, Appendix S1). Despite having two Tat pathways, PhoD and YwbN are the only two confirmed *B. subtilis* Tat substrates. There are two proteins, QcrA and YkuE, which have signal peptides recognized by the *Streptomyces coelicolor* Tat pathway but these proteins have yet to be confirmed as substrates on either one or both of the TatAdCd or TatAyCy pathways (Widdick et al., 2008).

1.2.6 *Bacillus subtilis* Tat Mechanism

Studies of the *B. subtilis* Tat pathways have suggested a translocation mechanism different from those proposed for *E. coli* and plant chloroplasts.

The TatAd and TatAy proteins have the conserved phenylalanine residue (Phe20) of *E. coli* TatA and the conserved proline residue (Pro22) of TatB (Hicks et al., 2003) leading to the suggestion that TatAd and TatAy perform the function of both TatA and TatB (Jongbloed et al., 2004). Indeed bi-functional mutants of *E. coli* TatA have been created, with suitable mutations made to the amino-terminus of TatA before the transmembrane helix, which allow efficient translocation in the absence of TatB (Blaudeck et al., 2005). In addition to the TatAd population in the membrane; a population of soluble TatAd was found in the cytosol which interacted with the precursor to PhoD, prePhoD, as inferred from co-immunoprecipitation and was proposed to assist in *B. subtilis* Tat-dependent targeting. (Pop et al., 2003). Soluble hexahistadine-tagged TatAd was purified, found to homo-oligomerize as complexes of 150 to 250 kDa in both the absence and presence of TatCd, and experiments with prePhoD suggested soluble TatAd complexes recognize the substrate in the cytosol before transport to the membrane (Westermann et al., 2006). The finding of soluble Gram-positive bacteria *Streptomyces lividans* TatA and TatB added support for the existence of a cytoplasmic population of these proteins (Keersmaeker et al., 2005) but mechanistic models of membrane-bound TatA and soluble TatA are yet to be reconciled.

In contrast to the lower number of proteins currently known to be translocated by the *B. subtilis* Tat pathways, the recent sequencing of the archaea *Halobacterium* species NRC-1 genome (Ng et al., 2000) allowed the systematic search for Tat substrates and it is thought the vast majority of

the halophilic archaea's secreted proteins is folded in the cytoplasm before translocation by the Tat pathway due to the high-salt environment (Rose et al., 2002). The TATFIND program identified 64 putative Tat substrates in *Halobacterium* sp. NRC-1, correctly identified 26 previously reported *E. coli* Tat substrates and a further 8 putative Tat substrates (Rose et al., 2002). Tat signal peptides were recognized using previously identified characteristics such as the hydrophobicity of the uncharged region after the twin-arginine motif (Robinson and Bolhuis, 2001).

1.3 Spatio-Temporal Bioimaging

Most research on the Tat pathway has focused on the biomolecular mechanism of translocation itself and the protein-protein interactions of translocation. In comparison, very little research has been done on the behaviour of the substrate targeted to the Tat pathway and there are many open questions regarding the manner in which Tat substrates arrive at an appropriate site for translocation after all necessary modifications to the substrate.

Chloroplast protein targeting is an inherently spatial process and yet the majority of the research carried out is of a non-spatial, biochemical nature. We use a Tat signal peptide fused to a fluorescent protein to allow *in vivo* visualization of the substrate population by fluorescence confocal microscopy. The citation relationship in figure 1.2 shows the context of

our spatio-temporal approach to Tat protein targeting. Our *in vivo* results complement the *in vitro* evidence for membrane-binding as an early step in the translocation process (di Cola et al., 2005; Hou et al., 2006) and address the importance of the signal peptide on the substrate dynamics before the translocation step.

We use fluorescence confocal microscopy as an analytical tool for observing and perturbing the spatial distribution of fluorescent proteins over a short interval of time at the micron-scale in common with techniques shown in figure 1.1. Working at this length scale is challenging for light microscopy and we take care to avoid unwanted damage from prolonged imaging. This length scale is also too coarse to resolve structures visible by electron microscopy at the nano-scale and we are unable to resolve the highly convoluted thylakoid membrane structure and its influence on protein targeting. This study attempts to take an *in vivo* approach without probing the movement of individual molecules as would be possible for single-particle tracking and other invasive techniques shown in table 1.4.

1.3.1 Fluorescence Microscopy Techniques

Fluorescence microscopy is the use of fluorescent molecules, which emit light when excited with appropriately chosen electromagnetic radiation, in order to visualize structures that may not be clearly discernable by

reflected or transmitted light in conventional light microscopy. Fluorescence microscopy may use the same arrangement of mirrors and lenses as in conventional light microscopy but sophisticated electronics, and both computer hardware and software are usually present to allow precise control of lasers and sensors in acquiring digital images from the analogue emission of fluorescence from fluorescent molecules.

Techniques for Localization and Measurement of Dynamics

The earliest use of fluorescence microscopy was with small molecules such as fluorescein which can be used to label a protein of interest directly or used to label antibodies which bind to a protein of interest. (Frye and Edidin, 1970) More recently, molecules such as the Green Fluorescent Protein (GFP) (Tsien, 1998), from the jellyfish *Aequorea victoria*, and its deriatives have been used to study protein dynamics *in vivo*. (Lippincott-Schwartz et al., 2001)

A number of fluorescence microscopy techniques have been employed ranging from observation of the intermixing of fluorescent molecules (Frye and Edidin, 1970) to the use of an effect known as photobleaching. Photobleaching is the use of a high power laser setting to abolish the fluorescent property of a molecule and this effect can be used on steady-state distributions to get more information by observation of fluorescence redistribution. (White and Stelzer, 1999)

One of the earliest and most popular techniques of fluorescence microscopy which uses the photobleaching effect is the Fluorescence Recovery After Photobleaching (FRAP) technique (Peters et al., 1974). A region of the sample is selected to be the bleach region and the average fluorescence intensity is measured during the course of the experiment. A high intensity laser setting rapidly depletes the fluorescence in within the bleach region and fluorescence redistributes according to interactions within the sample of interest. Typically the biological data are compared to diffusion within idealized geometries, such as circles or spheres (Soumpasis, 1983), or more recently comparisons may be made to computer simulations, perhaps employing actual geometries from the data (Sbalzarini et al., 2005).

The Fluorescence Loss In Photobleaching (FLIP) technique again uses a high intensity laser to deplete fluorescence in a small region but the aim is to observe the redistribution of fluorescence in order to determine the connectivity of biological compartments (Cole et al., 1996). An alternative to the FLIP technique is the use of photoactivatable GFP (PA-GFP) allowing selective activation of a small population of PA-GFP using high intensity ultraviolet illumination so that the redistribution of the marked population may be observed (Patterson and Lippincott-Schwartz, 2002).

Both FRAP and FLIP have counterparts, respectively fluorescence photobleaching recovery (FPR) and continuous fluorescence microlysis (CFM) summarized in table 1.1, more suited to a fixed laser rather than a fluorescence microscope. The approach taken in this thesis is closely related to

CFM (Peters et al., 1981) and FLIP (Cole et al., 1996) techniques.

The tendency for fluorescence molecules to be influenced by their surroundings is used by the Fluorescence Lifetime Imaging (FLIM) technique to create a map of where fluorescence remains present for long lengths of time and regions where fluorescence is lost very quickly in order to infer properties about binding interactions and the local environment in the sample (Lakowicz et al., 1992). Moving even further away from fluorescence microscopy for capturing static images, the Fluorescence Correlation Spectroscopy (FCS) technique measures fluorescence fluctuations in femto-litre volumes and uses statistical physics to extract quantitative information about the dynamics of the fluorescent molecules under observation (Maiti et al., 1997; Haupts et al., 1998).

Techniques for Detecting Co-Localization and Proximity

When the interaction of two particular proteins is of interest, both proteins may be expressed fused with variants of GFP, such as Cyan Fluorescent Protein (CFP) and Yellow Fluorescent Protein (YFP), so that the emission of the donor fluorophore, for example CFP, excites the acceptor fluorophore, for example YFP, in the Fluorescence Resonance Energy Transfer (FRET) technique which allows the proximity of the proteins of interest to be determined (Gadella et al., 1999).

Another approach to test for co-localization is the Bi-Fluorescence Complementation technique (BiFC) which detects co-location of two proteins of interest by fusing two non-fluorescent fragments of a fluorescent protein to the two proteins so that co-localization and interaction allows complementation to result in a detectable fluorescent protein (Hu et al., 2002; Walter et al., 2004).

Whereas most photobleaching techniques measure in a small part of the domain, we will bleach in a spot and measure the depletion in the whole domain and we consider this a slight modification of FLIP as it has been described up to the present. Such a whole chloroplast measurement is vital given the heterogeneous nature of the chloroplast and the stromal compartment. In the mature techniques such as those in table 1.1 there is often a collection of common analyses that may be applied, examples are shown in tables 1.2 and 1.3.

1.4 Spatial Modelling and Biological Simulation

Spatio-temporal modelling is the emerging approach to the analysis of protein transport and targeting processes. Much of our biological knowledge of protein targeting comes from inherently non-spatial *in vitro* biochemical data but the recent use of fluorescent proteins for localisation of proteins involved in protein targeting has encouraged the application of numerical

Figure 1.1: Chloroplast import and targeting pathways. Immature forms of chloroplast proteins are shown at the top, outside the chloroplast, and labelled with their functional destinations. The transit peptides are shown as grey bars and these allow entry to the chloroplast by the translocons at the inner and outer chloroplast envelopes (the Toc and Tic complexes). The stromal processing peptidase is shown as scissors cleaving the grey transit peptide. Various methods of membrane protein insertion into the inner and outer envelopes are shown, and a protein destined to reside in the stroma is depicted as folded on entry. The four thylakoid-related pathways are shown with the Sec and Tat pathways for lumenal proteins, and the SRP and spontaneous pathways for thylakoid membrane proteins. The Sec signal peptide is shown in light blue to match the Sec translocase; and the Tat signal peptide is shown in red to match the Tat translocase. Both the Sec and Tat signal peptides are cleaved by the lumenal thylakoid processing peptidase shown as scissors. The SRP pathway is shown as a GTP-dependent pathway. Figure reproduced from Current Biology (Jarvis and Robinson, 2004).

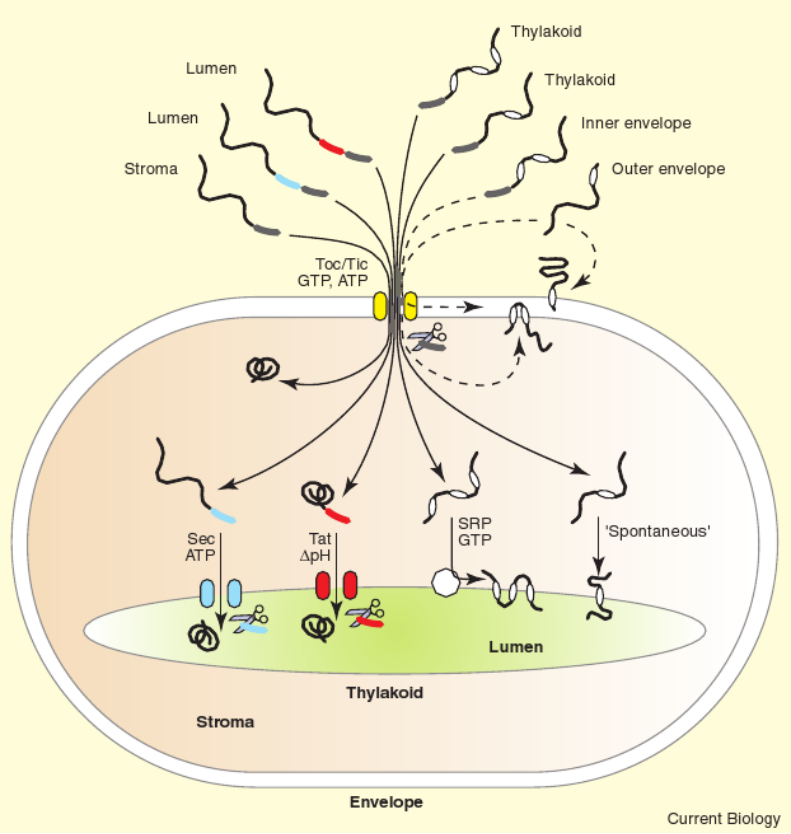

Figure 1.2: Citation relationship for Tat and fluorescent proteins. Current analyses are static rather than dynamic. In contrast to some areas of biology, there has been no attempt at spatial modelling and simulation for the Tat pathway and this is a key motivation for the current work.

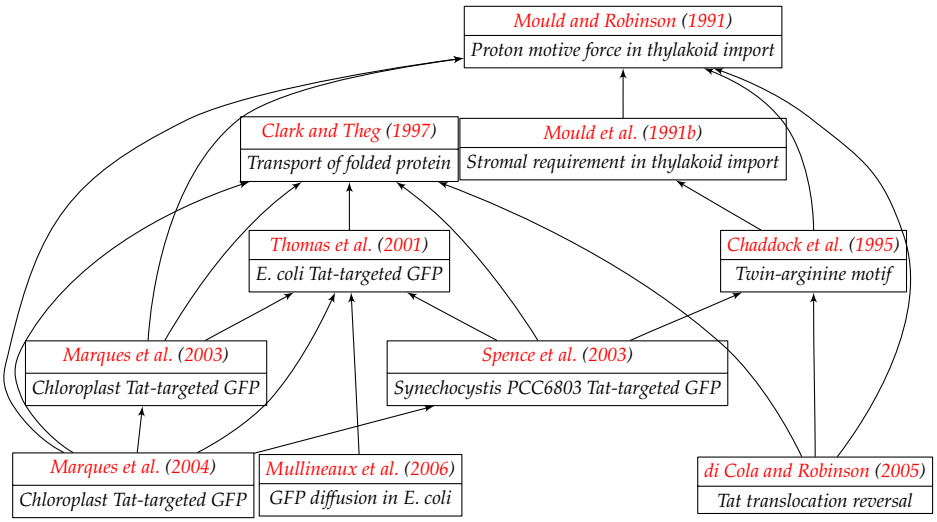

Table 1.1: Fluorescence mobility and photobleaching techniques. New techniques and novel modifications of old techniques are developed to tackle a specific biological application before further refinement and discussion of wider applications. The work presented in this thesis is an example of an application-driven employment and adaptation of techniques with a greater emphasis on spatial inhomogeneity in protein targeting.

Name	Distinguishing features	Reference(s)
(unnamed)	observation of fluorophore intermixing	Frye and Edidin (1970)
Fluorescence recovery after photobleaching (FRAP)	bleach region of varied sizes and shapes	Peters et al. (1974); Lopez et al. (1988)
Fluorescence photobleaching recovery (FPR)	spot bleach, resolving flow and diffusion processes	Axelrod et al. (1976)
Continuous fluorescence microphotolysis (CFM)	prolonged spot bleaching	Peters et al. (1981)
Fluorescence loss in photobleaching (FLIP)	fluorescence loss outside bleach region measured	Cole et al. (1996)
Line-scanning microphotolysis (LINESCAMP)	line bleaching and monitoring for high temporal-resolution	Wedekind et al. (1996)

Table 1.2: Photobleaching analysis and determination of mobility. There is an emphasis on deriving numbers, some with and some without intervals to indicate the uncertainty, as the final output of the analysis. The nature of our experimental system requires us to take a more explorative approach rather than deriving a number from some lesser, as low as three, or greater number of data points.

Approximation	Reference(s)
Spherical diffusion and Legendre polynomials expansions	Peters et al. (1974)
2D planar diffusion, three point fitting, and scaling of variables	Axelrod et al. (1976)
Uniform circular laser beam	Soumpasis (1983)
Analytical solutions and finite differences	Lopez et al. (1988)
Constrained diffusion	Feder et al. (1996)
3D finite difference and line-scanning	Kubitscheck et al. (1998)

Table 1.3: Continuous photobleaching – selected articles. The technique of continuous photobleaching makes a measurement in a small part of a particular sample, so care must be taken when the sample is highly inhomogeneous and the measurement at one location may not be representative of other locations or other samples.

Title	Reference
Continuous fluorescence microphotolysis: a sensitive method for study of diffusion processes in single cells.	Peters et al. (1981)
Analyzing intracellular binding and diffusion with continuous fluorescence photobleaching.	Wachsmuth et al. (2003)
Derivation of a closed form analytical expression for fluorescence recovery after photo bleaching in the case of continuous bleaching during read out.	Endress et al. (2005)
Continuous photobleaching in vesicles and living cells: a measure of diffusion and compartmentation.	Delon et al. (2006)
Continuous fluorescence microphotolysis and correlation spectroscopy using 4Pi microscopy.	Arkhipov et al. (2007)

methods such as the finite difference and finite element methods. For our simulations later, we will make use of the reported diffusion coefficients shown in table 1.4 although we keep in mind that many such results rely on methods developed for expedience: an example being curve fitting methods using a small numbers of graph points. Some of the concerns and recommendations regarding assumptions made in expedient methods are shown in table 1.5.

We point out a selection of the more sophisticated biological spatial simulations in table 1.6 which includes the use of a particle-based method that is of the same class of methods that we will employ.

1.5 The Partition of Unity Method (PUM)

The Partition of Unity Method is a numerical method developed in the late twentieth century (Babuška and Melenk, 1997) for the solution of PDEs important in biology, physics and engineering. PUM belongs to the class of mesh-free methods, recent approaches that seek to improve upon the established mesh-based Finite Element Method (FEM). (Belytschko et al., 1996; Li and Liu, 2002) References in the citation relationship of figure 1.3 show that mesh-free methods are often considered together and were recognized as replacements for FEM in certain applications and inter-compared as they emerged (see table 1.7).

Figure 1.3: Citation relationship for mesh-free method reviews. Mesh-free methods have emerged rather quietly and it is timely that we should consider one method in this class for application to a biological problem.

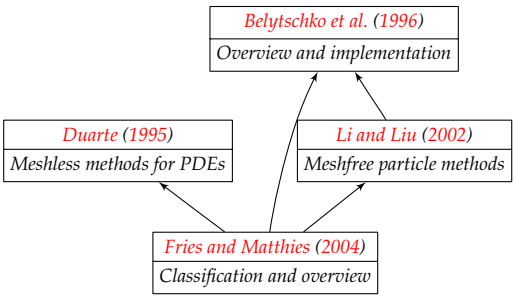

A good treatment of the many different numerical approaches used in FEM is provided by Zienkiewicz et al. (2006) which includes a description of mesh-free methods as "extended finite element methods" (Zienkiewicz et al., 2006, p. 525). A mathematical treatment of the main topics in FEM for numerical solution of PDEs is provided by Strang and Fix (1973) where the emphasis is on numerical analysis rather than physics or functional analysis. The rapid development of FEM in engineering was foreshadowed by Courant (1943) as pointed out by Bramble and Zlámal (1970) with further historical comments by Oden (1987).

1.5.1 The Partition of Unity Method

Spatial Approximation

The Partition of Unity Method was first described as the "Partition of Unity Finite Element Method" Melenk and Babuška (1996), a modification of the Finite Element Method that augments the piecewise polynomial spaces with additional functions that improve the approximation space. References for the early development of PUM are shown in table 1.8.

Figure 1.4: Citation relationship for the partition of unity method. There is a great diversity in the class of mesh-free methods. PUM is one of the more recent and less well-explored members of the class.

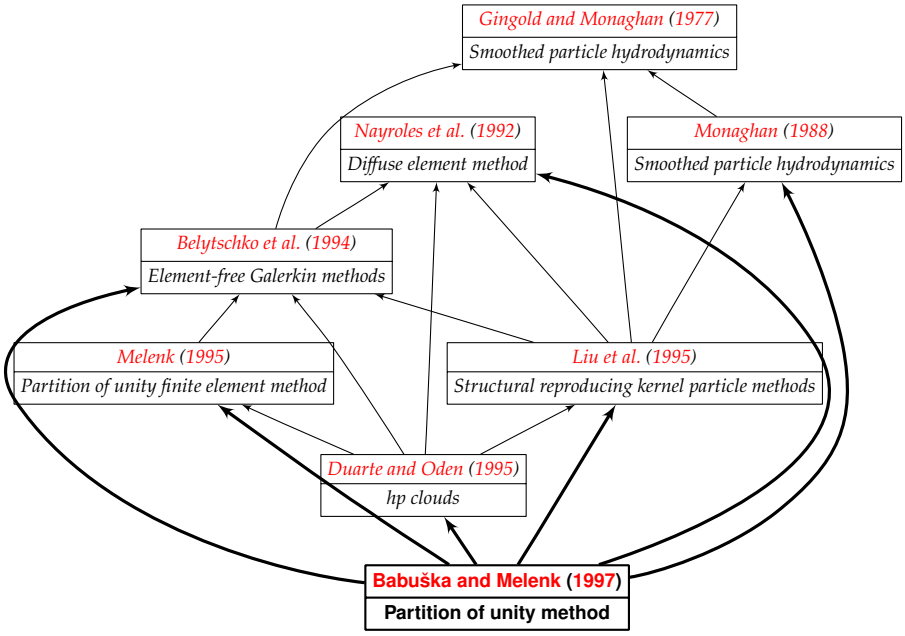

The statement of PUM in a general form was given by Babuška and Melenk (1997) and the numerical approach was taken forward by Griebel

and Schweitzer (2000, 2002a,b) as the Particle-Partition of Unity Method (Particle-PUM) in which PUM is used to discretize elliptic and parabolic equations with operator splitting applied to convection-diffusion problems. The citation relationship for PUM in figure 1.4 shows the inter-relationship between the earliest of the mesh-free methods as a class of advanced numerical methods.

PUM spatial approximation The partition of unity method is a further extension of the Rayleigh-Ritz-Galerkin technique operating on the integral form of a partial differential equation on some domain $\Omega \subset \mathbb{R}^d$ with $d \in \{1, 2, 3\}$. The approximate solution u^h is assumed to be a linear combination of the PUM trial functions $\varphi_i \psi_i^j$. The symbol h denotes a spatial approximation with a certain level of detail.

$$u^h = \sum_{i=1}^{I} \sum_{j=1}^{J_i} (Q_{i,j})(\varphi_i \psi_i^j)$$

The set of scalar functions $\{\varphi_i\}_{i=1}^I$ is a partition of unity (i.e. $\sum \varphi_i = 1$) subordinate to a cover $\{\omega_i\}_{i=1}^I$ of the domain (i.e. $\Omega \subset \overline{\Omega} \subset \bigcup \omega_i$ and $\varphi_i : \Omega \to [0, 1]$ with $\varphi_i \geq 0$ on ω_i and zero everywhere else). The ω_i are called patches. The set of functions $\{\psi_i^j\}_{j=1}^{J_i}$ are suitably chosen local approximation functions and this set is called the local basis on patch i, hence they should be at least linearly independent. The approximation of a PDE that does not depend on time would have $Q_{i,j} \in \mathbb{R}$ whereas for a time dependent PDE we put $Q_{i,j}(t) \in \mathbb{R}$.

Table 1.4: Some reported diffusion coefficients.

Experimental setup	Measurement
FCS of GFP aqueous buffer at ambient temperature.	8.7×10^{-7} cm^2 s^{-1} Terry et al. (1995)
FRAP of GFP in aqueous buffer.	8.67×10^{-7} cm^2 s^{-1} Swaminathan et al. (1997)
FRAP of GFP targeted to mitochondrial matrix using presequence of subunit VIII of human cytochrome c oxidase.	2.6×10^{-7} cm^2 s^{-1} Partikian et al. (1998)
FRAP of GFP in cytoplasm of *E. coli*.	7.7×10^{-8} cm^2 s^{-1} Elowitz et al. (1999)
FRAP of GFP in the lumen of the mammalian endoplasmic reticulum.	$0.5–1 \times 10^{-7}$ cm^2 s^{-1} Dayel et al. (1999)
FCS of GFP in aqueous solution, tobacco cytosol and plastid stromules.	9×10^{-7} cm^2 s^{-1}, 4×10^{-7} cm^2 s^{-1}, 9×10^{-9} cm^2 s^{-1} Köhler et al. (2000)
Single-particle tracking of light harvesting complex II in the stromally-exposed thylakoid membrane.	8.4×10^{-11} cm^2 s^{-1}, 2.7×10^{-10} cm^2 s^{-1} (phosphorylated) Consoli et al. (2005)
FRAP of GFP in 90% glycerol at 25°*C*.	6.6×10^{-7} cm^2 s^{-1}, Pucadyil and Chattopadhyay (2006)
FRAP of TatA-GFP in plasma membrane TorA-GFP in cytoplasm TorA-GFP in periplasm (all *E. coli*).	1.3×10^{-9} cm^2 s^{-1}, 9.0×10^{-8} cm^2 s^{-1}, 2.6×10^{-8} cm^2 s^{-1} Mullineaux et al. (2006)
FRAP of chlorophyll-protein complexes in patches of grana adsorbed onto phosphatidylcholine bilayer.	$4.6 \pm 0.4 \times 10^{-11}$ cm^2 s^{-1}, immobile fraction 73 ± 3% Kirchhoff (2008)

Table 1.5: Photobleaching concerns and recommendations. Computer simulation has long been advocated as a way of checking assumptions made with using photobleaching analysis. This study does not consider anomalous diffusion, in which the mean square displacement of particles varies as t^{α} with $\alpha \neq 1$, and considers diffusion a good approximation at the micron-scale and with the data available. The data presented later is acquired with the best signal to noise ratio balanced against a suitable length of imaging time rather than attempting to minimize observational photobleaching so that it can be neglected in the analysis.

Concern	Recommendation
Anomalous diffusion and multiple diffusing species invalidate effective diffusion approximation.	Allow continuous distributions of diffusion coefficient or allow varying in time.
Periasamy and Verkman (1998)	
Non-instantaneous imaging and photobleaching.	Computer simulation to account for these effects.
Weiss (2004)	
Observational photobleaching of slowly moving species.	Analytic models incorporating observational photobleaching.
Endress et al. (2005)	
Low signal to noise ratio and improper handling of observational photobleaching.	Higher excitation intensity and proper correction for this.
Hagen et al. (2005)	

Table 1.6: Biological spatial simulations – selected articles. Most photobleaching experiments which employ spatial simulations have been carried out on large biological structures such as the cell nucleus and endoplasmic reticulum which are orders of magnitude larger than the chloroplast.

Simulation	Reference
Reaction-diffusion in the nucleus and continuous photobleaching (method unspecified – most likely finite difference with cylindrical symmetry).	Analyzing intracellular binding and diffusion with continuous fluorescence photobleaching. Wachsmuth et al. (2003)
Diffusion in the endoplasmic reticulum lumen and FRAP (particle strength exchange method).	Effects of organelle shape on fluorescence recovery after photobleaching. Sbalzarini et al. (2005)
Diffusion on the endoplasmic reticulum membrane and FRAP (kernel-based particle method).	Simulations of (an)isotropic diffusion on curved biological surfaces. Sbalzarini et al. (2006)
Photoactivation experiments in the nucleus (finite difference method).	Dissecting the contribution of diffusion and interactions to the mobility of nuclear proteins. Beaudouin et al. (2006)

Table 1.7: Emergence of mesh-free methods – key references. The foundation of mesh-free methods is seen to derive from interpolation and approximation problems with a statistical flavour before the emphasis shifted to physical and mathematical considerations.

Year	Title	Author(s)
1968	A two-dimensional interpolation function for irregularly-spaced data.	Shepard
1977	Smoothed particle hydrodynamics: theory and application to non-spherical stars.	Gingold and Monaghan
1981	Surfaces generated by moving least squares methods.	Lancaster and Salkauskas
1992	Generalizing the finite element method: diffuse approximation and diffuse elements.	Nayroles et al.
1994	Element-free Galerkin methods.	Belytschko et al.
1995	Reproducing kernel particle methods for structural dynamics.	Liu et al.
1996	*H-p* clouds – an *h-p* meshless method.	Duarte and Oden
1996	The partition of unity finite element method: basic theory and applications.	Melenk and Babuška

Table 1.8: Foundations of the Partition of Unity Method. PUM, in contrast to other mesh-free methods, developed with an emphasis on similarity to the finite element method rather than by comparison to statistical methods. PUM was introduced by experts in FEM so the foundational publications of PUM and early developments have an excellent grounding in mathematics.

Year	Title	Author(s)
1995	On generalized finite element methods.	Melenk
1996	The partition of unity finite element method; basic theory and applications.	Melenk and Babuška
1997	The partition of unity method.	Babuška and Melenk

Table 1.9: The Particle-Partition of Unity Method – selected articles. Although many studies have been performed on Particle-PUM, all practical examples have been on much more regular domains than the chloroplast domains presented in this study, and the product quadrature integration schemes employed in Particle-PUM are much simpler than the numerical integration scheme presented later.

Year	Title	Author(s)
2000	A particle-partition of unity method for the solution of elliptic, parabolic and hyperbolic PDEs.	Griebel and Schweitzer
2002	A particle-partition of unity method – Part II: efficient cover construction and reliable integration.	Griebel and Schweitzer
	A particle-partition of unity method – Part III: a multilevel solver.	Griebel and Schweitzer
	A particle-partition of unity method – Part IV: parallelization.	Griebel and Schweitzer
	A particle-partition of unity method – Part V: boundary conditions.	Griebel and Schweitzer
2003	A parallel partition of unity method for elliptic partial differential equations.	Schweitzer
2005	A particle-partition of unity method – Part VI: a *p*-robust multilevel solver.	Griebel et al.
2007	A particle-partition of unity method – Part VII: adaptvity.	Griebel and Schweitzer
2008	A particle-partition of unity method – Part VIII: hierarchical enrichment.	Schweitzer
	An adaptive *hp*-version of the multilevel particle-partition of unity method.	Schweitzer
	An algebraic treatment of essential boundary conditions in the particle-partition of unity method.	Schweitzer

Computational PUM approximation The double summation expression of the PUM spatial approximation is rewritten as a single summation to aid computer implementation

$$u^h = \sum_{i=1}^{I} \sum_{j=1}^{J_i} (Q_{i,j})(\varphi_i \psi_i^j) = \sum_{n=1}^{N} q_n \Phi_n$$

With $N = \sum_1^I J_i$ and $n = j + \sum_{k=1}^{i-1} J_k$ (the summation is empty when $i = 1$) so that $q_i \in \mathbb{R}$ or $q_i(t) \in \mathbb{R}$. In practice, we never need to recover i and j given n and the conversion to a single summation is handled naturally with little intervention. The greatest body of references for PUM describes the Particle-Partition of Unity Method variant: a selection of these articles are shown in table 1.9. The implementational descriptions and discussions were invaluable for crafting our implementation and we hope the information we present will help others in this field of research.

Shepard's Method A patch weighting function $W_i : \omega_i \to [0, 1]$ is defined for the patch ω_i, zero outside the patch, so that the partition of unity functions $\{\varphi_i\}_{i=1}^I$ may be formed using Shepard's method. (Shepard, 1968)

$$\varphi_i = \frac{W_i}{\sum_{n=1}^{I} W_n}$$

PUM may be viewed as a generalization of Shepard's Method. (Babuška and Melenk, 1997, p. 731)

1.6 Mathematical Foundation

The mathematical foundation of both the Finite Element Method and the Partition of Unity Method rely on results from functional analysis where integral equations are used to investigate the properties of functions, partial differential equations and generalisations of these. (Adams, 1975) For technical references one may see table 1.8.

The reader is referred to Egorov and Shubin (1998, p. 37) for the classification of PDEs, how they may be of different type within different subsets of their domain of definition and when reduction to canonical form is possible. A problem involving partial differential equations is well-posed in the Hadamard sense if the solution exists for the given boundary data, the solution is uniquely determined by the data, and the solution is stable in appropriate norms. (Brezis, 1998, p. 82)

1.6.1 Important Definitions

The Function Spaces $L^2(\Omega)$ and $H^1(\Omega)$

Let $d \in \{1, 2, 3\}$ and $\Omega \subseteq \mathbb{R}^d$. $L^2(\Omega)$ is defined to be the set of equivalence classes of measurable functions $u : \Omega \to \mathbb{R}$ with

$$\int_\Omega |u(x)|^2 dx < \infty$$

The functional $\|\cdot\|_2$ defined by

$$\|u\|_2 = \left(\int_\Omega |u(x)|^2 dx \right)^{1/2}$$

is a norm on $L^2(\Omega)$. The Sobolev space $W^{m,2}(\Omega)$ is defined to be the set of elements u in $L^2(\Omega)$ that have all weak partial derivatives $D^\alpha u$ of order up to and equal to m also belonging to $L^2(\Omega)$ where $\boldsymbol{\alpha} \in \mathbb{N}^d$ is a multi-index with $0 \leq |\boldsymbol{\alpha}| \leq m$. The functional $\|\cdot\|_{m,2}$ defined by

$$\|u\|_{m,2} = \left(\sum_{0 \leq |\boldsymbol{\alpha}| \leq m} \|D^\alpha u\|_2^2 \right)^{1/2}$$

is a norm on $W^{m,2}(\Omega)$. $H^1(\Omega)$ is defined to be the completion of the space $C^\infty(\Omega)$ with respect to the norm $\|\cdot\|_{1,2}$. It turns out that $H^1(\Omega) = W^{1,2}(\Omega)$ for every domain Ω so we shall use exclusively the notation $H^1(\Omega)$ to denote this space (Adams, 1975, p. 45). The H^1 semi-norm is $|u|_{H^1} = \|\nabla u\|_2$ and will be used to consider convergence of an approximation to the true solution.

1.6.2 Nomenclature of Matrices and Vectors

Borrowing from physical terminology Matrices and vectors may be named based on an inspection of their entries, or based on their physical interpretation.

Finite element equation Solution of a steady problem using FEM or PUM requires the solution of a matrix equation that may be called the "finite element equation" (Strang and Fix, 1973, p. 32), or "system equations" (Zienkiewicz et al., 2006, p. 11).

Mass matrix The mass matrix is used to calculate $\int_\Omega (u^h)^2 \, \mathrm{d}x$ and takes the form shown below (Strang and Fix, 1973, p. 29)

$$\mathbf{M} = \begin{pmatrix} \int_\Omega \Phi_1 \Phi_1 \, \mathrm{d}x & \cdots & \int_\Omega \Phi_1 \Phi_N \, \mathrm{d}x \\ \vdots & \ddots & \vdots \\ \int_\Omega \Phi_N \Phi_1 \, \mathrm{d}x & \cdots & \int_\Omega \Phi_N \Phi_N \, \mathrm{d}x \end{pmatrix}$$

This matrix may arise from a discretization of a wave equation where the terminology has a physical interpretation, or it may arise from a discretization of the heat equation.

Stiffness matrix The stiffness matrix is used to calculate $\int_\Omega |\nabla u^h|^2 \, \mathrm{d}x$ and takes the following form (Strang and Fix, 1973, p. 29)

$$\mathbf{K} = \begin{pmatrix} \int_\Omega \nabla\Phi_1 \cdot \nabla\Phi_1 \, \mathrm{d}x & \cdots & \int_\Omega \nabla\Phi_1 \cdot \nabla\Phi_N \, \mathrm{d}x \\ \vdots & \ddots & \vdots \\ \int_\Omega \nabla\Phi_N \cdot \nabla\Phi_1 \, \mathrm{d}x & \cdots & \int_\Omega \nabla\Phi_N \cdot \nabla\Phi_N \, \mathrm{d}x \end{pmatrix}$$

Naming based on physical interpretation The general form of a damped wave equation

$$\rho \frac{\partial^2 u}{\partial t^2} + \mu \frac{\partial u}{\partial t} - \nabla \cdot (\kappa \nabla u) = 0$$

gives rise to a "matrix differential equation" (Zienkiewicz et al., 2006, p. 564)

$$\boldsymbol{M}_\rho \ddot{\boldsymbol{q}} + \boldsymbol{C}_\mu \dot{\boldsymbol{q}} + \boldsymbol{K}_\kappa \boldsymbol{q} + \boldsymbol{f} = \boldsymbol{0}$$

where $\boldsymbol{M}_\rho$ is the mass matrix, $\boldsymbol{C}_\mu$ is the damping matrix and $\boldsymbol{K}_\kappa$ is the stiffness matrix

$$\begin{aligned} \boldsymbol{M}_\rho &= \left(\int_\Omega \rho \Phi_i \Phi_j \, \mathrm{d}x \right)_{ij} \\ \boldsymbol{C}_\mu &= \left(\int_\Omega \mu \Phi_i \Phi_j \, \mathrm{d}x \right)_{ij} \\ \boldsymbol{K}_\kappa &= \left(\int_\Omega \nabla\Phi_i \cdot \nabla\Phi_j \, \mathrm{d}x \right)_{ij} \\ \boldsymbol{f} &= \left(\int_\Omega \Phi_i f \, \mathrm{d}x \right)_i \end{aligned}$$

1.6.3 Spatial Discretization of PDEs

The usefulness of partial differential equations to science and engineering is largely thanks to the numerical methods which allow approximate solutions to be found on computers and supercomputers. Numerical methods for the solution of PDEs must provided a discrete description that faithfully represents the continuous problem.

Rayleigh-Ritz Method – Variational Formulation

The aim of the Rayleigh-Ritz method (Courant, 1943; Schultz, 1969) is to find a function u that minimizes some functional J. A finite number of trial functions $\phi_1, \ldots, \phi_N$ are chosen (with $N \in \mathbb{N}$) so the vector space V of linear combinations $\sum_{i=1}^{N} q_i \phi_i$ is a suitable approximation of the domain of J. The Ritz approximation of the minimum u is then the element in V that minimizes $J(u)$.

Galerkin Method – Weak Formulation

The Galerkin method approximates the solution of $L(u) = f$ in a finite subspace of functions $V = span\{\Phi_1, \ldots, \Phi_N\}$ by finding the element $u \in V$ such that the residual $L(u) - f$ is orthogonal to the chosen basis of V. This is

the approach we take in our implementation of PUM as convection is not present in our models so no stabilization is required (Fries and Matthies, 2005).

Weighted Residual Method

The weighted residual method approximates a solution of an equation in a finite subspace $V = span\{\Phi_1, \ldots, \Phi_N\}$ by finding the element that is orthogonal to a carefully chosen set of functions $\{\Psi_j\}_{j=1}^{M}$ that may or may not be related to the Φ_i. The motivation for this is that certain terms may require a special form of the test function to stablize the solution and this leads to modifying the test function for all other terms to maintain consistency of the equations (Fries and Matthies, 2005).

1.6.4 Example Discretization of PDEs

We will later present an involved discretization that is able to maintain the inhomogeneity of the fluorescence distribution so we give some simple discretizations in preparation. In the following examples we multiply the classical form of the PDE by a test function $v \in V$ belonging to some suitable space of functions V and integrating over the domain Ω. The resulting integral equation is manipulated using the integration by parts

rule and the divergence theorem to arrive at an equation that involves an integral over the boundary Ω.

Table 1.10: Types of boundary condition (b.c.) for PDEs defined on the domain $\Omega \in \mathbb{R}^d$ with boundary $\partial\Omega$. Here $\frac{\partial u}{\partial n} = (\nabla u) \cdot \boldsymbol{n}$ and $\boldsymbol{n}$ is the unit normal vector on the oriented boundary $\partial\Omega$ pointing out of Ω.

Name	Example
Dirichlet or essential b.c.	$u = f$
Neumann or natural b.c.	$\frac{\partial u}{\partial \boldsymbol{n}} = 0$
Robin or generalized Neumann b.c.	$au + b\frac{\partial u}{\partial \boldsymbol{n}} = g$
Mixed	combinations of the above

The Dirichlet boundary condition may be regarded as a limiting case of the Robin boundary condition (Courant, 1943, p. 8)

$$\frac{1}{\gamma}\frac{\partial u}{\partial \boldsymbol{n}} + u = g$$

Further choices of boundary conditions are shown in table 1.10 although we will be interested only in zero Neumann boundary conditions for our biological simulations.

Poisson's Equation

Poisson's equation is a second order PDE.

$$\begin{aligned} -\Delta u &= f \\ -\int_\Omega v \Delta u \, \mathrm{d}x &= \int_\Omega v f \, \mathrm{d}x \end{aligned}$$

Neumann boundary conditions are readily imposed after application of the divergence theorem.

$$\int_\Omega \nabla v \cdot \nabla u \, \mathrm{d}x - \int_{\partial\Omega} v \frac{\partial u}{\partial \boldsymbol{n}} \, \mathrm{d}S = \int_\Omega v f \, \mathrm{d}x$$

We take the Dirichlet boundary condition $u = g$ to be the limit $\gamma \to \infty$ of the Robin boundary condition

$$\frac{1}{\gamma} \frac{\partial u}{\partial \boldsymbol{n}} + u = g$$

so that

$$\int_\Omega \nabla v \cdot \nabla u \, \mathrm{d}x - \gamma \int_{\partial\Omega} v(g - u) \, \mathrm{d}S = \int_\Omega v f \, \mathrm{d}x$$

$$\int_\Omega \nabla v \cdot \nabla u \, \mathrm{d}x + \gamma \int_{\partial\Omega} v u \, \mathrm{d}S = \int_\Omega v f \, \mathrm{d}x + \gamma \int_{\partial\Omega} v g \, \mathrm{d}S$$

Helmholtz's Equation

$$\begin{aligned} -\Delta u \quad &+ \quad k^2 u \quad = 0 \\ -\int_\Omega v\Delta u \, \mathrm{d}x + k^2 &\int_\Omega vu \, \mathrm{d}x = 0 \end{aligned}$$

A slight variant on this equation will be used for initial testing of our PUM implementation with a known solution to check convergence behaviour as the approximation approaches the true solution.

$$\int_\Omega \nabla v \cdot \nabla u \, \mathrm{d}x - \int_{\partial\Omega} v\frac{\partial u}{\partial \boldsymbol{n}} \, \mathrm{d}S + k^2 \int_\Omega vu \, \mathrm{d}x = 0$$

1.6.5 Temporal Discretization of PDEs

The Diffusion Equation

$$\frac{\partial u}{\partial t} - \Delta u = 0$$

$$\int_\Omega v\frac{\partial u}{\partial t} \, \mathrm{d}x + \int_\Omega \nabla v \cdot \nabla u \, \mathrm{d}x - \int_{\partial\Omega} v\frac{\partial u}{\partial \boldsymbol{n}} \, \mathrm{d}S = 0$$

The partition of unity method is used to approximate time-dependent spatial functions with

$$u^h(t,x) = \sum_{i=1}^{N} q_i(t)\Phi_i$$

where $t \in \mathbb{R}_{\geq 0}$, $x \in \mathbb{R}^d$, and $q_i : \mathbb{R}_{\geq 0} \to \mathbb{R}$. For $\frac{\partial u}{\partial \boldsymbol{n}} = 0$, we get

$$\boldsymbol{M}\dot{\boldsymbol{q}}(t) + \boldsymbol{K}\boldsymbol{q}(t) = 0$$

where $\boldsymbol{M}$ is the mass matrix and $\boldsymbol{K}$ is the stiffness matrix. Using backward Euler time stepping, we get

$$\boldsymbol{M}\boldsymbol{q}(t+\delta t) + \delta t\boldsymbol{K}\boldsymbol{q}(t+\delta t) = \boldsymbol{M}\boldsymbol{q}(t)$$

1.7 Problem Statement and Principal Results

Problem statement The *in vivo* behaviour of the Tat substrate in chloroplast protein targeting is not well understood: the complex structure of the thylakoid membrane creates a highly heterogeneous stromal compartment with unknown implications for protein targeting. Despite protein targeting being an inherently spatial process, protein targeting research is often of a non-spatial, biochemical nature and the use of fluorescence microscopy in this field has been limited up to now. Current modelling and computational mathematics to investigate spatio-temporal dynamics of protein targeting have been unsophisticated and the application of mathematical

techniques remains woefully under-explored. This study investigates the bulk behaviour of chimeric Tat proteins in the chloroplast and looks at the use of a state of the art numerical method in analyzing the results from microscopy.

Principal results This thesis analyzes the behaviour of the Tat substrate in protein targeting and the effect of the signal peptide on the substrate dynamics in the chloroplast stroma. We have used the fluorescence loss in photobleaching technique to characterize the substrate dynamics and show the variation of measurements between chloroplasts. An advanced numerical method, well-suited to complex biological compartments, is used to model our photobleaching experiments in a more compelling way than is common in the biological modelling and simulation literature.

Tat signal peptide has a pronounced effect *in vivo* Rather than the substrate being freely diffusing in the chloroplast stroma, our *in vivo* data suggests that the Tat signal peptide causes hindered mobility of the Tat substrate. The current belief based on *in vitro* data is that there is signal peptide-mediated association of Tat substrates with biological membranes and our data suggests there is a manifestation of this effect *in vivo*. This leads us to postulate that a population of Tat substrate will associate with the thylakoid membrane and move laterally before recruitment of Tat membrane proteins to facilitate translocation. This population is large enough

that the hindered mobility is apparent but not so large that the Tat substrate appears anchored to the thylakoid membrane as would be the case for a membrane protein.

High performance implementation of PUM A parallel d-binary tree implementation of PUM is presented which eliminates a great deal of the redundant calculation that has been present during the assembly phase in previous work within our group. Matrix-vector operations are used in placed of explicit integration of approximations and this re-use of calculation further helps to minimize walltime. The implementation is a novel particle-free formulation which is able to carry out single execution convergence testing to high levels of refinement detail in very reasonable walltimes. It is shown that some of the apparent difficiencies and implementational expense of the partition of unity method can be overcome and PUM has a promising future in numerical simulation of biological systems and processes.

Biological application of PUM Geometries are extracted from actual spatio-temporal data series and we compare parameters suggested by our simulations to published diffusion coefficients. The work presented is one of the earliest uses of PUM for a direct biological application using actual data and is one of a small number of mesh-free methods being applied to a biological problem. We go on to show how single-species

and inhomogeneous diffusion models are able to capture the fluorescence distributions apparent in the data to give a frame-by-frame comparison of confocal images and simulation; and a multi-species model is able to capture other aspects of the data.

Chapter 2

Materials and Methods

2.1 Protoplast Transfection

I. Isolation of Protoplasts

K3 Medium : 3.78 g/L Gamborg's B5 basal medium (minimal organics)

750 mg/L $CaCl_2 \cdot 2H_2O$

250 mg/L NH_4NO_3

136.2 g/L Sucrose

1 mg/L 6-benzylaminopurine

1 mg/L α-napthtalenacetic acid

10× Enzyme Mixture : 2% Macerozyme Onozuka R-10
4% Cellulase Onozuka R-10
(dissolved in K3 Medium)

Enzymatic digestion of cell wall Young green leaves (2-5 weeks) are taken from axenically grown tobacco plants. Cuts spaced 1-2 mm apart are made on the underside of the leaf using a blade but without cutting through the whole thickness of the leaf. The leaves are floated on 7 mL of 1× enzymatic mixture (diluted in K3 buffer) at room temperature with cut-side in contact with the enzymatic mixture. The required number of plates are placed over night at 25°C in the dark. (Pedrazzini et al., 1994) Chloroplasts were isolated before imaging by expelling three times through a 20 µm pore-diameter mesh secured at the opening of a syringe with the sample manually poured back into the syringe after each passage through.

W5 Medium : 9 g/L NaCl
0.37 g/L KCl
18.37 g/L $CaCl_2 \cdot 2H_2O$
0.9 g/L Glucose
(filter sterilized and stored at -20°C)

Recovery of the protoplasts A plastic Pasteur pipette is used to remove the enzymatic digestion mixture leaving the translucent shape of the leaves

intact. The protoplasts are release by drop-wise addition of K3 medium directly onto the leaves. The protoplast suspension is filtered through a sterile 100 μm mesh nylon filter pre-wetted with K3 medium and collected in a Petri dish. The suspension is centrifuged in sterile centrifuge tubes for 20 minutes at 400-600 rpm in a swinging bucket centrifuge with the brake off to minimise damage to the protoplasts. A Pasteur pipette is used to remove the pellet of plant debris. Four volumes of W5 medium is added slowly and mixed gently so that the floating protoplasts will sink. The suspension is centrifuged to pellet the protoplasts and the supernatant is removed. The protoplast pellet is washed and resuspended gently with the same volume of W5 medium. The suspension is centrifuged again and the pellet is resuspended in 10 mL W5 medium. (Pedrazzini et al., 1994)

MaCa Buffer : 0.5 M Mannitol
20 mM $CaCl_2$
0.1% MES pH 5.7
(filter sterilized and stored at -20°C)

40% PEG 4000 : 40% PEG 4000 (Merck)
0.1 M $Ca(NO_3)_2 \cdot 4H_2O$
0.5 M Mannitol
(pH 8-10 adjusted with KOH, filtered
through a 0.22μm filter and stored at -20°C)

Protoplast transfection The suspension is centrifuged at 600 rpm with the brake off. The supernatant is removed and the pellet is resuspended in MaCa buffer to a volume of 0.8-1 mL for each transfection to be performed. The protoplasts are heat shocked at 45°C for 5 minutes and allowed to cool at room temperature for at least 5 minutes. The DNA to be used for the transfection (approximately 20-40 μg per transfection) are placed in sterile 15 mL polypropylene tubes and brought to the same volume with sterile MaCa buffer. The protoplasts are added using cut pippette tips to avoid damage to the protoplasts, 0.8-1 mL of the protoplast suspension is added to each polypropylene tube and mixed gently with the DNA. The tubes are tilted so that an equal amount of 40% PEG solution can be added dropwise near the lip of the tubes and allowed to mix gently with the protoplast suspension. The suspension is mixed very gently and incubated at room temperature for 30 minutes. The tubes are filled with incremental 3 mL volumes followed by gentle mixing until the final 15 mL volume is reached taking at least 15 minutes to avoid damage to the protoplasts. The suspensions are centrifuged at 600 rpm for 10 minutes with the brake off and the supernatant is discarded. The protoplasts are resuspended in 1 mL K3 medium and incubated in the dark at 25°Cover night. (Pedrazzini et al., 1997)

2.2 Fluorescence Loss in Photobleaching (FLIP)

Microscope and settings A Leica TCS SP5 was used for fluoresence confocal imaging and carrying out the modified FLIP procedure. The 488 nm laser line was used for both imaging and photobleaching with a scan resolution of 512×512 pixels, 8 bit intensity values (giving 256 possible values), and a scan rate of 0.754 s per frame. A 63× oil immersion lens was used and the GFP fluoresence signal was collected in the 400-450 nm range with the gain set appropriately and kept fixed during the course of the measurements. The Leica FlyMode is used so that bleaching at 100% laser intensity occurs in the forward scan of each line and imaging at 3% laser intensity occurs in the backward scan of the same line to minimize the time separation of bleaching and imaging.

Modified FLIP procedure A protoplast expressing one of the GFP fusions was centred in the field of view using a low magnification to minimize imaging photobleaching. The automated procedure begins by switching to 20 times magnification. Two pre-bleach images are acquired to give an indication of the observational photobleaching, 50 bleach frames are acquired in which bleaching occurs in a spot either 0.4 μm or 1.0 μm in diameter. A final 20 post-bleach frames are recorded to observe any recovery back into the bleached spot.

Observational control The modified FLIP procedure described was carried out with the bleach spot set outside the chloroplast of interest so that the would switch laser intensity from 100% in the forward bleach direction to 3% in the backward imaging direction without bleaching within the chloroplast under observation.

Figure 2.1: Fluorescence Loss In Photobleaching (FLIP) procedure.

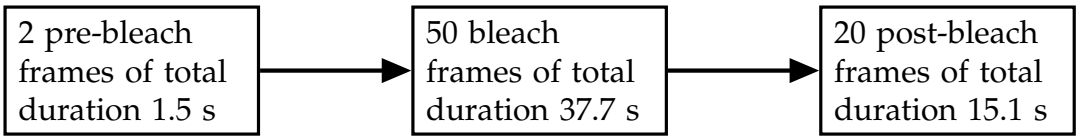

2.3 Chloroplast and Thylakoid Import

Chloroplasts are isolated from *Pisum sativum* (the Garden Pea plant) and provide us with a functional Tat system for experimentation and analysis. Thylakoids may be isolated from lysed[a] chloroplasts.

I. Isolation of Chloroplasts

Garden pea plants are easy to grow and many can be grown in a small area to provide a larger number of leaves and a large number of chloroplasts. Once the leaf cells are broken and the chloroplasts are released, the chloro-

[a] induced to break or burst in order to release the contents

plasts must be maintained in a solution that is isotonic with the stroma of the chloroplasts.

HEPES Sorbitol (HS) Buffer : 50 mM HEPES–KOH pH 8.0
0.33 M Sorbitol

Removal of general plant debris Trays of garden peas (*Pisum sativum*) are grown for 8–9 days. The leaves are harvested and homogenized in 250 mL HS buffer to break the leaf cells and release the chloroplasts. The homogenate is filtered through two layers of Miracloth to separate the debris from the chloroplasts. The filtrate is centrifuged at 3300 g for 2 minutes at 4°C. The pellet of chloroplasts is resuspended in 2 mL of HS buffer using cotton swabs.

Removal of broken chloroplasts The resuspended chloroplasts are centrifuged through Percoll pads at 1400 g for 8 minutes at 4°C to separate the intact chloroplasts from the broken chloroplasts. The broken chloroplasts are discarded as they form the interface sitting on the Percoll and are easily removed using a Pasteur pipette. The pellet is washed in 10 mL HS buffer by resuspension and centrifuging at 3000 g for 2 minutes at 4°C. The washed pellet is resuspended in a minimum volume of HS buffer (0.5-0.8 mL).

Adjusting chloroplast concentration 5 μL of the sample of intact chloroplasts is vortexed with 1 mL of 80% acetone to release the chlorophyll from the chloroplasts. This is prepared in triplicate to give a better estimate of the amount of chlorophyll present. The three samples are centrifuged at 13000 rpm for 1 minute to pellet starch and the absorbance of the supernatant is measured at 652 nm.

II. Isolation of Thylakoids

HEPES Magnesium (HM) Buffer	: 10 mM HEPES–KOH pH 8.0 5 mM $MgCl_2$
Protease	: 10 mg/mL Trypsin in 1×HM
Protease Inhibitor	: 10 mg/mL Trypsin inhibitor in 1×HM

Osmolysis of chloroplasts Chloroplasts are taken at 2.0 mg/mL chlorophyll and centrifuged at 7000 rpm for 1 minute. The chloroplasts are resuspended by marking the level of the supernatant and replacing the supernatant with an equal volume of HM buffer. The chloroplasts are resuspended and left to lyse on ice for 10 minutes. The lysed chloroplasts are centrifuged at 13500 rpm for 2 minutes to pellet the thylakoid membranes and leave the stromal contents in the supernatant. The stroma diluted in HM can be kept for other experiments. The thylakoids are washed three times by resuspending in 0.7 mL HM. The thylakoids are finally resus-

pended in the marked volume of HM.

2.3.1 Radiolabelled Imports

Translation of the Tat substrate was carried out in the prescence of radioactive ^{35}S methionine for one hour at 27°C. For a thylakoid import, 20 μL of thylakoids at a concentration of 0.5 mg/mL chlorophyll was incubated with 5 μL translation for 30 minutes at 25°C in an illuminated water bath. 1 mL HM is added to stop the import and the thylakoids are pelleted by centrifugation at 13000 rpm for 2 minutes at 4°C. The pellet is resuspended in 60 μL HM and separated into two 30 μL aliquots: one that will be analyzed directly and one that is treated with 0.05 mg/mL trypsin on ice for 30 minutes to digest translation product that has not been imported. In the case of a chloroplast import, a 40 minute incubation with thermolysin on ice is used to digest translation product that has not been imported into the chloroplast. The chloroplasts are lysed to extract the thylakoids fraction which is treated as before. Samples of different fractions are reserved along the way to track the route taken by the radiolabelled Tat substrate and to see at which stages the Tat substrate is protected from protease.

2.4 Computer Hardware and Software

2.4.1 Developmental Software

Software development took place on the Ubuntu and Gentoo GNU/Linux operating systems using KDevelop-3.5, GNU Emacs-22.2 and Vim-7.2. Version control was handled by Subversion-1.3.2 on a virtual private server hosted by Webfusion (GX Networks Ltd) and the build system was the Python-based software construction tool SCons-1.2.0.

2.4.2 Production Testing

The primary platform for production testing of our PUM implementation was the **Centre for Scientific Computing**[b] **IBM cluster**.

The IBM cluster has 240 two-way nodes with Intel Xeon 5160 "Woodcrest" socket J (LGA 771), dual core, 3.0 GHz processors (480 processors, 960 cores in the whole cluster); 8 GB RAM (1.92 TB in the whole cluster) and QLogic InfiniPath interconnect. The operating system is SUSE Linux Enterprise Server 10 (Novell, Inc) with job scheduling provided by PBS Professional 10.0 (Altair Engineering, Inc).

[b] University of Warwick, Coventry CV4 7UW, United Kingdom

The MPI-based PETSc 3.0.0 library and our applications were compiled using the Intel Compilers 10.1 and linked to Open MPI 1.2.8 and the Intel Math Kernel Library 10.0 (MKL). OpenMP[c] was used for shared memory computation with up to four OpenMP threads sharing the work assigned to a node. (OpenMP) The IBM General Parallel File System was used for high performance output of binary Visualization Toolkit (VTK), XML format files for visualization in ParaView 3.2.2 (Kitware, Inc).

2.4.3 Development Testing

Development testing was carried out on an AMD Athlon 64 X2 4400+ "Toledo", socket 939, dual core, 2.5 GHz processor with 4 GB RAM running the Ubuntu 9.04 "Jaunty Jackalope" (Canonical, Ltd) GNU/Linux operating system. PETSc 3.0.0 and our applications were compiled with the GNU Compiler Collection (GCC) 4.3.2 C++ compiler and linked to MPICH2 1.0.8.

Development testing also took place on an AMD Athlon 64 3500+ "Venice", socket 939, 2.2 GHz processor with 2 GB RAM running the Gentoo GNU/Linux operating system. PETSc 3.0.0, OpenMPI 1.3.2 and our applications were compiled with the GCC 4.3.1 C++ compiler.

[c]Open Multi-Processing Application Program Interface

Part II

Results, Discussion and Conclusion

Chapter 3

Spatio-Temporal Dynamics of Chloroplast Tat Substrates

This chapter describes the experimental approach taken to better understand the role of the signal peptide in the early stages of protein targeting leading up to translocation. The current state of research into chloroplast Tat substrate dynamics is described and various possible models are presented for how the substrate interacts with the thylakoid membrane and the integral membrane proteins of the Tat translocase. Actual data from experiments conducted on a laser scanning confocal microscope are presented with different experimental repetitions shown side-by-side to illustrate both the variability between chloroplasts and between experiments. Various analyses of the data are presented and the results are discussed.

3.1 Substrate Dynamics in Tobacco Chloroplasts

The vast majority of our knowledge about chloroplast protein targeting comes from *in vitro* biochemical data and this is particularly the case for the chloroplast Tat pathway (Cline and Mori, 2001; Dabney-Smith et al., 2006; Schünemann, 2007). Studies on the chloroplast Tat pathway have made use of fluorescent proteins and fluorescence microscopy with the potential for dynamic analysis but they have usually observed steady states (Marques et al., 2004; di Cola and Robinson, 2005).

The targeting of fluorescent proteins to the Tat pathway lags behind such work in bacteria (Thomas et al., 2001; Barrett et al., 2003; Marques et al., 2003) and only a little more characterization of Tat substrate dynamics has been done in bacteria (Mullineaux et al., 2006).

Expression, targeting and imaging of GFP Colleagues in the laboratory provided ready-made DNA constructs for transient expression in tobacco protoplasts and targeting to the chloroplast. Alessandra di Cola provided pre23k-GFP and pre23k-ΔTPP-GFP (di Cola and Robinson, 2005), Cassie Aldridge provided TP-GFP and Elina Vladimirou provided Hcf106-GFP.

The two Tat substrates are pre23k-GFP, the wild-type bipartite signal peptide of the thylakoid lumenal 23 kDa oxygen-evolving complex subunit

Figure 3.1: Tat substrate dynamics in the chloroplast. A chloroplast is shown with the inner and outer chloroplast envelopes enclosing the thylakoid membrane system (granal stacks joined by stromal lamellae). The confocal imaging slice is depicted as a horizontal slice with a vertical laser photobleaching at a spot in the centre of the chloroplast. **(A)** is a stromal region containing predominantly soluble proteins. Protein movement is restricted in thylakoid membrane-dense regions such as **(C)**. There are two proposed models for how the Tat substrate (orange rectangles) proceeds to the Tat translocase (blue circles). The Tat substrate may either **(B)** bind first to the thylakoid membrane and move laterally to meet the translocase, or **(D)** the Tat substrate may bind directly to the Tat translocase from the stroma. **(E)** shows a postulated equilibrium established between bound and unbound Tat substrate.

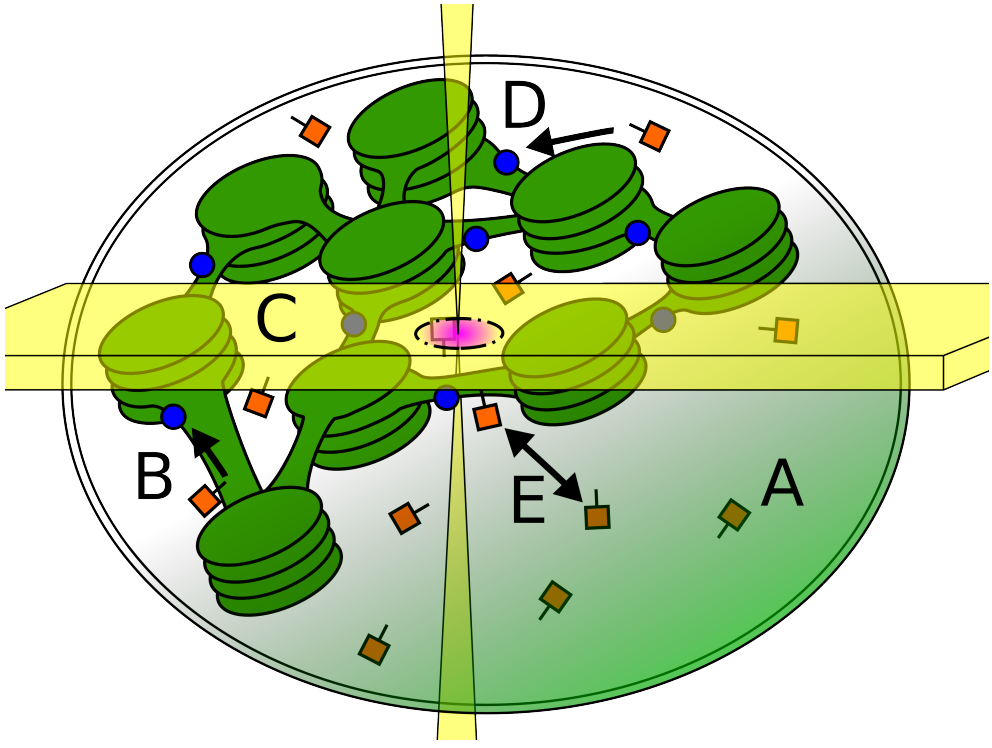

(pre23k) fused to GFP; and pre23k-GFPΔTPP, the same signal peptide with the thylakoid processing peptidase (TPP) cleavage site altered to prevent removal of the signal peptide (di Cola and Robinson, 2005). We compare these to TP-GFP, the first part of the pre23k signal peptide targeting GFP to the stroma; and Hcf106-GFP, GFP fused to the chloroplast Tat membrane protein Hcf106.

The pre23k-GFP and pre23kΔTPP constructs are well-characterized (di Cola and Robinson, 2005). The pre23k-GFP construct is expected to result in a mixed population of mature and precursor GFP and hence display a larger variability in fluorescence depletion during photobleaching. The pre23kΔTPP-GFP cannot be processed to the mature form so will retain its signal peptide and we would expect the greatest level of signal peptide mediated interaction with the thylakoid membrane. As a mobile control we have TP-GFP which is imported into the chloroplast and processed to the mature form, without the transit peptide, by the stromal processing peptidase. The immobile control is Hcf106-GFP which will be anchored to the thylakoid membrane and should be the least mobile of the contructs analyzed.

Display of frames In the following sections, certain frames have been selected from the total of 72 frames for a FLIP sequence in a way that allows direct comparison between constructs and between observation photobleaching and the modified FLIP. This format will be used again when

simulations are performed based on the data presented in this chapter. The selected frames are: the first image, the first bleach image, the last bleach image, the first post-bleach image and the last image in the sequence; these are indices 0, 2, 51, 52, 71 respectively. The bleach spot is indicated in the cases where spot photobleaching has taken place.

3.1.1 Small Bleach Region Modified FLIP

A small bleach region of 0.4 μm diameter was used at first to ensure minimal invasiveness and our imaging time was kept below one minute. The high rate of fluorescence depletion of mobile species is most evident for pre23k-GFP in panels **(A-D)** of figure 3.4 and all panels of TP-GFP in figure 3.6, as compared to the less mobile pre23kΔTPP-GFP in figure 3.2 and Hcf106-GFP in figure 3.8. It may be seen that the observational photobleaching rates of all constructs; figures 3.3, 3.5, 3.7 and 3.9; were comparable although pre23kΔTPP-GFP appeared a little more resistant to photobleaching in this data series as can be seen from panel **(B)** in figure 3.11.

We note the pointwise standard deviation bands for observational photobleaching are especially tight around the pointwise averages for the homogeneous **(A)** TP-GFP, less mobile **(B)** Hcf106-GFP and **(C)** pre23kΔTPP-GFP in figure 3.10. There is greater variability for when spot photobleaching is present during the FLIP procedure but only **(D)** pre23k-GFP shows

evidence of a range of behaviours in figure 3.10.

There are certain features in the graphs of figure 3.10 that we will be unable to address with the data. All fluorescence depletion graphs show comparable sharp initial drops and the time at which spot bleaching is stopped is marked by a rise in the fluorescence graph. The rise is most likely caused by movement of fluorescent protein into the confocal imaging slice from above and below the slice. The initial drop must be connected with the onset of imaging but we have no way of determining its cause without a significant detour from the main line of enquiry. It should be noted that the initial drop occurs in a very short interval of time even when compared to the short total duration of the experiment so assigning it a lower priority is not unjustified. Whatever its cause, it serves as a warning to experimentalists who would try to make measurements in tiny intervals of time very close to the start of bleaching and imaging.

The magnitude of the slopes of the linear portion of the graphs shown in figure 3.10 are plotted in panel **(B)** of figure 3.11 to compare and quantify the rates of whole-chloroplast fluorescence depletion caused by spot bleaching. Panel **(A)** of figure 3.11 shows a correction for the observational photobleaching effect. Even from the confocal images themselves it was clear that TP-GFP is highly mobile which is characterized by the small bleach spots seen in figures 3.6, as compared to pre23k-GFP and pre23kΔTPP-GFP, and we will see this again with simulations in which we are able to control the various bleach and diffusion parameters.

Figure 3.2: Modified FLIP pre23kΔTPP-GFP (small bleach region). Rows of five experimental repetitions **(A-E)** are shown (different chloroplasts). Later frames in each row show slightly lower levels of fluorescence than earlier frames in the row. The scale bar is 5 μm in length. pre23kΔTPP-GFP has relatively low mobility yet the bleach region appears smeared in a horizontal direction in the first-bleach (column 3) and last-bleach (column 4) columns which shows redistribution between the forward bleach scan of a line and the immediate backward imaging scan of the same line.

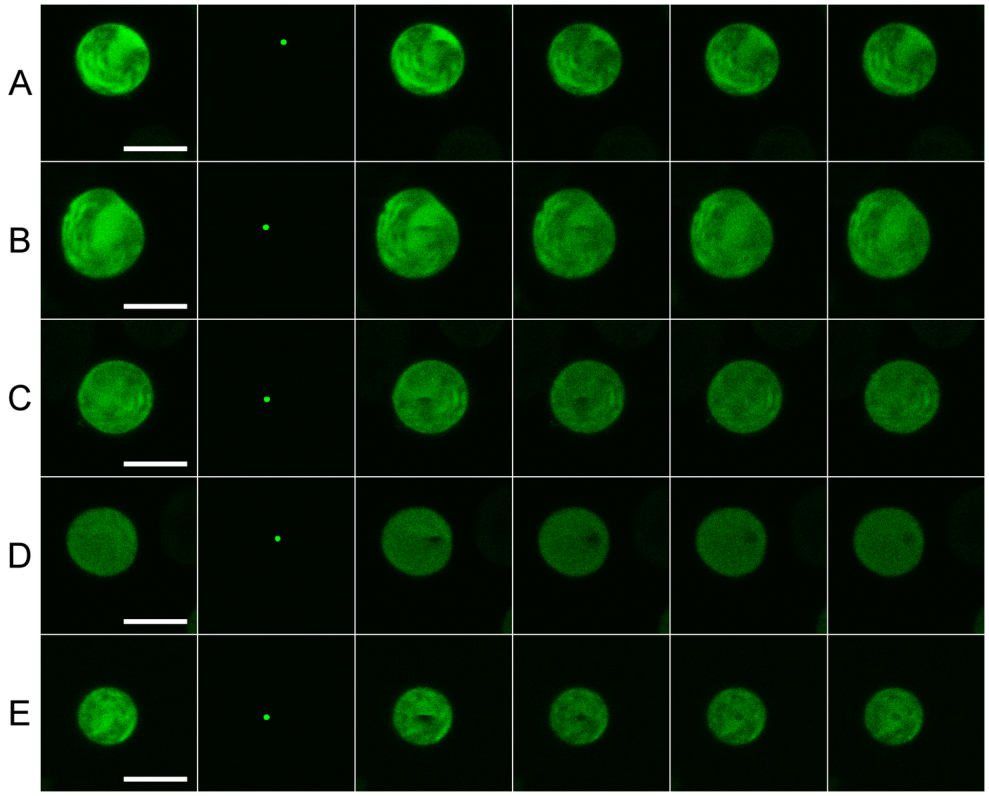

Figure 3.3: Observational control: pre23kΔTPP-GFP. Rows of five experimental repetitions **(A-E)** are shown (different chloroplasts). Later frames in each row show very similar levels of fluorescence to earlier frames in the row. The scale bar is 5 μm in length.

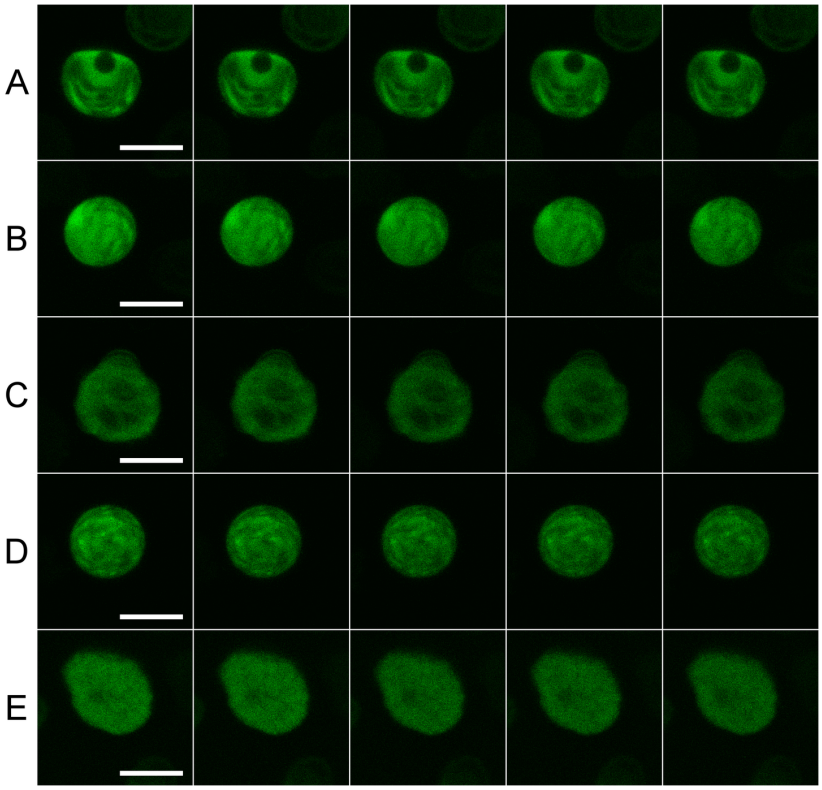

Figure 3.4: Modified FLIP: pre23k-GFP (small bleach region). Rows of five experimental repetitions **(A-E)** are shown (different chloroplasts). Later frames in each row show lower levels of fluorescence than earlier frames in the row. The scale bar is 5 μm in length. The high mobility of pre23k-GFP is evidenced by the extent the bleach region leads to a widening depleted local region (column 3) and noticeably less fluorescence near the end of the sequence (columns 4 to 6).

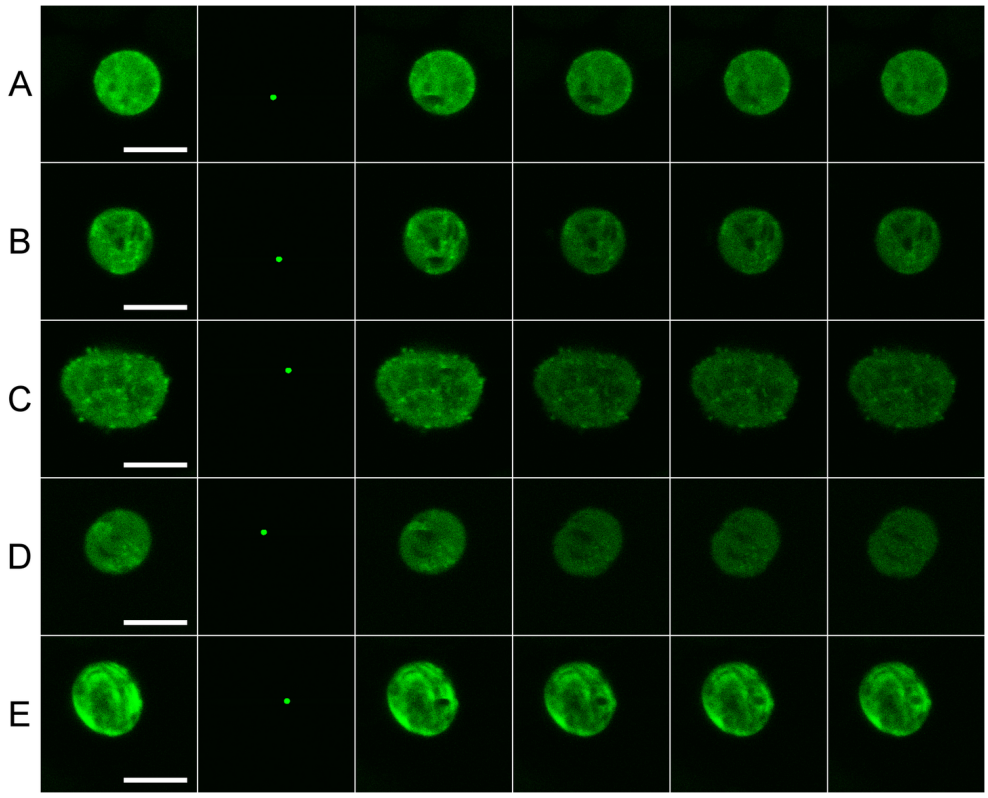

Figure 3.5: Observational control: pre23k-GFP. Rows of five experimental repetitions **(A-E)** are shown (different chloroplasts). Later frames in each row show very similar levels of fluorescence to earlier frames in the row. The scale bar is 5 μm in length.

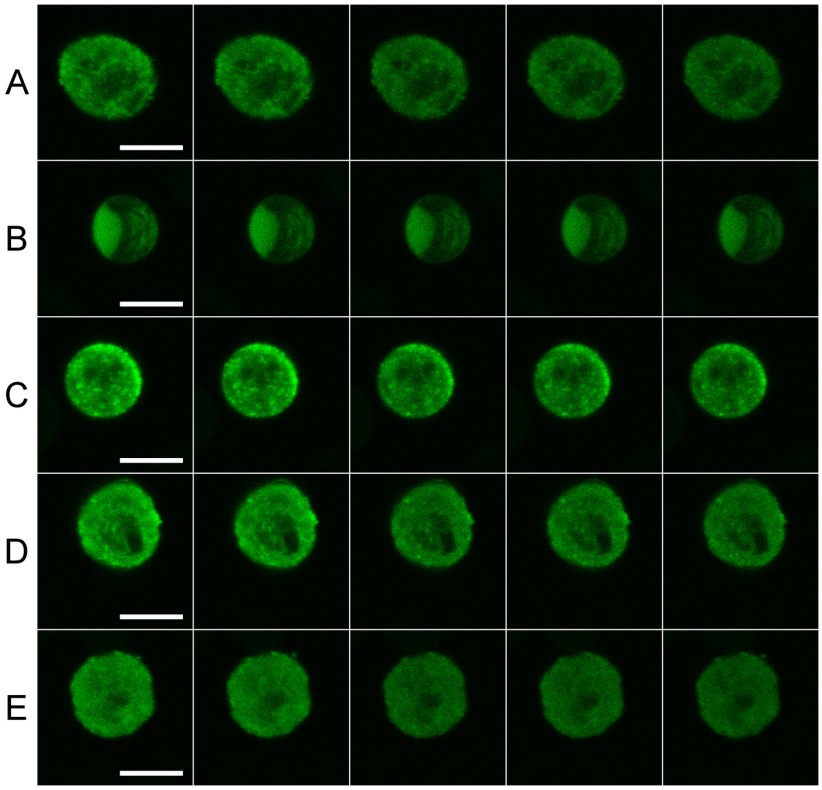

Figure 3.6: Modified FLIP: TP-GFP (small bleach region). Rows of five experimental repetitions **(A-E)** are shown (different chloroplasts). Later frames in each row show lower levels of fluorescence than earlier frames in the row. The scale bar is 5 μm in length. TP-GFP is an example of how modelling and simulation is important for testing our interpretation of photobleaching analyses as here we see the most rapid depletion in the later stages (columns 4 to 6) but the depletion is fairly uniform across the chloroplast without the expanding bleach region seen for pre23k-GFP.

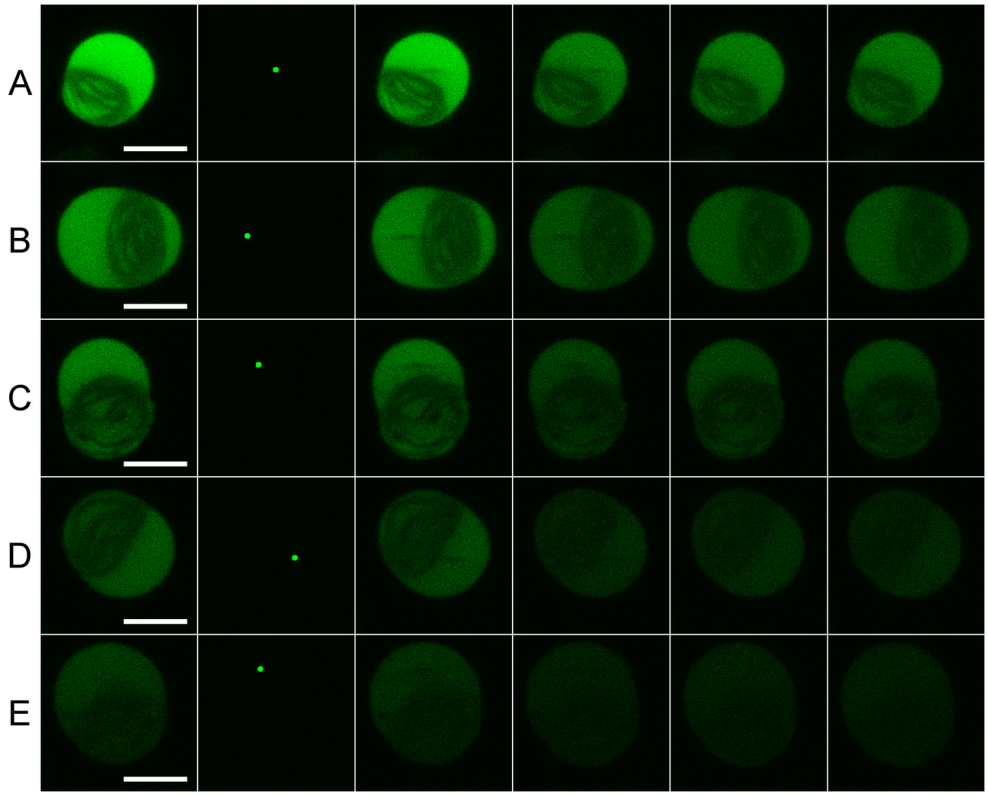

Figure 3.7: Observational control: TP-GFP. Rows of five experimental repetitions **(A-E)** are shown (different chloroplasts). Later frames in each row show very similar levels of fluorescence to earlier frames in the row. The scale bar is 5 μm in length.

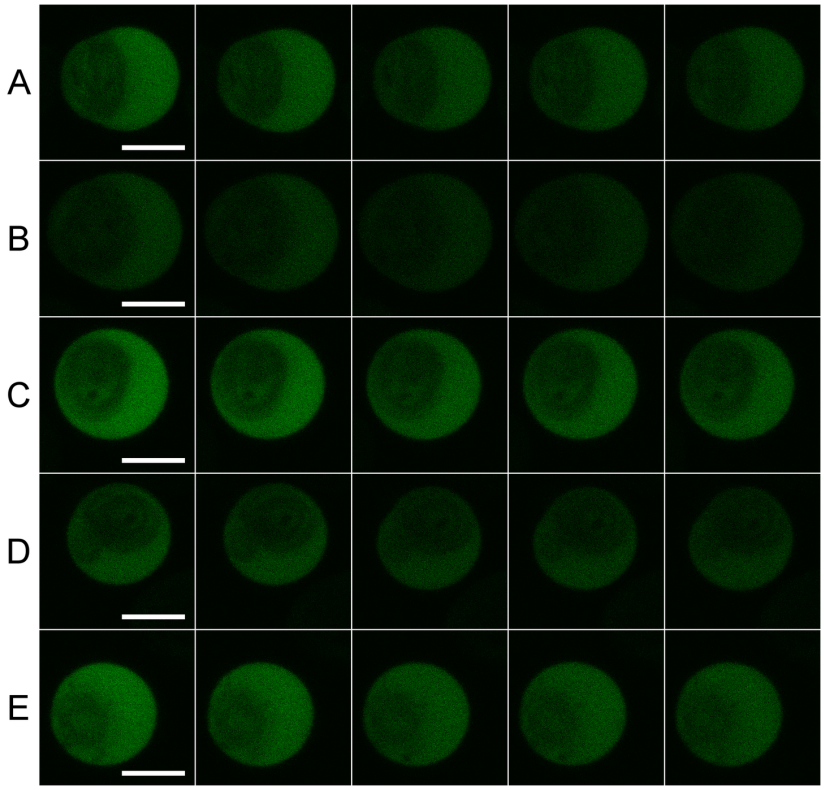

Figure 3.8: Modified FLIP: Hcf106-GFP (small bleach region). Rows of five experimental repetitions **(A-E)** are shown (different chloroplasts). Later frames in each row show very similar levels of fluorescence to earlier frames in the row. The scale bar is 5 μm in length. The bleach region is strikingly apparent in the first post-bleach images (column 5) and even at the last of twenty post-bleach acquisitions (column 6).

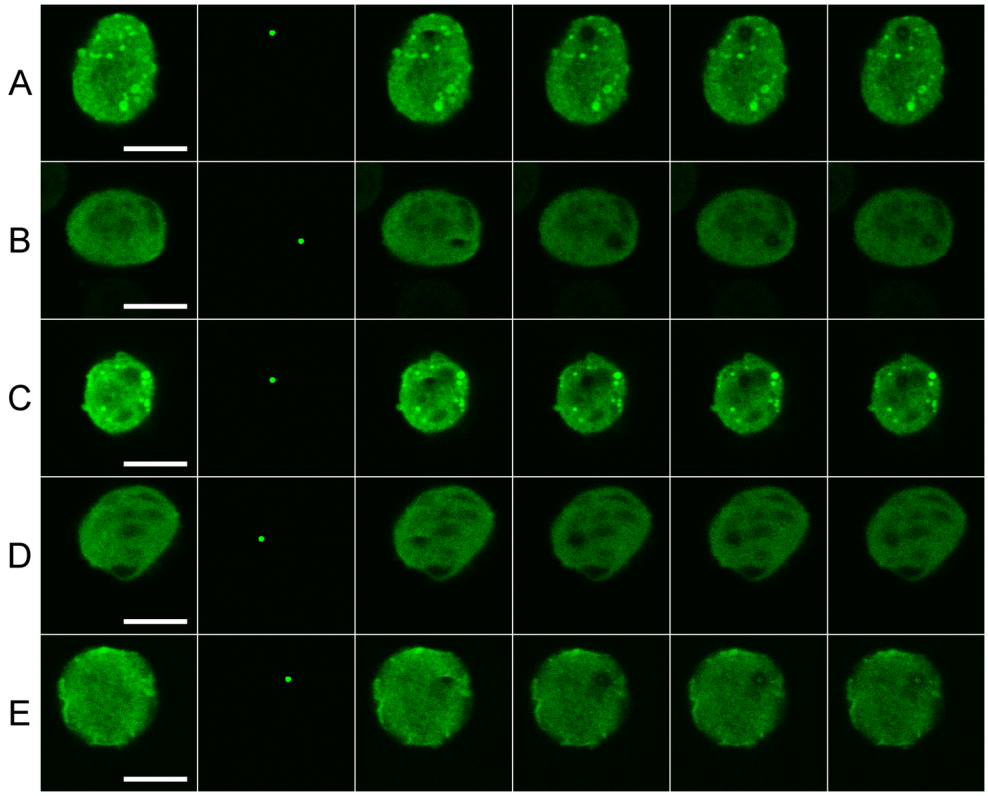

Figure 3.9: Observational control: Hcf106-GFP. Rows of five experimental repetitions **(A-E)** are shown (different chloroplasts). Later frames in each row show very similar levels of fluorescence to earlier frames in the row. The scale bar is 5 μm in length.

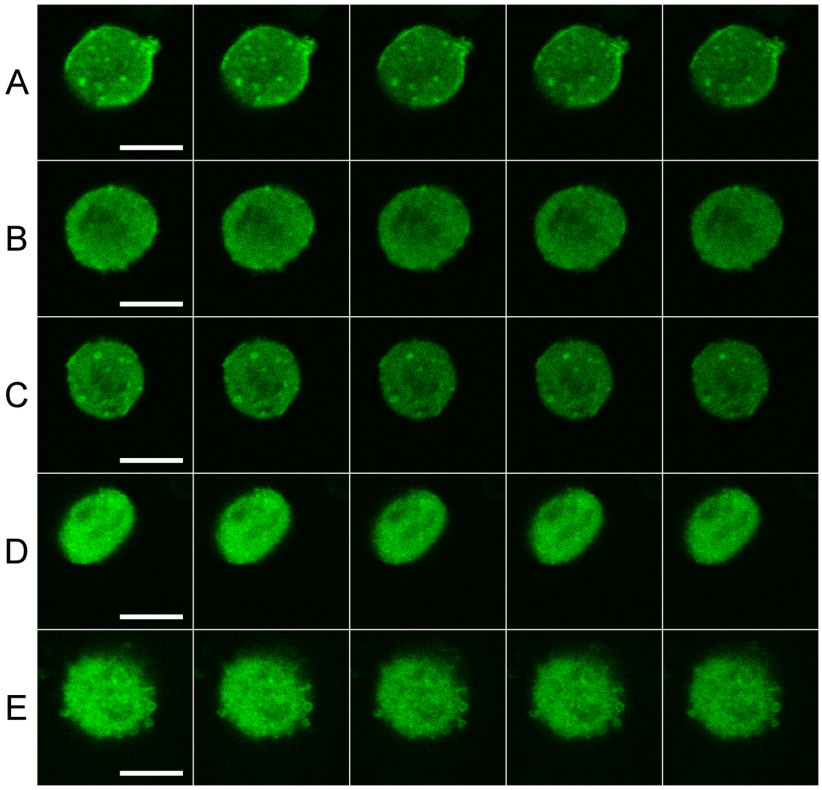

Figure 3.10: Fluorescence depletion: small bleach region FLIP. Each quadrant shows the spot photobleaching effect (five repetitions with pointwise standard deviation, s.d., shown) as compared to the observational photobleaching (five repetitions with pointwise standard deviation shown). The FLIP spot photobleaching has the most pronounced effect in **(A)** and **(D)** suggesting greater mobility. The pointwise standard deviation is greatest in **(D)**, for both observation and FLIP, which suggests a greater range of binding and dynamic processes are involved.

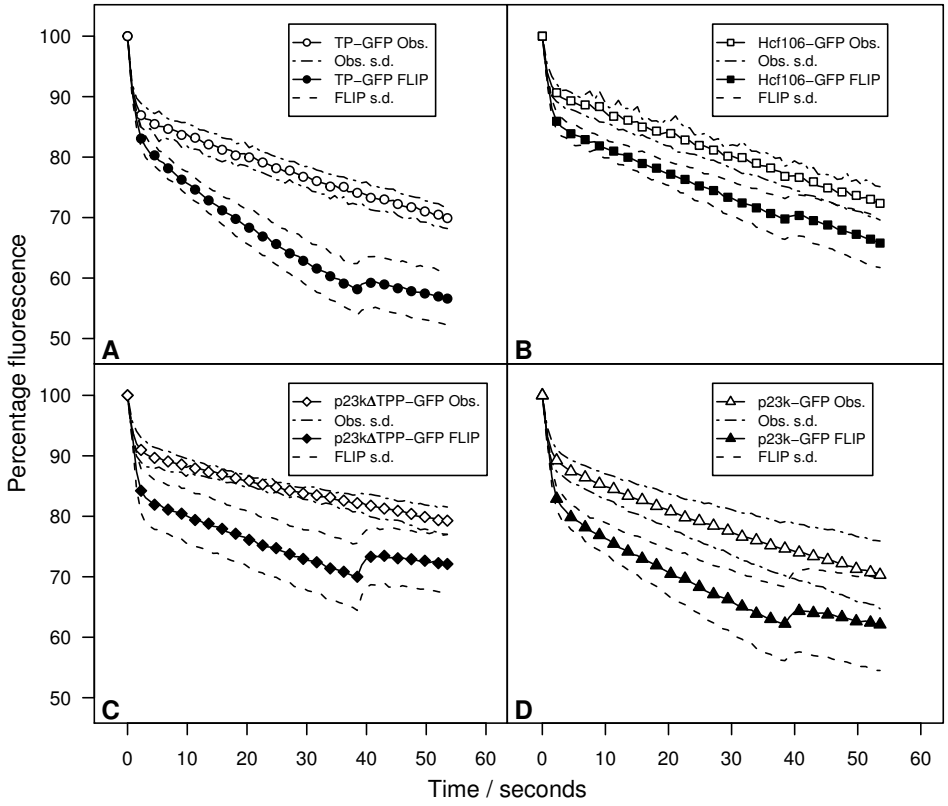

Figure 3.11: Correcting for observation: small bleach region. The fluorescence profiles with observational photobleaching effect removed are shown in **(A)**. TP-GFP shows the greatest rate of fluorescence depletion during photobleaching and Hcf106-GFP shows only a small rate of loss. A quantification of the fluorescence loss during spot photobleaching (the approximately linear portion after the initial drop and before the recovery) is shown in **(B)**. The standard deviation is shown at the top of each bar.

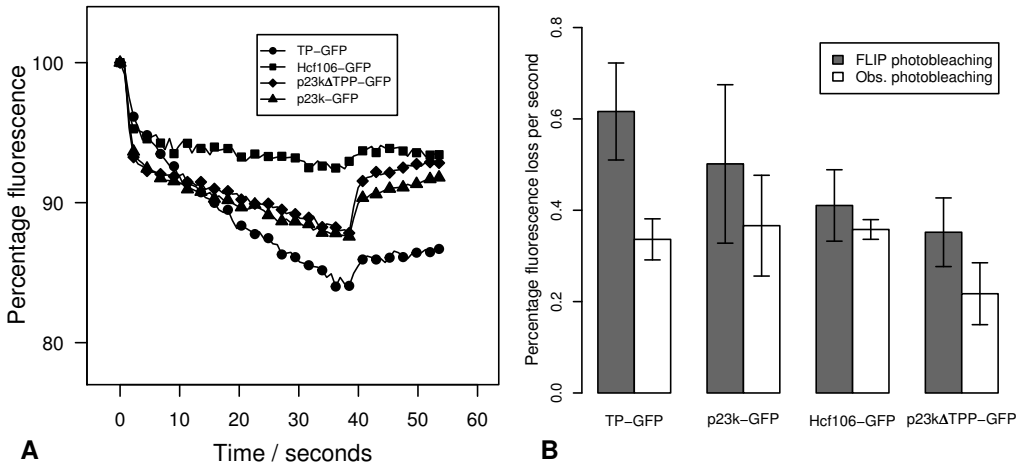

3.1.2 Large Bleach Region Modified FLIP

In order to better separate the constructs pre23k-GFP and pre23kΔTPP-GFP that are seen to give very close observation-corrected graphs in figure 3.11, a larger bleach region of 1 μm diameter was used for the modified FLIP procedure. The TP-GFP construct was omitted to allow the increase of the number of repetitions was from five to six with the intention of performing formal statistical analyses but it was later decided it would be an abuse of statistical inference methods to blindly employ tests of significance for a system with a high number of random variables with unknown distributions.

Although the level of expressed fluorescence appears to be lower in this data series compared to the previous data series, there are striking features such as seen in all the repetitions in figures 3.12, 3.14 and figure 3.16 where the mobility of the Tat substrates contrasts clearly with the immobility of the membrane bound Hcf106-GFP. Panel **(C)** of figure 3.18 has an extended scale to show the greater mobility of the mixed population pre23k-GFP construct whereas the signal peptide of pre23kΔTPP-GFP causes reduced mobility by a greater degree of membrane association.

Figure 3.12: Modified FLIP: pre23kΔTPP-GFP (large bleach region). Rows of six experimental repetitions **(A-F)** are shown (different chloroplasts). Later frames in each row show slightly lower levels of fluorescence than earlier frames in the row. The scale bar is 5 μm in length.

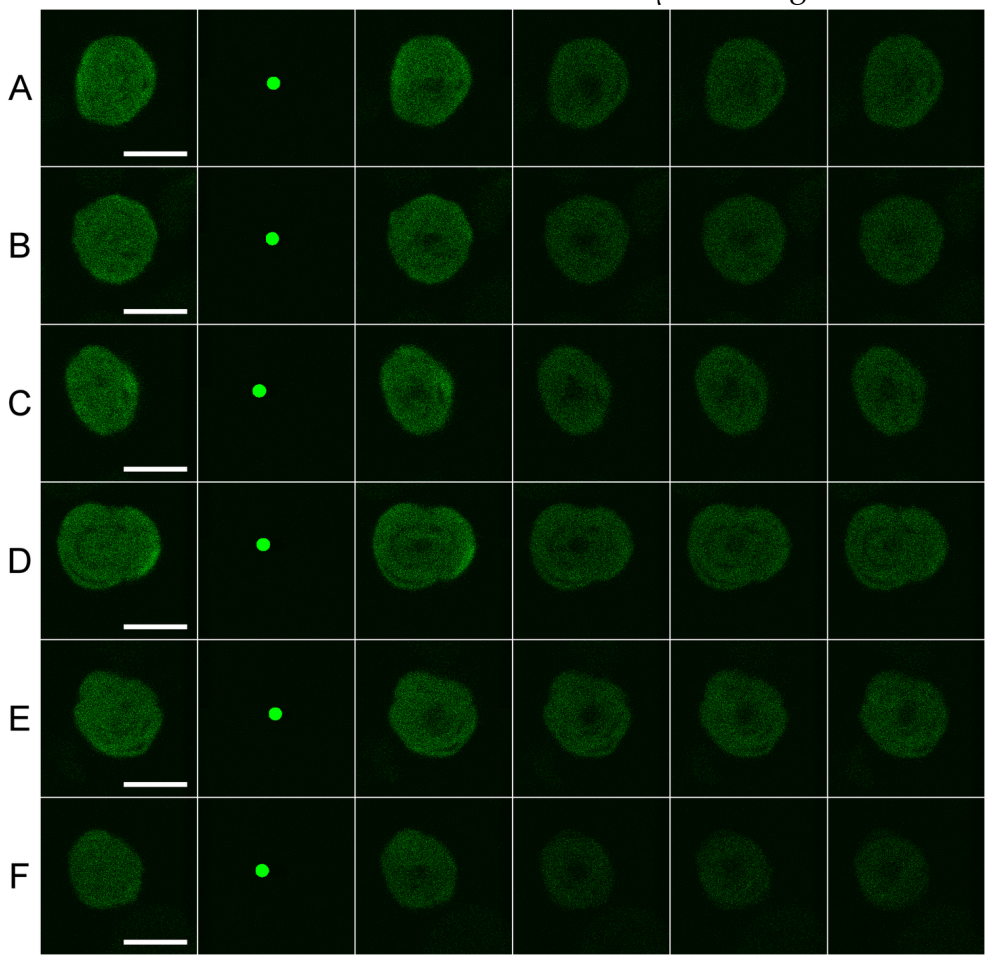

Figure 3.13: Observational control: pre23k-GFPΔTPP. Rows of six experimental repetitions **(A-F)** are shown (different chloroplasts). Later frames in each row show very similar levels of fluorescence to earlier frames in the row. The scale bar is 5 μm in length.

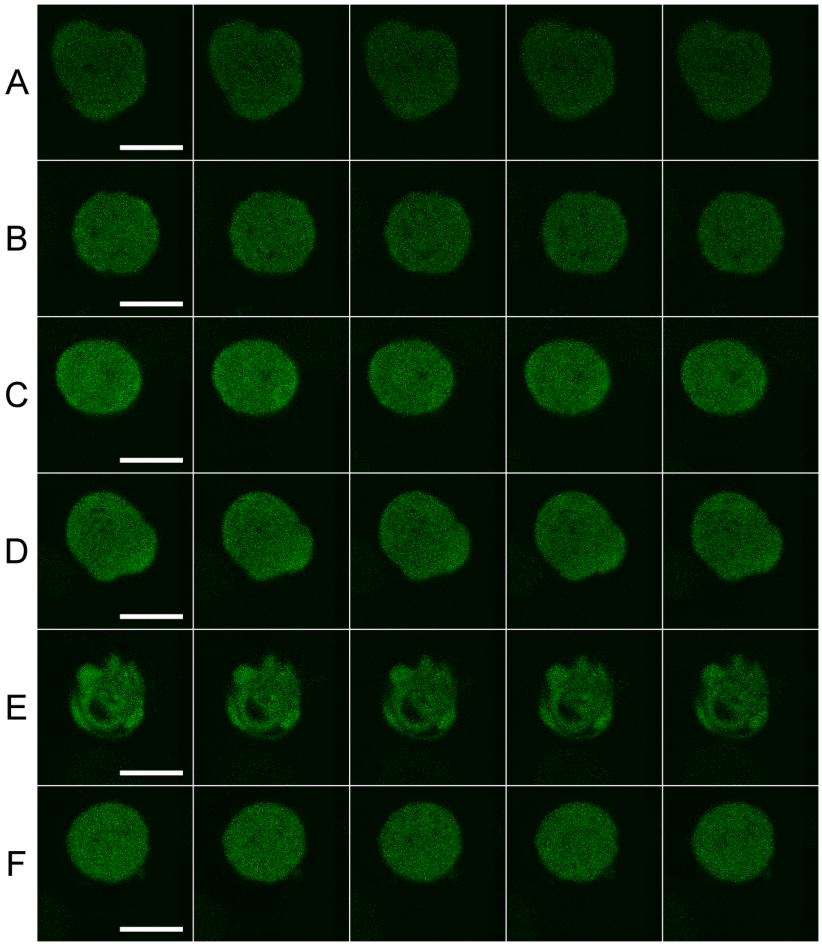

Figure 3.14: Modified FLIP: pre23k-GFP (large bleach region). Rows of six experimental repetitions **(A-F)** are shown (different chloroplasts). Later frames in each row show lower levels of fluorescence than earlier frames in the row. The scale bar is 5 μm in length.

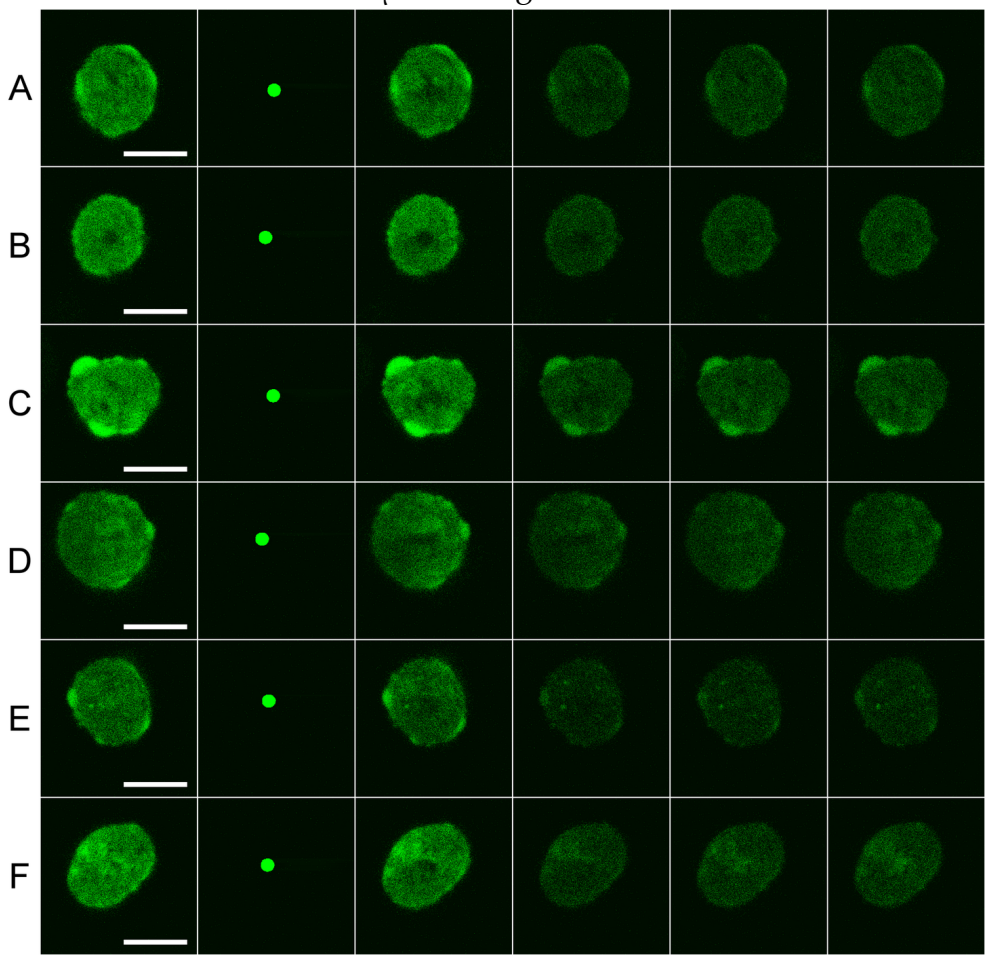

Figure 3.15: Observational control: pre23k-GFP. Rows of six experimental repetitions **(A-F)** are shown (different chloroplasts). Later frames in each row show very similar levels of fluorescence to earlier frames in the row. The scale bar is 5 μm in length.

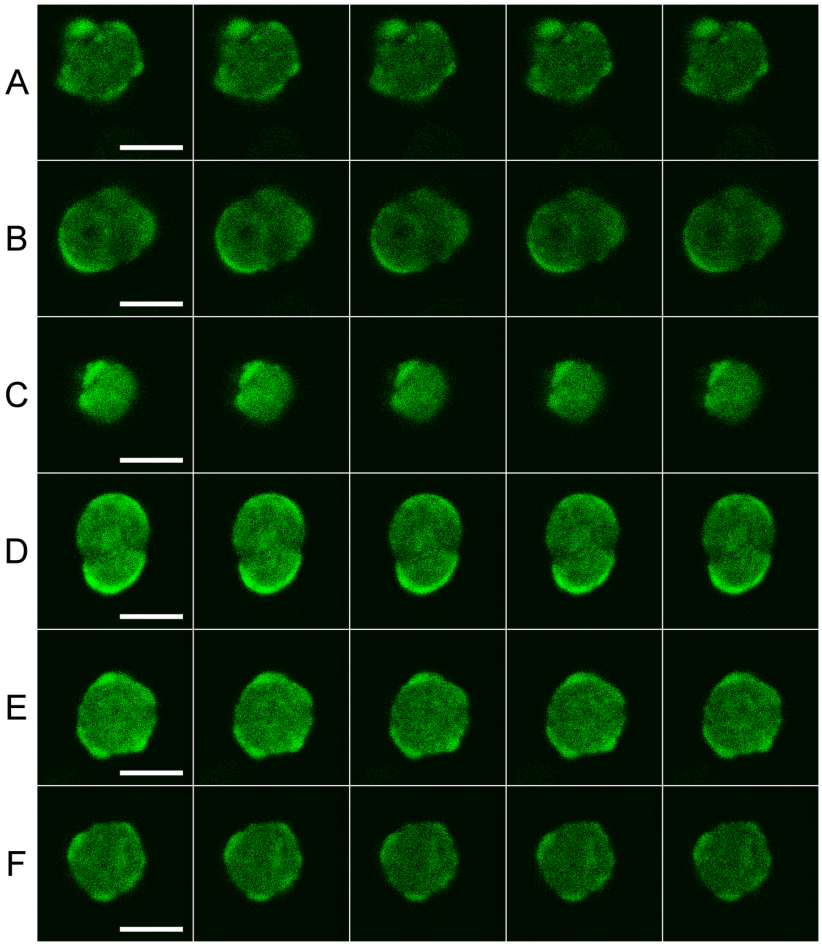

Figure 3.16: Modified FLIP: Hcf106-GFP (large bleach region). Rows of six experimental repetitions **(A-F)** are shown (different chloroplasts). Later frames in each row show very similar levels of fluorescence to earlier frames in the row. The scale bar is 5 μm in length.

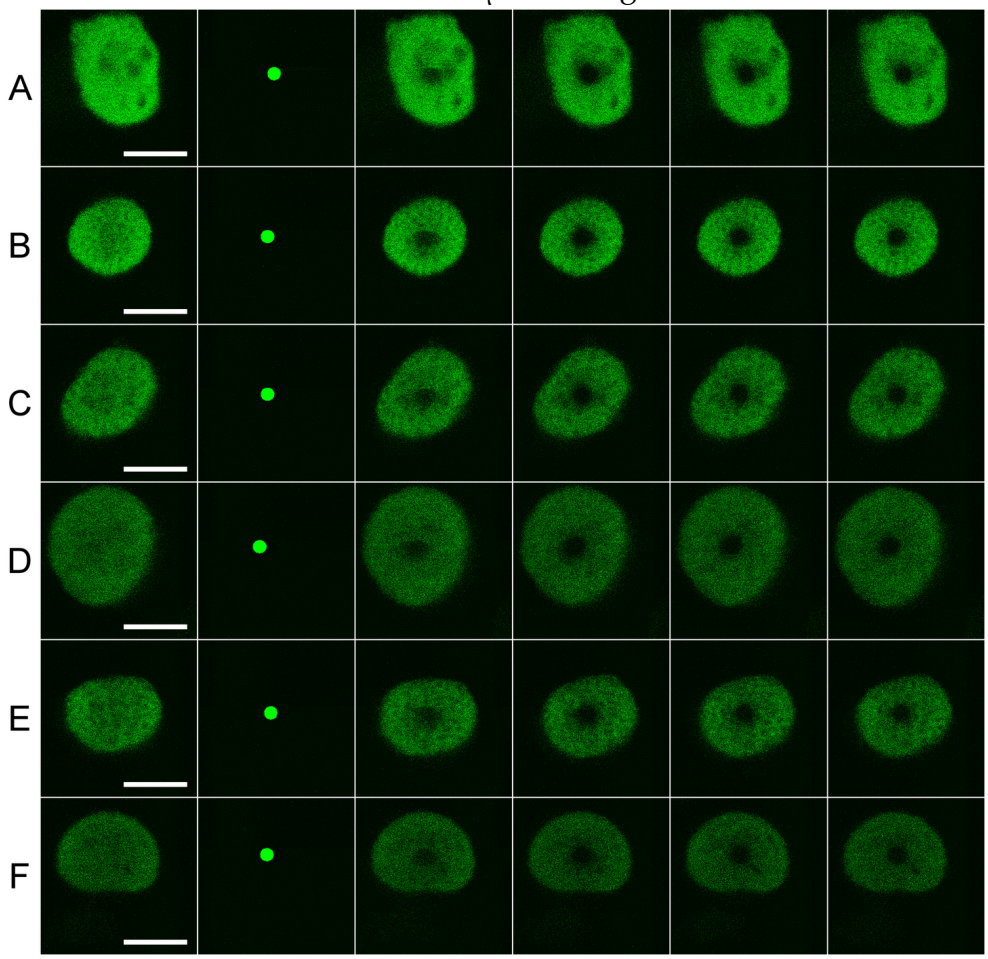

Figure 3.17: Observational control: Hcf106-GFP. Rows of six experimental repetitions **(A-F)** are shown (different chloroplasts). Later frames in each row show very similar levels of fluorescence to earlier frames in the row. The scale bar is 5 μm in length.

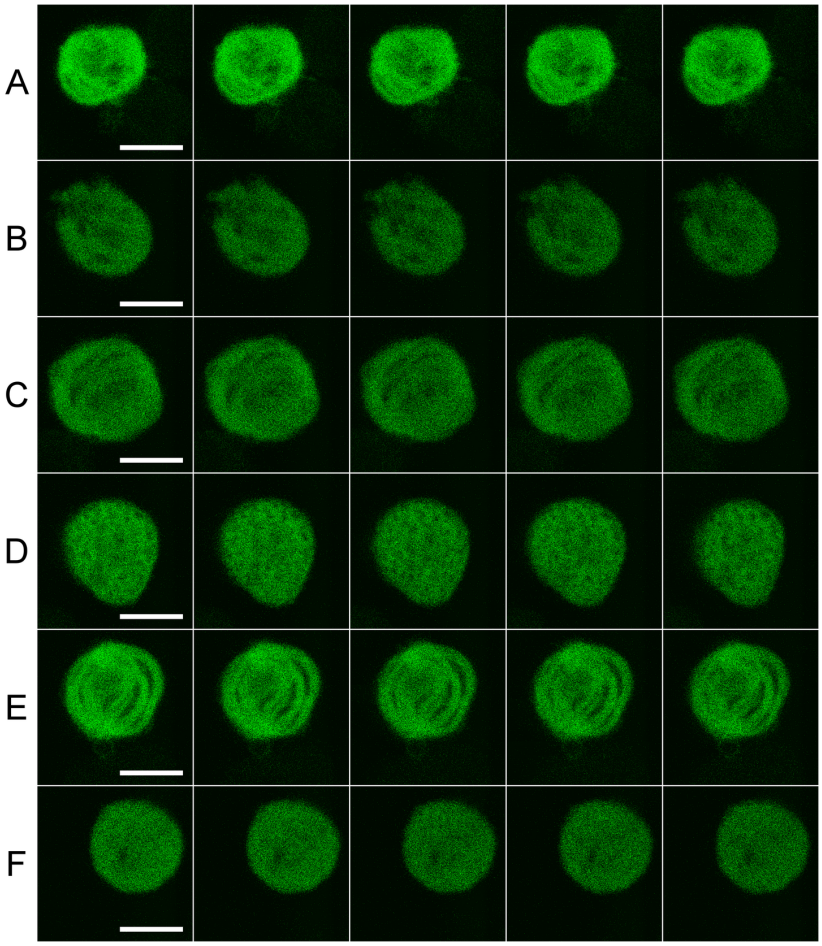

Figure 3.18: Fluorescence depletion: large bleach region FLIP. The panels show the spot photobleaching effect (six repetitions with pointwise standard deviation, s.d.) as compared to the observational photobleaching (six repetitions with pointwise standard deviation). The larger bleach region shows a much larger rate of depletion in **(C)** where the vertical scale must be adjusted to capture the full range of the profile.

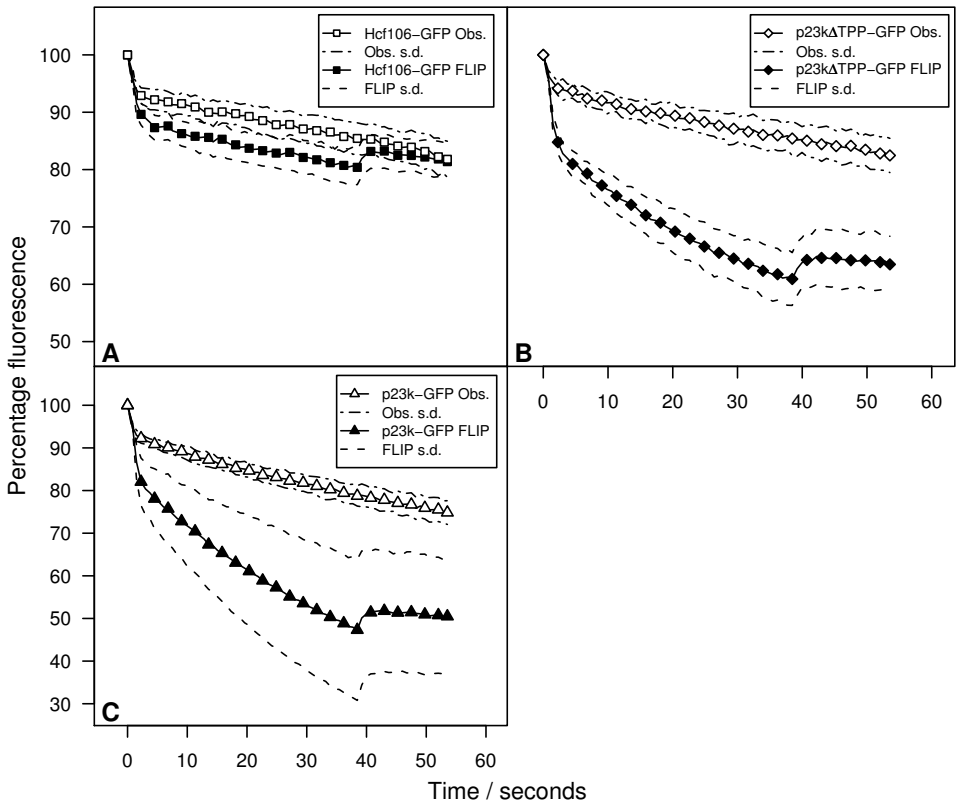

Figure 3.19: Correcting for observation: large bleach region. The fluorescence profiles with observational photobleaching effect removed are shown in **(A)**. The Tat substrates are better distinguished with the larger bleach region and emphasis is given to the immobility of Hcf106-GFP. A quantification of the fluorescence loss during spot photobleaching (the approximately linear portion after the initial drop and before the recovery) is shown in **(B)**. The standard deviation is shown at the top of each bar.

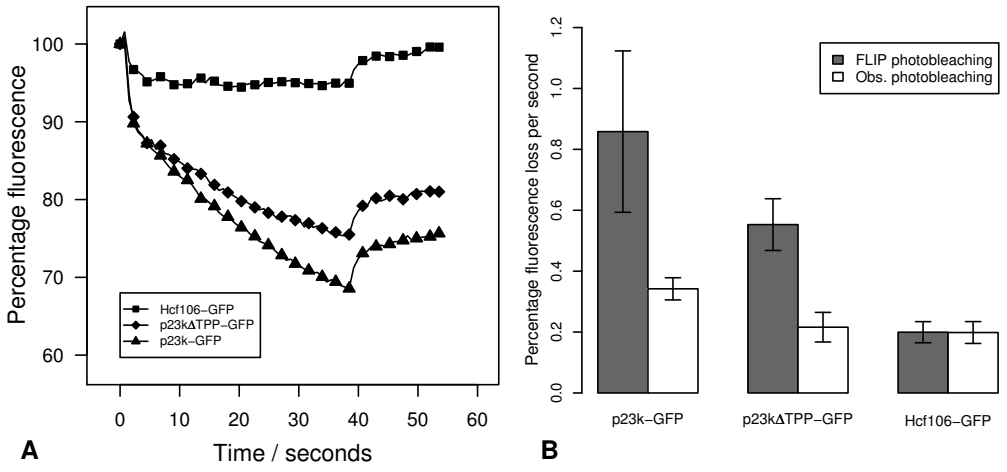

3.1.3 Signal Peptide Influence on Tat Substrates *in vivo*

The expectation at the outset was that the Tat substrate would diffuse in a non-directed way towards the Tat translocase as illustrated by **(D)** in figure 3.1 or that we would be unlikely to detect appreciable effects of thylakoid membrane association of the Tat substrate above the expected experimental variability.

Observational photobleaching What we found was, contrary to the high heterogeneity of the chloroplasts, the fluorescence depletion curves in figures 3.10 and 3.18 showed remarkably little variability for each construct. The variability tended to be less for observation-only than with spot photobleaching and we point to panels **(A-C)** of figure 3.10 and all panels of figure 3.18 for observational depletion within surprisingly narrow pointwise standard deviation bands. The high variability for observation that stands out is for the small spot bleach modified FLIP for pre23k-GFP in panel **(D)** of figure 3.10 which is to be expected as the pre23k-GFP construct is expected to have the most heterogeneous population of fluorescent protein with differing mobilities.

FLIP spot photobleaching Spot photobleaching tended to give greater variability as seen for **(D)** pre23k-GFP in figure 3.10 and **(C)** pre23k-GFP. The retardation of both the Tat substrate pre23k-GFP and pre23kΔTPP-

GFP as compared to TP-GFP is shown clearly in figure 3.11. The *in vivo* data presented here is signficant in itself as it represents the first attempt at a dynamic analysis of the Tat substrate in chloroplasts and it is already clear that the influence of the signal peptide is pronounced even before the translocation event. We further analyze this data with the help of simulation so that we can be sure we have a reliable interpretation of the Tat substrate dynamics.

Chapter 4

d-Binary Tree Partition of Unity Method

Important aspects of the numerical method, the *d*-Binary Tree Partition of Unity Method, are presented. Details for implementing the method in a computer program are described as these details allow the program to be run on not just one single computer but on many tens of computers. Results are presented where the PUM program has been run on 64 computers with each of these individual computers, or nodes, carrying out its portion of the calculation and combining results at appropriate stages. Mathematical equations are presented which show how various quantities of interest may be calculated by all the nodes in parallel so that the time taken to finish the calculation increases reasonably as the detail and size of the

calculation increases; which is to say that the calculation scales reasonably with problem size.

4.1 The *d*-Binary Tree

A *d*-binary tree-based cover is employed to enable a high performance C/C++ implementation of the Partition of Unity Method and we will use this implementation to make direct use of the temporal confocal image data series gathered. We present the most important aspects of our implementation that allows highly efficient execution on workstations and supercomputers.

The Partition of Unity Method does not yet have established domains of applications and this makes PUM an interesting research topic but shifts the focus on to more basic and low level considerations. We present results that will aid other researchers in using the Partition of Unity Method. Due to the novelty of the method, we have emphasized simplicity and clarity over raw computational efficiency.

Scale and Type of Computation An implementation of PUM based on a *d*-binary tree presents a structured computation without compromising resolution of the geometry. This structure is similar to the rigidity of the

finite difference method that has allowed terascale and petascale computations. In order for PUM to move from an interesting topic in numerical analysis to more general usage, it must demonstrate some real and significant advantage over established methods. The finite element method was able to establish itself by showing its superiority in structural mechanics (Clough, 1990). The choice of PUM for our application was motivated for its suitability for complex domains that are important for biology and although we present PUM with an easy outer boundary, the convenience of having our own implementation meant we were able to go on to capture the internal inhomogeneity of the chloroplast.

Particles are often superfluous Our group's work with PUM suggested that both a particle distribution and an internal meshing of a region are superfluous computational artifacts for our reaction-diffusion simulations. The *d*-binary tree implementation presented is able to perform calculations on a domain with a crude representation of the boundary, when the boundary is unimportant, or to fully resolve a polygonal boundary in a way that is consistent with the integration scheme employed in the interior.

4.1.1 Creation of the Keys

Keys are stored as STL `string`s of the form `"0-1-2-3"`. The basic operation with our handling of a *d*-binary tree in 2D is the creation of a certain number

r of complete refinements from some key k. This is done recursively using `recursive_modify_keys`. If r complete refinements are requested, the result will be 4^r keys. Memory for all the 4^r keys is allocated in an STL `vector` of `string` and initialized to the base key k lengthened to the final key length (right-padded with "`-0`") so that the key `string`s do not have to be dynamically extended.

The function `recursive_modify_keys` takes three self-documenting arguments: an integer `level_to_modify`, an iterator `position_to_begin` and an integer `number_to_operate_on`.

A total of `number_to_operate_on` elements are modified beginning at `position_to_begin`. The `level_to_modify` key position of the first (`number_to_operate_on`/4) elements is set to '`0`'. The same key position of the subsequent three blocks of (`number_to_operate_on`/4) is set to '`1`', '`2`' and '`3`' respectively. The function `recursive_modify_keys` is called again four times with `level_to_modify` incremented by one, `number_to_operate_on` set to (`number_to_operate_on`/4), and the iterator `position_to_begin` set to the respective first elements of the four blocks that were collectively modified.

Table 4.1: In-place recursive key generation. Each rectangle represents a single call to `recursive_modify_keys` and the entries within are modified together.

0	–	0	–	0
0	–	0	–	1
0	–	0	–	2
0	–	0	–	3
0	–	1	–	0
0	–	1	–	1
0	–	1	–	2
0	–	1	–	3
0	–	2	–	0
0	–	2	–	1
0	–	2	–	2
0	–	2	–	3
0	–	3	–	0
0	–	3	–	1
0	–	3	–	2
0	–	3	–	3

4.1.2 Creation of a *d*-Binary Tree

A `refinement_structure` is used to represent the *d*-binary tree: within the `refinement_structure`, a `C++` STL `map` is used to describe the number of complete refinements that should be made from particular keys in order to produce the final configuration of the tree. The keys are present in the `map` in order of increasing level so that the `map` can be traversed once to create the final tree.

This data structure allows a compact representation of certain refine-

ment of the computational domain and it is expected to ease the transfer of information between distributed memory nodes of a computation.

The initial tree begins with the single key `"0"`. The `refinement_structure map` is made up of pairs (k, r) of a key k and an integer r. The tree creation is carried out as follows

1. Take the next pair (k, r).
2. Remove k from the tree.
3. Insert the keys that are r refinement levels from k into the tree.
4. Repeat from 1. until the end of `map`.

4.1.3 Neighbour Search

The neighbours of a patch in the d-binary tree may be determined without the need for an expensive search by projecting the key to a binary tree key in the x and y directions. The binary tree neighbours of the projected keys are easily determined and these are then used to form the keys for the higher dimensional d-binary tree.

4.2 Parallel Calculation of Integrals and Norms

Error norms are calculated for convergence testing and PUM function integrals are needed to check for conservation and depletion in instationary reaction-diffusion simulations. We show how these integrals may be calculated using matrix-vector and vector-vector operations that may be carried out in parallel to avoid the naïve strategy of direct quadrature carried out on the PUM solution and perhaps another function of interest.

$$\|u\|_{L^2(\Omega)} = \left(\int_\Omega |u|^2 \, \mathrm{d}x \right)^{\frac{1}{2}}$$
$$\|u\|_{H^1(\Omega)} = \left(\int_\Omega |u|^2 \, \mathrm{d}x + \int_\Omega |\nabla u|^2 \, \mathrm{d}x \right)^{\frac{1}{2}}$$

An important aspect that allows for fast, efficient execution is the linearity inherent in PUM. It will be shown how certain integrals may be obtained by simple matrix-vector and vector-vector operations in such a way that certain matrices and vectors may be stored to avoid repeated numerical integration. In subsequent paragraphs, an expression will be written in a form that may involve either vectors or matrices or both. The integral of the expression will then be deduced where certain matrix or vector entries appear in integral form: the correctness of this is most evident from the last equality just before matrices and vectors become involved.

4.2.1 Integrals Without Basis Function Derivatives

Parallel Partition of Unity Integration The partition of unity may be used to parallelize an integration over many computer CPUs. (Carpinteri et al., 2002)

$$\begin{aligned} f &= \left(\sum_{i=1}^{I} \varphi_i\right) f \\ &= \sum_{i=1}^{I} (\varphi_i f) \\ \implies \qquad \int_\Omega f \,\mathrm{d}x &= \sum_{i=1}^{I} \left(\int_\Omega \varphi_i f \,\mathrm{d}x\right) \end{aligned}$$

As f is an arbitrary function, we can deduce

$$\begin{aligned} \int_\Omega f^2 \,\mathrm{d}x &= \sum_{i=1}^{I} \left(\int_\Omega \varphi_i f^2 \,\mathrm{d}x\right) \\ \int_\Omega |\nabla f|^2 \,\mathrm{d}x &= \int_\Omega \nabla f \cdot \nabla f \,\mathrm{d}x \\ &= \sum_{i=1}^{I} \left(\int_\Omega \varphi_i \nabla f \cdot \nabla f \,\mathrm{d}x\right) \end{aligned}$$

Integration of PUM approximation The integral of a PUM approximation over the domain Ω may be easily computed by a vector dot product. If numerical integration were to be applied to the PUM solution directly, the cost would be equivalent to assembling the vector of trial function

integrals shown below and the cost would be severe if carried out at each time step for an instationary problem.

$$
\begin{aligned}
u^h &= \sum_{i=1}^{N} q_i \Phi_i \\
&= \begin{pmatrix} \Phi_1 & \cdots & \Phi_N \end{pmatrix} \begin{pmatrix} q_1 \\ \vdots \\ q_N \end{pmatrix} \\
\implies \quad \int_\Omega u^h \, \mathrm{d}x &= \begin{pmatrix} \int_\Omega \Phi_1 \, \mathrm{d}x & \cdots & \int_\Omega \Phi_N \, \mathrm{d}x \end{pmatrix} \mathbf{q}
\end{aligned}
$$

Replacing u^h by $f u^h$ we may deduce

$$
\int_\Omega f u^h \, \mathrm{d}x = \begin{pmatrix} \int_\Omega f \Phi_1 \, \mathrm{d}x & \cdots & \int_\Omega f \Phi_N \, \mathrm{d}x \end{pmatrix} \mathbf{q}
$$

to evaluate PUM approximation-function products. The function f may be chosen to be unity in a subset of the domain and zero everywhere else in order to limit the domain of integration; this is done to evaluate integrals in some region of interest, for example. It is readily seen that the same vector of integrals is exactly the RHS vector for a Galerkin projection of f onto the global basis $\{\Phi_i\}_{i=1}^N$.

RHS assembly Projections between different PUM spaces may be efficiently implemented by using matrix-vector operations to form the RHS of the projection system. Matrix vector operations may also be used to aid in calculating the RHS in instationary problems and for when linear terms

are involved.

$$\begin{aligned}
\Psi_j u^h &= \sum_{i=1}^{N} q_i \Psi_j \Phi_i \\
&= \begin{pmatrix} \Psi_j \Phi_1 & \cdots & \Psi_j \Phi_N \end{pmatrix} \begin{pmatrix} q_1 \\ \vdots \\ q_N \end{pmatrix} \\
\implies \qquad \int_\Omega \Psi_j u^h \, \mathrm{d}x &= \begin{pmatrix} \int_\Omega \Psi_j \Phi_1 \, \mathrm{d}x & \cdots & \int_\Omega \Psi_j \Phi_N \, \mathrm{d}x \end{pmatrix} \begin{pmatrix} q_1 \\ \vdots \\ q_N \end{pmatrix} \\
\implies \qquad \begin{pmatrix} \int_\Omega \Psi_1 u^h \, \mathrm{d}x \\ \vdots \\ \int_\Omega \Psi_M u^h \, \mathrm{d}x \end{pmatrix} &= \begin{pmatrix} \int_\Omega \Psi_1 \Phi_1 \, \mathrm{d}x & \cdots & \int_\Omega \Psi_1 \Phi_N \, \mathrm{d}x \\ \vdots & \ddots & \vdots \\ \int_\Omega \Psi_M \Phi_1 \, \mathrm{d}x & \cdots & \int_\Omega \Psi_M \Phi_N \, \mathrm{d}x \end{pmatrix} \begin{pmatrix} q_1 \\ \vdots \\ q_N \end{pmatrix}
\end{aligned}$$

Products of PUM approximations The product of two PUM approximations may be found efficiently without requiring they share the same global

basis.

$$
\begin{aligned}
v^h u^h &= \left(\sum_{j=1}^{M} r_j \Psi_j\right)\left(\sum_{i=1}^{N} q_i \Phi_i\right) \\
&= \sum_{j=1}^{M}\left(r_j \sum_{i=1}^{N} q_i \Psi_j \Phi_i\right) \\
&= \begin{pmatrix} r_1 & \cdots & r_M \end{pmatrix}\begin{pmatrix} \sum_{i=1}^{N} q_i \Psi_1 \Phi_i \\ \vdots \\ \sum_{i=1}^{N} q_i \Psi_M \Phi_i \end{pmatrix} \\
&= \mathbf{r}^T \begin{pmatrix} \Psi_1\Phi_1 & \cdots & \Psi_1\Phi_N \\ \vdots & \ddots & \vdots \\ \Psi_M\Phi_1 & \cdots & \Psi_M\Phi_N \end{pmatrix}\begin{pmatrix} q_1 \\ \vdots \\ q_N \end{pmatrix} \\
\implies \int_\Omega v^h u^h \,\mathrm{d}x &= \mathbf{r}^T \begin{pmatrix} \int_\Omega \Psi_1\Phi_1 \,\mathrm{d}x & \cdots & \int_\Omega \Psi_1\Phi_N \,\mathrm{d}x \\ \vdots & \ddots & \vdots \\ \int_\Omega \Psi_M\Phi_1 \,\mathrm{d}x & \cdots & \int_\Omega \Psi_M\Phi_N \,\mathrm{d}x \end{pmatrix}\mathbf{q}
\end{aligned}
$$

Replacing $v^h u^h$ by $f v^h u^h$ it may be readily deduced that

$$
\int_\Omega f v^h u^h \,\mathrm{d}x = \mathbf{r}^T \begin{pmatrix} \int_\Omega f\Psi_1\Phi_1 \,\mathrm{d}x & \cdots & \int_\Omega f\Psi_1\Phi_N \,\mathrm{d}x \\ \vdots & \ddots & \vdots \\ \int_\Omega f\Psi_M\Phi_1 \,\mathrm{d}x & \cdots & \int_\Omega f\Psi_M\Phi_N \,\mathrm{d}x \end{pmatrix}\mathbf{q}
$$

Making use of this matrix, a suitable f may be chosen to account for reaction terms of the form fu. An example is where f describes a sink effect in a certain region of the domain: f is negative only on a small subset of the domain and this may be interpreted as a bleach region.

4.2.2 Integrals Involving Basis Function Derivatives

Dot product of function, approximation gradients

$$
\begin{aligned}
\nabla u^h \cdot \nabla f &= \sum_{k=1}^{d} \frac{\partial u^h}{\partial x_k} \frac{\partial f}{\partial x_k} \\
&= \sum_{k=1}^{d} \left(\sum_{i=1}^{N} q_i \frac{\partial \Phi_i}{\partial x_k} \right) \frac{\partial f}{\partial x_k} \\
&= \sum_{k=1}^{d} \left(\sum_{i=1}^{N} q_i \frac{\partial \Phi_i}{\partial x_k} \frac{\partial f}{\partial x_k} \right) \\
&= \sum_{i=1}^{N} q_i \sum_{k=1}^{d} \frac{\partial \Phi_i}{\partial x_k} \frac{\partial f}{\partial x_k} \\
&= \sum_{i=1}^{N} q_i (\nabla \Phi_i) \cdot (\nabla f) \\
&= \begin{pmatrix} \nabla \Phi_1 \cdot \nabla f & \cdots & \nabla \Phi_N \cdot \nabla f \end{pmatrix} \begin{pmatrix} q_1 \\ \vdots \\ q_N \end{pmatrix}
\end{aligned}
$$

$$
\implies \qquad \int_\Omega (\nabla u^h) \cdot (\nabla f) \, \mathrm{d}x = \begin{pmatrix} \int_\Omega \nabla \Phi_1 \cdot \nabla f \, \mathrm{d}x & \cdots & \int_\Omega \nabla \Phi_N \cdot \nabla f \, \mathrm{d}x \end{pmatrix} \begin{pmatrix} q_1 \\ \vdots \\ q_N \end{pmatrix}
$$

Dot product of two approximation gradients

$$
\begin{aligned}
\nabla v^h \cdot \nabla u^h &= \sum_{k=1}^{d} \frac{\partial v^h}{\partial x_k} \frac{\partial u^h}{\partial x_k} \\
&= \sum_{k=1}^{d} \left(\sum_{j=1}^{M} r_j \frac{\partial \Psi_j}{\partial x_k} \right) \left(\sum_{i=1}^{N} q_i \frac{\partial \Phi_i}{\partial x_k} \right) \\
&= \sum_{j=1}^{M} r_j \sum_{i=1}^{N} q_i \sum_{k=1}^{d} \frac{\partial \Psi_j}{\partial x_k} \frac{\partial \Phi_i}{\partial x_k} \\
&= \sum_{j=1}^{M} r_j \sum_{i=1}^{N} q_i \nabla \Psi_j \cdot \nabla \Phi_i \\
&= \begin{pmatrix} r_1 & \cdots & r_M \end{pmatrix} \begin{pmatrix} \sum_{i=1}^{N} q_i \nabla \Psi_1 \cdot \nabla \Phi_i \\ \vdots \\ \sum_{i=1}^{N} q_i \nabla \Psi_M \cdot \nabla \Phi_i \end{pmatrix} \\
&= \mathbf{r}^T \begin{pmatrix} \nabla \Psi_1 \cdot \nabla \Phi_1 & \cdots & \nabla \Psi_1 \cdot \nabla \Phi_N \\ \vdots & \ddots & \vdots \\ \nabla \Psi_M \cdot \nabla \Phi_1 & \cdots & \nabla \Psi_M \cdot \nabla \Phi_N \end{pmatrix} \begin{pmatrix} q_1 \\ \vdots \\ q_N \end{pmatrix}
\end{aligned}
$$

$$
\implies \qquad \int_\Omega \nabla v^h \cdot \nabla u^h \, \mathrm{d}x = \mathbf{r}^T \begin{pmatrix} \int_\Omega \nabla \Psi_1 \cdot \nabla \Phi_1 \, \mathrm{d}x & \cdots & \int_\Omega \nabla \Psi_1 \cdot \nabla \Phi_N \, \mathrm{d}x \\ \vdots & \ddots & \vdots \\ \int_\Omega \nabla \Psi_M \cdot \nabla \Phi_1 \, \mathrm{d}x & \cdots & \int_\Omega \nabla \Psi_M \cdot \nabla \Phi_N \, \mathrm{d}x \end{pmatrix} \mathbf{q}
$$

In particular for $M = N$, $\Phi_i = \Psi_i$ for all i, and $\mathbf{q} = \mathbf{r}$; we can work out $(u^h)^2$.

4.3 Parallel Calculation of Norms

$$\begin{aligned}\|u-f\|_{L^2}^2 &= \int_\Omega |u-f|^2 \,\mathrm{d}x \\ &= \int_\Omega u^2 \,\mathrm{d}x - 2\int_\Omega uf \,\mathrm{d}x + \int_\Omega f^2 \,\mathrm{d}x\end{aligned}$$

$$\begin{aligned}\int_\Omega |\nabla(u-f)|^2 \,\mathrm{d}x &= \int_\Omega |\nabla u - \nabla f|^2 \,\mathrm{d}x \\ &= \int_\Omega (\nabla u - \nabla f)\cdot(\nabla u - \nabla f) \,\mathrm{d}x \\ &= \int_\Omega \sum_{i=1}^{d} \left(\frac{\partial u}{\partial x_i} - \frac{\partial f}{\partial x_i}\right)^2 \mathrm{d}x \\ &= \int_\Omega \sum_{i=1}^{d} \left(\frac{\partial u}{\partial x_i}\right)^2 \mathrm{d}x - 2\int_\Omega \sum_{i=1}^{d} \left(\frac{\partial u}{\partial x_i}\frac{\partial f}{\partial x_i}\right) \mathrm{d}x + \int_\Omega \sum_{i=1}^{d} \left(\frac{\partial f}{\partial x_i}\right)^2 \mathrm{d}x \\ &= \int_\Omega |\nabla u|^2 \,\mathrm{d}x - 2\int_\Omega \nabla u\cdot\nabla f \,\mathrm{d}x + \int_\Omega |\nabla f|^2 \,\mathrm{d}x\end{aligned}$$

$$\begin{pmatrix} \Phi_1\Phi_1 & \cdots & \Phi_1\Phi_N \\ \vdots & \ddots & \vdots \\ \Phi_N\Phi_1 & \cdots & \Phi_N\Phi_N \end{pmatrix} \begin{pmatrix} q_1 \\ \vdots \\ q_N \end{pmatrix} = \begin{pmatrix} \sum_i q_i \Phi_1\Phi_i \\ \vdots \\ \sum_i q_i \Phi_N\Phi_i \end{pmatrix}$$

4.4 Efficient Implementation of PUM

Rectangular Patches and Coordinate Transforms Let $\Omega \subset \mathbb{R}^d$ be covered by I rectangular patches $\{\omega_i\}_{i=1}^I$. The global coordinates $x = (x_1, \ldots, x_d)$ may be mapped to the local coordinates $[-1,1]^d$ of patch ω_i by the affine linear transformation $\zeta_i : \omega_i \to [-1,1]^d$ defined by

$$\zeta_i(x) = \left(\zeta_i^1(x), \ldots, \zeta_i^d(x)\right)$$

We will need to be able to take the gradient ∇_{ζ_i} with respect to this coordinate system.

$$\nabla_{\zeta_i} = \left(\frac{\partial}{\partial \zeta_i^1}, \ldots, \frac{\partial}{\partial \zeta_i^d}\right)$$

Partition of Unity and Weighting Functions Let $W : [-1,1]^d \to [0,1]$ be a suitable weighting function and we define W_i to be the weighting function on patch ω_i where

$$W_i(x) = W(\zeta_i(x))$$

We construct our partition of unity function $\varphi_i : \omega_i \to [0,1]$ using the W_i

$$\varphi_i(x) = \frac{W_i(x)}{\sum_{n \in N_i} W_n(x)}$$

where $N_i = \{n : 1 \leq n \leq I, \quad \omega_n \cap \omega_i \neq \emptyset\}$ is the set of indices of patches incident on ω_i. The $\{\omega_n\}_{n \in N_i}$ are called neighbours of ω_i.

Local and Global Approximation Functions Let $\{p_i^j\}_{j=1}^{J_i}$ be the set of J_i functions with good properties. These, for example, may be the set of monomials $p_i^j : [-1,1] \to \mathbb{R}$ in local coordinates on patch ω_i with $p_i^j(\zeta_i) = (\zeta_i)^{j-1}$. The j^{th} local approximation ψ_i^j function on patch ω_i is

$$\psi_i^j(x) = p_i^j(\zeta_i(x))$$

The gradient of the global functions is then

$$\begin{aligned}
\nabla(\varphi_i\psi_i^j) &= (\nabla\varphi_i)\psi_i^j + \varphi_i\nabla\psi_i^j \\
&= \left(\nabla\frac{W_i}{\sum_{n=1}^N W_n}\right)\psi_i^j + \varphi_i\nabla\psi_i^j \\
&= \left(\frac{(\nabla W_i)(\sum_{n=1}^N W_n) - W_i\sum_{n=1}^N \nabla W_n}{\left(\sum_{n=1}^N W_n\right)^2}\right)\psi_i^j + \varphi_i\nabla\psi_i^j
\end{aligned}$$

4.5 Numerical Integration in the Interior

Interior box integral

$$x = \frac{x_a + x_b}{2} + \xi\,\frac{x_b - x_a}{2}$$
$$y = \frac{y_a + y_b}{2} + \eta\,\frac{y_b - y_a}{2}$$

$$\left|\frac{\partial(x,y)}{\partial(\xi,\eta)}\right| = \begin{vmatrix} \frac{\partial x}{\partial \xi} & \frac{\partial x}{\partial \eta} \\ \frac{\partial y}{\partial \xi} & \frac{\partial y}{\partial \eta} \end{vmatrix} = \begin{vmatrix} \frac{\partial x}{\partial \xi} & 0 \\ 0 & \frac{\partial y}{\partial \eta} \end{vmatrix}$$
$$= \frac{(x_b - x_a)(y_b - y_a)}{4}$$

$$\int_{y_a}^{y_b}\int_{x_a}^{x_b} f(x,y)\,\mathrm{d}x\,\mathrm{d}y = \int_{\eta_a}^{\eta_b}\int_{\xi_a}^{\xi_b} f(\xi,\eta)\left|\frac{\partial(x,y)}{\partial(\xi,\eta)}\right|\,\mathrm{d}\xi\,\mathrm{d}\eta$$
$$\approx \sum_{j=1}^{q_\eta} w_j^\eta \int_{\xi_a}^{\xi_b} f(\xi,\eta_j)\left|\frac{\partial(x,y)}{\partial(\xi,\eta)}\right|\,\mathrm{d}\xi$$
$$\approx \sum_{j=1}^{q_\eta} w_j^\eta \sum_{i=1}^{q_\xi} w_i^\xi f(\xi_i,\eta_j)\left|\frac{\partial(x,y)}{\partial(\xi,\eta)}\right|$$

Cartesian coordinates parametrization We give the equations for the case when the boundary runs in a vertical direction through our box of interest.

$$x = \frac{x_a(y) + x_b(y)}{2} + \xi\,\frac{x_b(y) - x_a(y)}{2}$$
$$y = \frac{y_a + y_b}{2} \qquad + \eta\,\frac{y_b - y_a}{2}$$

$$\left|\frac{\partial(x,y)}{\partial(\xi,\eta)}\right| = \begin{vmatrix} \frac{\partial x}{\partial \xi} & \frac{\partial x}{\partial \eta} \\ \frac{\partial y}{\partial \xi} & \frac{\partial y}{\partial \eta} \end{vmatrix} = \begin{vmatrix} \frac{\partial x}{\partial \xi} & \frac{\partial x}{\partial \eta} \\ 0 & \frac{\partial y}{\partial \eta} \end{vmatrix}$$
$$= \frac{\Big(x_b(y) - x_a(y)\Big)(y_b - y_a)}{4}$$

$$\int_{y_a}^{y_b} \int_{x_a(y)}^{x_b(y)} f(x,y)\,\mathrm{d}x\,\mathrm{d}y = \int_{\eta_a}^{\eta_b} \int_{\xi_a}^{\xi_b} f(\xi,\eta) \left|\frac{\partial(x,y)}{\partial(\xi,\eta)}\right| \,\mathrm{d}\xi\,\mathrm{d}\eta$$
$$\approx \sum_{j=1}^{q_\eta} w_j^\eta \sum_{i=1}^{q_\xi} w_i^\xi f(\xi_i,\eta_j) \left|\frac{\partial(x,y)}{\partial(\xi,\eta)}\right|$$

Similarly, when the boundary runs in a horizontal direction

$$x = \frac{x_a + x_b}{2} + \xi\,\frac{x_b - x_a}{2}$$
$$y = \frac{y_a(x) + y_b(x)}{2} + \eta\,\frac{y_b(x) - y_a(x)}{2}$$

$$\left|\frac{\partial(x,y)}{\partial(\xi,\eta)}\right| = \begin{vmatrix} \frac{\partial x}{\partial \xi} & \frac{\partial x}{\partial \eta} \\ \frac{\partial y}{\partial \xi} & \frac{\partial y}{\partial \eta} \end{vmatrix} = \begin{vmatrix} \frac{\partial x}{\partial \xi} & 0 \\ \frac{\partial y}{\partial \xi} & \frac{\partial y}{\partial \eta} \end{vmatrix}$$
$$= \frac{(x_b - x_a)\Big(y_b(x) - y_a(x)\Big)}{4}$$

$$\int_{x_a}^{x_b} \int_{y_a(x)}^{y_b(x)} f(x,y)\,\mathrm{d}y\,\mathrm{d}x \approx \sum_{i=1}^{q_\xi} w_i^\xi \sum_{j=1}^{q_\eta} w_j^\eta f(\xi_i,\eta_j) \left|\frac{\partial(x,y)}{\partial(\xi,\eta)}\right|$$

An example distribution of numerical integration points distributed according to this parameterization using a product nine-point Gauss-Legendre rule is shown in figure 4.1.

Polar coordinates parametrization When the boundary intersects our integration region so that either exactly one corner lies inside the domain or exactly three corners lie inside the domain, parameterization with polar coordinates will give a more accurate approximation to the integral. (Luft et al., 2008)

$$\begin{aligned} r &= \frac{r_a(\theta)+r_b(\theta)}{2} + \xi\,\frac{r_b(\theta)-r_a(\theta)}{2} \\ \theta &= \frac{\theta_a+\theta_b}{2} \qquad\quad + \eta\,\frac{\theta_b-\theta_a}{2} \end{aligned}$$

$$\begin{aligned} \left|\frac{\partial(r,\theta)}{\partial(\xi,\eta)}\right| &= \begin{vmatrix} \frac{\partial r}{\partial \xi} & \frac{\partial r}{\partial \eta} \\ \frac{\partial \theta}{\partial \xi} & \frac{\partial \theta}{\partial \eta} \end{vmatrix} = \begin{vmatrix} \frac{\partial r}{\partial \xi} & \frac{\partial r}{\partial \eta} \\ 0 & \frac{\partial \theta}{\partial \eta} \end{vmatrix} \\ &= \frac{\Big(r_b(\theta)-r_a(\theta)\Big)(\theta_b-\theta_a)}{4} \end{aligned}$$

$$\int_{\theta_a}^{\theta_b} \int_{r_a(\theta)}^{r_b(\theta)} f(r,\theta)\, r \, \mathrm{d}r \, \mathrm{d}\theta = \int_{\eta_a}^{\eta_b} \int_{\xi_a}^{\xi_b} f(\xi,\eta)\, r(\xi) \left| \frac{\partial(r,\theta)}{\partial(\xi,\eta)} \right| \, \mathrm{d}\xi \, \mathrm{d}\eta$$

$$\approx \sum_{j=1}^{q_\eta} w_j^\eta \sum_{i=1}^{q_\xi} w_i^\xi f(\xi_i,\eta_j)\, r(\xi_i) \left| \frac{\partial(r,\theta)}{\partial(\xi,\eta)} \right|$$

Example distributions of numerical integration points distributed according to this parameterization using a product nine-point Gauss-Legendre rule is shown in figure 4.1.

4.6 Numerical Integration on the Boundary

A naïve way of performing curve integrals is to use a parameterization unrelated to the parameterization used for the interior integral. Here we describe an efficient way of performing curve integrals that makes use of computations performed during the interior integral and approximates integrals in a way that is more likely to be numerically compatible with the interior integral.

The integral of a function $f : \mathbb{R}^n \to \mathbb{R}$ along a curve C is defined to be

$$\int_C f \, \mathrm{d}s = \int_{\tau_a}^{\tau_b} f(\underline{\boldsymbol{x}}(\tau)) \left| \underline{\boldsymbol{x}}'(\tau) \right| \, \mathrm{d}\tau$$

where $\underline{x} = (x, y)$ is some sufficiently smooth parameterization of C.

The equation of the line going through the points (x_1, y_1), (x_2, y_2) is

$$\underline{x} = (x_1, y_1) + \lambda(x_2 - x_1, y_2 - y_1)$$

For $x_2 - x_1 \neq 0$ and $y_2 - y_1 \neq 0$ we eliminate λ to get

$$\frac{x - x_1}{x_2 - x_1} = \frac{y - y_1}{y_2 - y_1}$$

which is suggestive of how we may arrive at equations for x and y.

For $x_2 - x_1 \neq 0$

$$\begin{aligned} x &= \frac{x_a + x_b}{2} + \tau\frac{x_b - x_a}{2} \\ y &= \frac{x - x_1}{x_2 - x_1}(y_2 - y_1) + y_1 \end{aligned}$$

so

$$\left|\underline{x}'(\tau)\right| = \frac{|x_b - x_a|}{2}\left(1 + \left(\frac{y_2 - y_1}{x_2 - x_1}\right)^2\right)^{\frac{1}{2}}$$

For $y_2 - y_1 \neq 0$

$$\begin{aligned} x &= \frac{y - y_1}{y_2 - y_1}(x_2 - x_1) + x_1 \\ y &= \frac{y_a + y_b}{2} + \tau\frac{y_b - y_a}{2} \end{aligned}$$

so

$$\left|\underline{x}'(\tau)\right| = \frac{|y_b - y_a|}{2}\left(1 + \left(\frac{x_2 - x_1}{y_2 - y_1}\right)^2\right)^{\frac{1}{2}}$$

Polar Coordinates Line Integral The equation of a line in polar coordinate form is

$$r(\theta) = \frac{r_0}{\cos(\theta - \theta_0)}$$

where (r_0, θ_0) is the foot of the perpendicular from the pole $(0, 0)$ to the line. We take the parameterization

$$\theta = \frac{\theta_a + \theta_b}{2} + \tau\frac{\theta_b - \theta_a}{2}$$
$$r = \frac{r_0}{\cos(\theta - \theta_0)}$$

and use $x = r\cos\theta$, $y = r\sin\theta$ to see that

$$\begin{aligned}
\frac{\partial x}{\partial \tau} &= \frac{\partial r}{\partial \theta}\frac{\partial \theta}{\partial \tau}(\cos\theta) - r(\sin\theta)\frac{\partial \theta}{\partial \tau} \\
\frac{\partial y}{\partial \tau} &= \frac{\partial r}{\partial \theta}\frac{\partial \theta}{\partial \tau}(\sin\theta) + r(\cos\theta)\frac{\partial \theta}{\partial \tau} \\
\frac{\partial r}{\partial \theta} &= r\tan(\theta - \theta_0)
\end{aligned}$$

Cancellation gives

$$\begin{aligned}
\left|\underline{x}'(\tau)\right| &= r\,\frac{|\theta_b - \theta_a|}{2}\left(1 + \tan^2(\theta - \theta_0)\right)^{\frac{1}{2}} \\
&= \frac{r\,|\theta_b - \theta_a|}{2\,|\cos(\theta - \theta_0)\,|}
\end{aligned}$$

Gauss-Legendre quadrature The Gauss-Legendre quadrature rules (one dimensional) are calculated by solving a sparse matrix with non-zero entries only on the diagonals above and below the main diagonal following Trefethen and Bau III (1997). The matrix is solved using the double precision LAPACK function `dstevd` which computes the eigenvalues and eigenvectors of tridiagonal matrices (all entries on our main diagonal are zero).

Point in polygon test The point in polygon test we use is the Hacker-Shimrat Algorithm 112 (Hacker, 1962).

Generalized Minimal Residual Method The Generalized Minimial Residual Method (GMRES) is a Krylov subspace method (Trefethen and Bau III, 1997, p. 245) for numerical solution of matrix equations with matrices that are possibly non-symmetric (Saad and Schultz, 1986; Trefethen and Bau III, 1997, p. 266). We use the multi-programming language (FORTRAN, C/C++) library PETSc which provides a parallel implementation of GMRES.

4.7 Stationary Convergence Test

A benefit of PUM is that it allows a step-wise implementation. Our first implementations were purely box-based and gave a crude approximation to the domain. In order to test our non-boundary resolving implementations, we used a test problem where the boundary conditions were automatically satisfied, or at least very well approximated. As is often seen in software development and biology, this test case has been retained indefinitely.

We look at the test problem (Babuška et al., 2002; Griebel and Schweitzer, 2002c; Eigel et al., 2009)

$$\begin{aligned} -\Delta u + u &= f \quad \text{on} \quad \Omega \\ \frac{\partial u}{\partial \boldsymbol{n}} &= 0 \quad \text{on} \quad \partial\Omega \end{aligned}$$

with $\Omega = [0,1] \times [0,1] \subset \mathbb{R}^2$ and we choose $f = 2x^3 - 3x^2 + 12x - 6$ so that the solution is $u(x,y) = 2x^3 - 3x^2$.

In the tables that follow, the relative L^2-error e_{L^2} and relative H^1 semi-norm error e_{H^1} calculated at a certain level of refinement l are

$$\begin{aligned} e_{L^2} &= \frac{\|u - u_l^h\|_2^l}{\|u\|_2^l} \\ e_{H^1} &= \frac{|u - u_l^h|_{H^1}^l}{|u|_{H^1}^l} \end{aligned}$$

where u denotes the true solution and u_l^h denotes the PUM approximation at level l. The L^2 error convergence rate ρ_{L^2} and H^1 semi-norm error convergence rate ρ_{H^1} are

$$\rho_{L^2} = \frac{\log \frac{\|u-u^h\|_2^l}{\|u-u_l^h\|_2^{l-1}}}{\log \frac{\text{dof}^l}{\text{dof}^{l-1}}}$$

$$\rho_{H^1} = \frac{\log \frac{|u-u^h|_{H^1}^l}{|u-u_l^h|_{H^1}^{l-1}}}{\log \frac{\text{dof}^l}{\text{dof}^{l-1}}}$$

All integrals are calculated numerically even though our simple test cases would allow exact calculation. This ensures greater generality and reproducibility of program execution. A consequence of this is that the relative errors and convergence rates shown are not the best values that could be calculated. It would also have been possible to employ the highest level of detail in a single program execution in order to increase the accuracy of the lower detail level calculations. We sacrifice this higher level of accuracy to ensure independence of different but related calculations.

4.7.1 Convergence Needs High Order Quadrature

Significance to mixed-sized patches The convergence behaviour of PUM has been used in the past to demonstration correctness of implementation and conformance to theory but there have been few remarks on the impor-

tance of the integration scheme to the convergence behaviour and accuracy. This is of particular relevance to the case where mixed-sized patches are allowed and the order of the numerical integration scheme must be increased in regions with a high density of patches.

Our PUM implementation calculates the relative L^2 error, relative H^1 semi-norm error and corresponding convergence rates between two given levels of refinement. For levels of refinement l ranging from one to eight, a single MPI process with four OpenMP threads is used on the IBM Cluster. One solve is carried out per level of refinement for a total of eight solves. In the tables that follow $\boldsymbol{\alpha_c}$ is the cover factor, $\boldsymbol{q}$ is the one dimensional Gauss-Legendre quadrature order used for numerical integration, $\boldsymbol{l}$ is the level of refinement and **dof** is the number of degrees of freedom solved for.

We consider first the lowest local basis order of $p = 1$. In table 4.2 we see that the rate of convergence at high levels of refinement is limited when using low quadrature orders and table 4.3 shows that close to optimal rates are attainable for high quadrature orders. When we increase the local basis order to $p = 2$ we see an approximate doubling in walltime as the costs are dominated by the assembly at problem sizes of these refinement levels as compared to $p = 1$. Convergence is seen to be severely limited especially for the H^1 semi-norm error in table 4.4. There is an improvement with medium quadrature orders in table 4.5 although the walltime reaches the edge of what is reasonable for such a simple run. When we reach high quadrature orders in table 4.6, we see respectable convergence rates but the

walltime cost has become too high for assembly with only four OpenMP threads.

4.7.2 High Order Quadrature and Changing Cover Factor

We continue now with local basis order $p = 1$. In light of the convergence tests shown, we have selected quadrature order $q = 9$ as a high quadrature order that is a suitable compromise between computational expense and sufficient accuracy. It should be noted that selecting a slightly sub-optimal quadrature order is seen to reduce the rate of convergence but does not immediately result in incorrect solutions in the test case considered. We see good robustness for the range of cover factors tested in tables 4.7, 4.8 and 4.9.

4.7.3 Extremes of Cover Factor

With structured positioning of patches we see reasonable behaviour with large cover factors. As the refinement level increases to the point where the numerical integration order limits the accuracy, we have seen the error no longer decreases but remain steady in a certain restricted range of values. In contrast, small cover factors present a significant problem when combined with an inadequate quadrature order and PUM may return a

Figure 4.1: Numerical integration in the interior. A product rule based on the nine-point Gauss-Legendre rule (giving 49 numerical integration points) is used as the base rule for numerical integration. The numerical integration scheme presented does not require decomposition to triangular or quadrilateral pieces, and the number of integration points does not, in general, increase with the number of boundary points. Four test cases are shown with one example of the Cartesian coordinate parameterization used (top left), and three examples (top right and bottom row) of the more implementationally compilicated polar coordinates parameterization. The grey box encloses a part of the domain being processed. The boundary of the domain is shown in black, the blue points are numerical integration points that lie within the domain and the red points are numerical integration points that lie outside the domain.

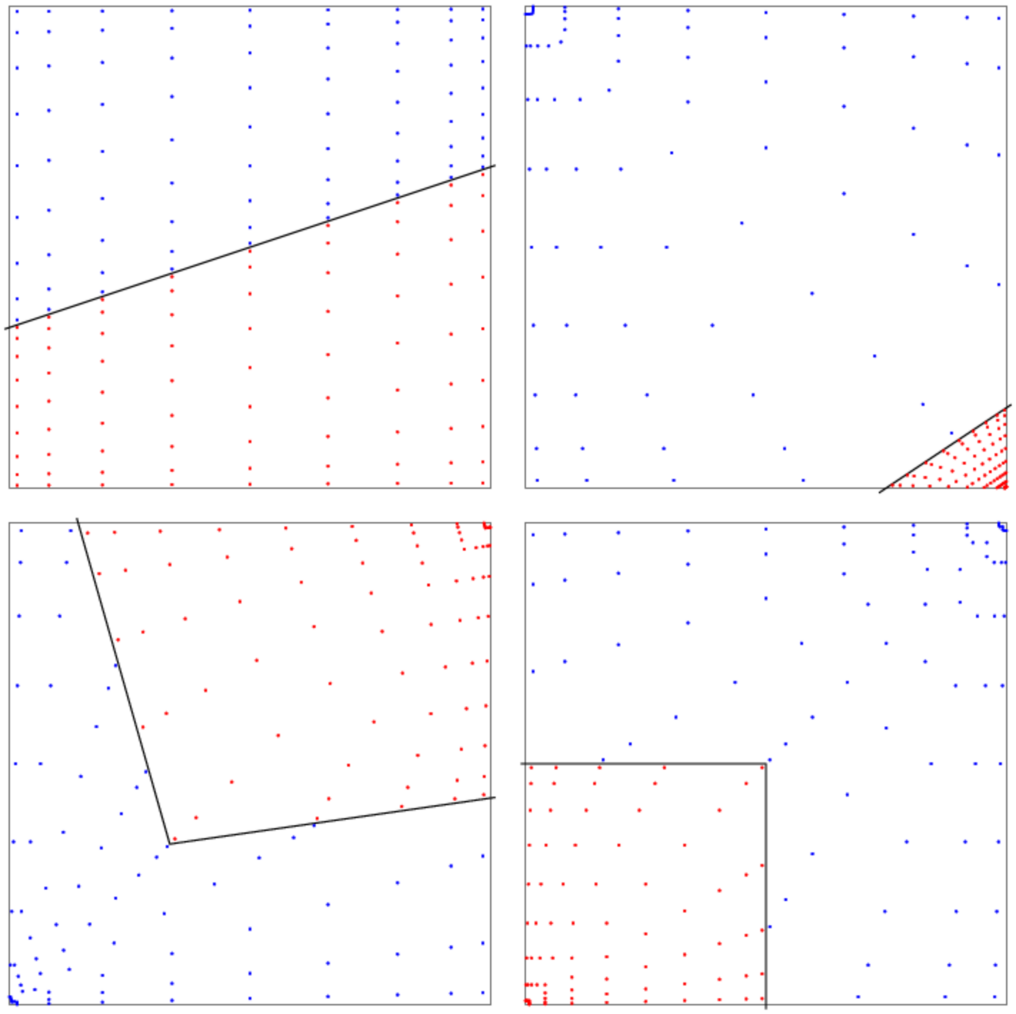

Table 4.2: Convergence: low quadrature orders q and $p = 1$. Low quadrature orders eventually limit the accuracy that may be attained. The convergence runs took 242.67 s, 323.70 s, 383.89 s and 462.24 s respectively.

α_c	q	p	l	**dof**	e_{L^2}	e_{H^1}	ρ_{L^2}	ρ_{H^1}
1.3	5	1	1	12	6.936_{-2}	4.418_{-1}		
			2	48	1.819_{-2}	2.239_{-1}	−0.982	−0.489
			3	192	4.450_{-3}	1.115_{-1}	−1.020	−0.503
			4	768	1.056_{-3}	5.841_{-2}	−1.039	−0.466
			5	3072	2.555_{-4}	3.501_{-2}	−1.024	−0.369
			6	12288	2.051_{-4}	2.617_{-2}	−0.159	−0.210
			7	49152	2.402_{-4}	2.345_{-2}	+0.114	−0.079
			8	193548	2.574_{-4}	2.270_{-2}	+0.051	−0.024
1.3	6	1	1	12	1.046_{-1}	3.754_{-1}		
			2	48	3.243_{-2}	2.201_{-1}	−0.838	−0.386
			3	192	8.644_{-3}	1.162_{-1}	−0.952	−0.461
			4	768	2.159_{-3}	5.993_{-2}	−1.001	−0.478
			5	3072	4.979_{-4}	3.168_{-2}	−1.058	−0.460
			6	12288	8.887_{-5}	1.855_{-2}	−1.243	−0.386
			7	49152	3.963_{-5}	1.330_{-2}	−0.583	−0.240
			8	193548	5.499_{-5}	1.158_{-2}	+0.239	−0.101
1.3	7	1	1	12	7.719_{-2}	4.166_{-1}		
			2	48	2.222_{-2}	2.227_{-1}	−0.908	−0.451
			3	192	5.765_{-3}	1.126_{-1}	−0.975	−0.492
			4	768	1.486_{-3}	5.650_{-2}	−0.978	−0.497
			5	3072	3.886_{-4}	2.851_{-2}	−0.968	−0.493
			6	12288	1.019_{-4}	1.469_{-2}	−0.966	−0.478
			7	49152	2.410_{-5}	8.086_{-3}	−1.040	−0.431
			8	193548	4.633_{-6}	5.191_{-3}	−1.203	−0.323
1.3	8	1	1	12	1.020_{-1}	3.797_{-1}		
			2	48	3.080_{-2}	2.184_{-1}	−0.860	−0.399
			3	192	8.129_{-3}	1.138_{-1}	−0.960	−0.471
			4	768	2.059_{-3}	5.765_{-2}	−0.990	−0.490
			5	3072	5.137_{-4}	2.904_{-2}	−1.002	−0.495
			6	12288	1.266_{-4}	1.468_{-2}	−1.011	−0.492
			7	49152	3.050_{-5}	7.520_{-3}	−1.026	−0.482
			8	193548	7.237_{-6}	3.993_{-3}	−1.050	−0.462

Table 4.3: Convergence: high quadrature orders q and $p = 1$. Here we see good agreement in the measured convergence rates and the orders of magnitude of the relative errors. The convergence runs took 620.90 s, 623.81 s, 754.61 s and 895.97 s respectively.

α_c	q	p	l	**dof**	e_{L^2}	e_{H^1}	ρ_{L^2}	ρ_{H^1}
1.3	9	1	1	12	8.254_{-2}	4.055_{-1}		
			2	48	2.439_{-2}	2.219_{-1}	−0.885	−0.435
			3	192	6.399_{-3}	1.134_{-1}	−0.967	−0.484
			4	768	1.648_{-3}	5.706_{-2}	−0.979	−0.495
			5	3072	4.287_{-4}	2.866_{-2}	−0.972	−0.497
			6	12288	1.136_{-4}	1.443_{-2}	−0.958	−0.495
			7	49152	3.029_{-5}	7.296_{-3}	−0.954	−0.492
			8	193548	7.065_{-6}	3.695_{-3}	−1.062	−0.496
1.3	10	1	1	12	9.977_{-2}	3.822_{-1}		
			2	48	2.991_{-2}	2.183_{-1}	−0.867	−0.404
			3	192	7.866_{-3}	1.133_{-1}	−0.963	−0.473
			4	768	1.994_{-3}	5.729_{-2}	−0.990	−0.492
			5	3072	4.999_{-4}	2.881_{-2}	−0.998	−0.496
			6	12288	1.248_{-4}	1.450_{-2}	−1.001	−0.495
			7	49152	3.108_{-5}	7.321_{-3}	−1.003	−0.493
			8	193548	7.988_{-6}	3.682_{-3}	−0.991	−0.501
1.3	11	1	1	12	8.598_{-2}	3.999_{-1}		
			2	48	2.558_{-2}	2.212_{-1}	−0.878	−0.427
			3	192	6.727_{-3}	1.135_{-1}	−0.965	−0.481
			4	768	1.727_{-3}	5.721_{-2}	−0.981	−0.494
			5	3072	4.455_{-4}	2.875_{-2}	−0.978	−0.496
			6	12288	1.165_{-4}	1.446_{-2}	−0.967	−0.495
			7	49152	3.065_{-5}	7.300_{-3}	−0.963	−0.493
			8	193548	7.385_{-6}	3.668_{-3}	−1.038	−0.502
1.3	12	1	1	12	9.831_{-2}	3.837_{-1}		
			2	48	2.941_{-2}	2.185_{-1}	−0.869	−0.406
			3	192	7.731_{-3}	1.132_{-1}	−0.963	−0.474
			4	768	1.961_{-3}	5.722_{-2}	−0.989	−0.492
			5	3072	4.931_{-4}	2.877_{-2}	−0.996	−0.496
			6	12288	1.237_{-4}	1.448_{-2}	−0.997	−0.495
			7	49152	3.100_{-5}	7.308_{-3}	−0.998	−0.493
			8	193548	7.915_{-6}	3.671_{-3}	−0.996	−0.502

Table 4.4: Convergence: low quadrature orders q and $p = 2$. Low quadrature orders eventually limit the accuracy that may be attained. The convergence runs took 683.17 s, 825.07 s, 994.12 s and 1202.59 s respectively.

α_c	q	p	l	**dof**	e_{L^2}	e_{H^1}	ρ_{L^2}	ρ_{H^1}
1.3	5	2	1	24	6.289_{-2}	1.651_{-1}		
			2	96	1.627_{-2}	5.004_{-2}	−0.992	−0.860
			3	384	4.050_{-3}	2.548_{-2}	−1.007	−0.487
			4	1536	1.120_{-3}	2.267_{-2}	−0.928	−0.084
			5	6144	4.406_{-4}	2.246_{-2}	−0.673	−0.007
			6	24576	2.913_{-4}	2.244_{-2}	−0.298	−0.001
			7	98304	2.642_{-4}	2.244_{-2}	−0.071	−0.000
			8	387096	2.636_{-4}	2.244_{-2}	−0.002	−0.000
1.3	6	2	1	24	2.623_{-2}	9.658_{-2}		
			2	96	5.783_{-3}	2.590_{-2}	−1.084	−0.950
			3	384	1.330_{-3}	1.240_{-2}	−1.059	−0.531
			4	1536	2.874_{-4}	1.104_{-2}	−1.105	−0.084
			5	6144	7.396_{-5}	1.094_{-2}	−0.979	−0.006
			6	24576	6.379_{-5}	1.094_{-2}	−0.107	−0.000
			7	98304	6.403_{-5}	1.094_{-2}	+0.003	−0.000
			8	387096	6.207_{-5}	1.094_{-2}	−0.023	−0.000
1.3	7	2	1	24	3.356_{-2}	1.171_{-1}		
			2	96	8.601_{-3}	2.975_{-2}	−0.991	−0.988
			3	384	2.051_{-3}	8.392_{-3}	−1.036	−0.913
			4	1536	4.686_{-4}	4.176_{-3}	−1.065	−0.503
			5	6144	1.014_{-4}	3.764_{-3}	−1.104	−0.075
			6	24576	2.318_{-5}	3.740_{-3}	−1.065	−0.005
			7	98304	9.396_{-6}	3.738_{-3}	−0.651	−0.000
			8	387096	8.632_{-6}	3.738_{-3}	−0.062	−0.000
1.3	8	2	1	24	1.887_{-2}	8.744_{-2}		
			2	96	3.620_{-3}	2.058_{-2}	−1.187	−1.044
			3	384	8.054_{-4}	5.175_{-3}	−1.083	−0.996
			4	1536	1.795_{-4}	1.922_{-3}	−1.083	−0.715
			5	6144	3.624_{-5}	1.523_{-3}	−1.154	−0.168
			6	24576	6.285_{-6}	1.497_{-3}	−1.264	−0.013
			7	98304	2.433_{-6}	1.495_{-3}	−0.685	−0.001
			8	387096	1.330_{-6}	1.495_{-3}	−0.441	−0.000

Table 4.5: Convergence: medium quadrature orders q and $p = 2$. Here we see relatively good agreement in the measured convergence rates and the orders of magnitude of the relative errors.

α_c	q	p	l	**dof**	e_{L^2}	e_{H^1}	ρ_{L^2}	ρ_{H^1}
1.3	9	2	1	24	2.135_{-2}	9.951_{-2}		
			2	96	5.377_{-3}	2.376_{-2}	−1.001	−1.033
			3	384	1.279_{-3}	5.876_{-3}	−1.037	−1.008
			4	1536	2.887_{-4}	1.531_{-3}	−1.074	−0.970
			5	6144	5.821_{-5}	6.387_{-4}	−1.155	−0.631
			6	24576	8.888_{-6}	5.480_{-4}	−1.356	−0.110
			7	98304	9.203_{-7}	5.432_{-4}	−1.636	−0.006
			8	387096	9.346_{-7}	5.430_{-4}	+0.011	−0.000
1.3	10	2	1	24	1.550_{-2}	8.461_{-2}		
			2	96	2.600_{-3}	1.950_{-2}	−1.286	−1.059
			3	384	5.437_{-4}	4.652_{-3}	−1.128	−1.034
			4	1536	1.190_{-4}	1.147_{-3}	−1.096	−1.010
			5	6144	2.379_{-5}	3.416_{-4}	−1.161	−0.874
			6	24576	3.580_{-6}	2.134_{-4}	−1.366	−0.339
			7	98304	3.520_{-7}	2.033_{-4}	−1.673	−0.035
			8	387096	3.770_{-7}	2.028_{-4}	+0.050	−0.002
1.3	11	2	1	24	1.556_{-2}	9.197_{-2}		
			2	96	3.718_{-3}	2.129_{-2}	−1.037	−1.055
			3	384	8.781_{-4}	5.135_{-3}	−1.042	−1.026
			4	1536	1.979_{-4}	1.252_{-3}	−1.075	−1.018
			5	6144	3.978_{-5}	3.080_{-4}	−1.157	−1.012
			6	24576	5.915_{-6}	1.013_{-4}	−1.375	−0.803
			7	98304	2.544_{-7}	7.547_{-5}	−2.270	−0.212
			8	387096	4.749_{-7}	7.389_{-5}	+0.455	−0.015
1.3	12	2	1	24	1.376_{-2}	8.351_{-2}		
			2	96	2.060_{-3}	1.907_{-2}	−1.368	−1.065
			3	384	3.998_{-4}	4.517_{-3}	−1.182	−1.039
			4	1536	8.526_{-5}	1.096_{-3}	−1.115	−1.022
			5	6144	1.691_{-5}	2.700_{-4}	−1.167	−1.011
			6	24576	2.510_{-6}	7.132_{-5}	−1.376	−0.960
			7	98304	6.583_{-8}	3.160_{-5}	−2.626	−0.587
			8	387096	2.599_{-7}	2.783_{-5}	+1.002	−0.093

Table 4.6: Convergence: high quadrature orders q and $p = 2$. Here we see good agreement in the measured convergence rates and the orders of magnitude of the relative errors. The convergence runs took 2589.02 s, 2850.15 s, 3215.18 s and 3733.45 s respectively.

α_c	q	p	l	**dof**	e_{L^2}	e_{H^1}	ρ_{L^2}	ρ_{H^1}
1.3	13	2	1	24	1.270_{-2}	8.836_{-2}		
			2	96	2.771_{-3}	2.013_{-2}	−1.101	−1.067
			3	384	6.426_{-4}	4.798_{-3}	−1.055	−1.035
			4	1536	1.443_{-4}	1.165_{-3}	−1.078	−1.021
			5	6144	2.897_{-5}	2.823_{-4}	−1.158	−1.022
			6	24576	4.309_{-6}	6.829_{-5}	−1.375	−1.024
			7	98304	9.470_{-8}	1.902_{-5}	−2.754	−0.922
			8	387096	3.076_{-7}	1.265_{-5}	+0.860	−0.298
1.3	14	2	1	24	1.277_{-2}	8.304_{-2}		
			2	96	1.752_{-3}	1.887_{-2}	−1.432	−1.069
			3	384	3.136_{-4}	4.456_{-3}	−1.241	−1.041
			4	1536	6.463_{-5}	1.080_{-3}	−1.139	−1.022
			5	6144	1.269_{-5}	2.656_{-4}	−1.174	−1.012
			6	24576	1.878_{-6}	6.587_{-5}	−1.378	−1.006
			7	98304	1.350_{-7}	1.631_{-5}	−1.899	−1.007
			8	387096	9.703_{-8}	4.928_{-6}	−0.241	−0.873
1.3	15	2	1	24	1.129_{-2}	8.645_{-2}		
			2	96	2.197_{-3}	1.955_{-2}	−1.183	−1.072
			3	384	4.935_{-4}	4.627_{-3}	−1.078	−1.039
			4	1536	1.100_{-4}	1.122_{-3}	−1.083	−1.022
			5	6144	2.205_{-5}	2.737_{-4}	−1.159	−1.018
			6	24576	3.280_{-6}	6.675_{-5}	−1.375	−1.018
			7	98304	1.446_{-7}	1.703_{-5}	−2.251	−0.985
			8	387096	1.784_{-7}	5.892_{-6}	+0.153	−0.774
1.3	16	2	1	24	1.217_{-2}	8.284_{-2}		
			2	96	1.566_{-3}	1.877_{-2}	−1.478	−1.071
			3	384	2.590_{-4}	4.424_{-3}	−1.298	−1.043
			4	1536	5.119_{-5}	1.072_{-3}	−1.169	−1.023
			5	6144	9.911_{-6}	2.640_{-4}	−1.184	−1.011
			6	24576	1.463_{-6}	6.569_{-5}	−1.380	−1.003
			7	98304	1.441_{-7}	1.696_{-5}	−1.672	−0.977
			8	387096	8.900_{-8}	6.226_{-6}	−0.352	−0.731

Table 4.7: Convergence: small cover factors α_c and quadrature order $q = 9$.

α_c	q	**Level**	**dof**	e_{L^2}	$e_{W^{1,2}}$	ρ_{L^2}	$\rho_{W^{1,2}}$
1.1	9	1	12	8.848_{-2}	4.269_{-1}		
		2	48	2.388_{-2}	2.247_{-1}	−0.952	−0.463
		3	192	6.068_{-3}	1.131_{-1}	−0.990	−0.495
		4	768	1.551_{-3}	5.663_{-2}	−0.984	−0.499
		5	3072	4.088_{-4}	2.839_{-2}	−0.962	−0.498
		6	12288	1.327_{-4}	1.428_{-2}	−0.811	−0.496
		7	49152	4.505_{-5}	7.214_{-3}	−0.779	−0.493
		8	193548	5.263_{-6}	3.630_{-3}	−1.567	−0.501
1.2	9	1	12	8.551_{-2}	4.176_{-1}		
		2	48	2.417_{-2}	2.237_{-1}	−0.918	−0.450
		3	192	6.244_{-3}	1.134_{-1}	−0.978	−0.490
		4	768	1.602_{-3}	5.691_{-2}	−0.982	−0.497
		5	3072	4.173_{-4}	2.856_{-2}	−0.971	−0.497
		6	12288	1.112_{-4}	1.437_{-2}	−0.954	−0.495
		7	49152	2.990_{-5}	7.262_{-3}	−0.947	−0.492
		8	193548	6.925_{-6}	3.666_{-3}	−1.067	−0.499
1.3	9	1	12	8.254_{-2}	4.081_{-1}		
		2	48	2.439_{-2}	2.223_{-1}	−0.885	−0.438
		3	192	6.399_{-3}	1.134_{-1}	−0.967	−0.485
		4	768	1.648_{-3}	5.707_{-2}	−0.979	−0.495
		5	3072	4.287_{-4}	2.866_{-2}	−0.972	−0.497
		6	12288	1.136_{-4}	1.443_{-2}	−0.958	−0.495
		7	49152	3.029_{-5}	7.296_{-3}	−0.954	−0.492
		8	193548	7.062_{-6}	3.695_{-3}	−1.062	−0.496
$1.\dot{3}$	9	1	12	8.154_{-2}	4.049_{-1}		
		2	48	2.444_{-2}	2.218_{-1}	−0.875	−0.434
		3	192	6.445_{-3}	1.134_{-1}	−0.963	−0.484
		4	768	1.662_{-3}	5.710_{-2}	−0.978	−0.495
		5	3072	4.322_{-4}	2.868_{-2}	−0.972	−0.497
		6	12288	1.144_{-4}	1.444_{-2}	−0.959	−0.495
		7	49152	3.040_{-5}	7.303_{-3}	−0.956	−0.492
		8	193548	7.094_{-6}	3.703_{-3}	−1.062	−0.495

Table 4.8: Convergence: medium cover factors α_c and quadrature order $q = 9$.

α_c	q	**Level**	**dof**	e_{L^2}	$e_{W^{1,2}}$	ρ_{L^2}	$\rho_{W^{1,2}}$
1.4	9	1	12	7.955_{-2}	3.984_{-1}		
		2	48	2.452_{-2}	2.207_{-1}	−0.854	−0.426
		3	192	6.530_{-3}	1.133_{-1}	−0.956	−0.481
		4	768	1.688_{-3}	5.713_{-2}	−0.976	−0.494
		5	3072	4.384_{-4}	2.871_{-2}	−0.972	−0.496
		6	12288	1.157_{-4}	1.445_{-2}	−0.961	−0.495
		7	49152	3.056_{-5}	7.313_{-3}	−0.960	−0.491
		8	193548	7.157_{-6}	3.718_{-3}	−1.059	−0.494
1.5	9	1	12	7.655_{-2}	3.884_{-1}		
		2	48	2.458_{-2}	2.188_{-1}	−0.824	−0.414
		3	192	6.635_{-3}	1.130_{-1}	−0.946	−0.477
		4	768	1.720_{-3}	5.707_{-2}	−0.974	−0.493
		5	3072	4.461_{-4}	2.869_{-2}	−0.973	−0.496
		6	12288	1.172_{-4}	1.445_{-2}	−0.964	−0.495
		7	49152	3.071_{-5}	7.312_{-3}	−0.966	−0.491
		8	193548	7.247_{-6}	3.728_{-3}	−1.054	−0.492
1.6	9	1	12	7.358_{-2}	3.782_{-1}		
		2	48	2.456_{-2}	2.166_{-1}	−0.796	−0.402
		3	192	6.719_{-3}	1.125_{-1}	−0.936	−0.472
		4	768	1.746_{-3}	5.692_{-2}	−0.972	−0.492
		5	3072	4.521_{-4}	2.863_{-2}	−0.975	−0.496
		6	12288	1.181_{-4}	1.443_{-2}	−0.968	−0.494
		7	49152	3.052_{-5}	7.339_{-3}	−0.976	−0.488
		8	193548	7.072_{-6}	3.813_{-3}	−1.067	−0.478

Table 4.9: Convergence: large cover factors α_c and quadrature order $q = 9$.

α_c	q	**Level**	**dof**	e_{L^2}	$e_{W^{1,2}}$	ρ_{L^2}	$\rho_{W^{1,2}}$
1.7	9	1	12	7.042_{-2}	3.678_{-1}		
		2	48	2.436_{-2}	2.139_{-1}	−0.769	−0.391
		3	192	6.746_{-3}	1.117_{-1}	−0.927	−0.468
		4	768	1.757_{-3}	5.658_{-2}	−0.971	−0.491
		5	3072	4.544_{-4}	2.844_{-2}	−0.976	−0.496
		6	12288	1.185_{-4}	1.431_{-2}	−0.969	−0.496
		7	49152	3.072_{-5}	7.224_{-3}	−0.974	−0.493
		8	193548	7.462_{-6}	3.660_{-3}	−1.032	−0.496
1.8	9	1	12	6.718_{-2}	3.571_{-1}		
		2	48	2.400_{-2}	2.107_{-1}	−0.746	−0.381
		3	192	6.720_{-3}	1.106_{-1}	−0.919	−0.465
		4	768	1.752_{-3}	5.604_{-2}	−0.970	−0.490
		5	3072	4.524_{-4}	2.817_{-2}	−0.977	−0.496
		6	12288	1.176_{-4}	1.416_{-2}	−0.972	−0.496
		7	49152	2.682_{-5}	7.138_{-3}	−1.066	−0.494
		8	193548	7.465_{-6}	3.609_{-3}	−0.933	−0.498
1.9	9	1	12	6.429_{-2}	3.460_{-1}		
		2	48	2.366_{-2}	2.070_{-1}	−0.724	−0.371
		3	192	6.700_{-3}	1.093_{-1}	−0.911	−0.461
		4	768	1.749_{-3}	5.540_{-2}	−0.969	−0.490
		5	3072	4.501_{-4}	2.784_{-2}	−0.979	−0.496
		6	12288	1.162_{-4}	1.402_{-2}	−0.977	−0.495
		7	49152	2.561_{-5}	7.127_{-3}	−1.091	−0.488
		8	193548	6.997_{-6}	3.729_{-3}	−0.947	−0.473

wholly unacceptable solution (table 4.10). This has implications for when patches are allowed to be of different sizes and may be arbitrarily positioned because the quadrature requirements vary dramatically in different parts of the discretization. Adaptive quadrature has been employed to avoid this issue but it is unclear what the implications of this are in terms of computational cost and it difficult to predict exactly what calculations will be carried out during the course of the computation. It seems the structured refinement and fixed quadrature approach may still be justified in order to find a local criteria for determining when the quadrature order needs to be increased to give optimal convergence in the global error.

4.7.4 Large Refinement Values

For nine levels of complete refinement it is no longer convenient to assemble and solve on a single workstation and parallel execution is necessary to keep the walltime below one hour. The assembly time, memory requirements and solve time become significant at ten levels of complete refinement when the number of degrees of freedom rises to above three million. Sample runs are provided in table 4.12. Refinement levels of this range and higher are beyond what is required to capture the detail that we have in our biological data and one would be interested in higher levels of refinement primarily for benchmarking supercomputers, testing highly optimized parallel solvers and testing the limits of PUM.

Table 4.10: Convergence: small cover factors are more problematic. We see the occasional incorrect solution produced: visual inspection of the solution shows no resemblance to the desired solution (the corresponding relative errors shown in bold).

c.f.	q.o.	Level	dof	e_{L^2}	$e_{W^{1,2}}$	ρ_{L^2}	$\rho_{W^{1,2}}$
1.1	4	1	12	1.239_{-1}	3.954_{-1}		
		2	48	3.690_{-2}	2.261_{-1}	−0.858	−0.405
		3	192	9.001_{-3}	1.242_{-1}	−1.014	−0.432
		4	768	1.552_{-3}	7.483_{-2}	−1.267	−0.366
		5	3072	6.489_{-4}	5.531_{-2}	−0.629	−0.218
		6	12288	1.016_{-3}	4.913_{-2}	+0.324	−0.085
		7	49152	1.112_{-3}	4.744_{-2}	+0.065	−0.025
		8	193548	1.131_{-3}	4.700_{-2}	+0.012	−0.007
1.1	5	1	12	7.017_{-2}	4.684_{-1}		
		2	48	1.671_{-2}	2.307_{-1}	−1.056	−0.509
		3	192	4.080_{-3}	1.131_{-1}	−1.022	−0.514
		4	768	1.222_{-3}	5.703_{-2}	−0.871	−0.494
		5	3072	$\mathbf{1.001_{+0}}$	$\mathbf{1.141_{+0}}$	+4.838	+2.161
		6	12288	$\mathbf{1.000_{+0}}$	$\mathbf{1.144_{+0}}$	−0.001	+0.002
		7	49152	$\mathbf{1.000_{+0}}$	$\mathbf{1.144_{+0}}$	−0.000	+0.000
		8	193548	$\mathbf{1.000_{+0}}$	$\mathbf{1.144_{+0}}$	−0.000	+0.000
1.1	6	1	12	1.176_{-1}	3.942_{-1}		
		2	48	3.383_{-2}	2.199_{-1}	−0.891	−0.422
		3	192	8.751_{-3}	1.135_{-1}	−0.974	−0.477
		4	768	2.179_{-3}	5.753_{-2}	−1.002	−0.490
		5	3072	5.244_{-4}	2.937_{-2}	−1.027	−0.485
		6	12288	1.150_{-4}	1.565_{-2}	−1.094	−0.454
		7	49152	1.771_{-5}	9.423_{-3}	−1.349	−0.366
		8	193548	1.166_{-5}	6.989_{-3}	−0.305	−0.218
1.1	7	1	12	8.148_{-2}	4.396_{-1}		
		2	48	2.130_{-2}	2.265_{-1}	−0.979	−0.478
		3	192	5.364_{-3}	1.130_{-1}	−0.998	−0.501
		4	768	1.381_{-3}	5.646_{-2}	−0.980	−0.501
		5	3072	3.705_{-4}	2.833_{-2}	−0.949	−0.497
		6	12288	8.640_{-3}	2.761_{-2}	+2.272	−0.019
		7	49152	2.104_{-4}	7.464_{-3}	−2.680	−0.943
		8	193548	$\mathbf{1.001_{+0}}$	$\mathbf{1.151_{+0}}$	+6.178	+3.676

Table 4.11: Convergence: large cover factors are less problematic.

c.f.	q.o.	Level	dof	e_{L^2}	$e_{W^{1,2}}$	ρ_{L^2}	$\rho_{W^{1,2}}$
1.9	4	1	12	8.344_{-2}	3.440_{-1}		
		2	48	4.191_{-2}	3.024_{-1}	−0.492	−0.093
		3	192	3.094_{-2}	2.631_{-1}	−0.218	−0.100
		4	768	2.959_{-2}	2.456_{-1}	−0.032	−0.050
		5	3072	2.946_{-2}	2.401_{-1}	−0.003	−0.016
		6	12288	2.944_{-2}	2.386_{-1}	−0.000	−0.004
		7	49152	2.942_{-2}	2.382_{-1}	−0.000	−0.001
		8	193548	2.943_{-2}	2.381_{-1}	+0.000	−0.000
1.9	5	1	12	6.898_{-2}	3.704_{-1}		
		2	48	2.153_{-2}	2.038_{-1}	−0.847	−0.431
		3	192	5.072_{-3}	1.111_{-1}	−1.044	−0.438
		4	768	1.466_{-3}	7.244_{-2}	−0.896	−0.308
		5	3072	1.411_{-3}	5.979_{-2}	−0.028	−0.138
		6	12288	1.523_{-3}	5.633_{-2}	+0.055	−0.043
		7	49152	1.577_{-3}	5.545_{-2}	+0.025	−0.011
		8	193548	1.575_{-3}	5.522_{-2}	−0.001	−0.003
1.9	6	1	12	6.476_{-2}	3.231_{-1}		
		2	48	2.516_{-2}	2.128_{-1}	−0.680	−0.301
		3	192	7.242_{-3}	1.213_{-1}	−0.898	−0.405
		4	768	1.659_{-3}	6.935_{-2}	−1.063	−0.404
		5	3072	4.347_{-4}	4.583_{-2}	−0.966	−0.299
		6	12288	5.203_{-4}	3.742_{-2}	+0.130	−0.146
		7	49152	5.758_{-4}	3.495_{-2}	+0.073	−0.049
		8	193548	5.968_{-4}	3.430_{-2}	+0.026	−0.014
1.9	7	1	12	6.447_{-2}	3.534_{-1}		
		2	48	2.293_{-2}	2.053_{-1}	−0.750	−0.392
		3	192	6.313_{-3}	1.069_{-1}	−0.931	−0.471
		4	768	1.603_{-3}	5.453_{-2}	−0.989	−0.486
		5	3072	3.852_{-4}	2.887_{-2}	−1.029	−0.459
		6	12288	8.143_{-5}	1.729_{-2}	−1.121	−0.370
		7	49152	5.290_{-5}	1.284_{-2}	−0.311	−0.215
		8	193548	5.734_{-5}	1.145_{-2}	+0.059	−0.084

Table 4.12: Convergence: large refinement level l and $p = 1$. With 64 MPI processes and 4 OpenMP threads per MPI process, the convergence runs took 1788.94 s, 1788.94 s, 1899.89 s, 3124.58 s, 3116.97 s, 2043.34 s and 3136.14 s respectively. With large matrices to solve in parallel, the walltime cost is dominated by the solve which is in line with FEM discretizations.

α_c	q	p	l	**dof**	e_{L^2}	e_{H^1}	ρ_{L^2}	ρ_{H^1}
1.3	9	1	7	49152	3.132_{-5}	7.296_{-3}		
			8	193548	1.919_{-5}	3.695_{-3}	−0.357	−0.496
			9	774192	9.079_{-6}	1.910_{-3}	−0.540	−0.476
			10	3084588	4.240_{-5}	1.066_{-3}	+1.115	−0.421
1.3	10	1	7	49152	4.179_{-5}	7.321_{-3}		
			8	193548	8.105_{-6}	3.682_{-3}	−1.197	−0.501
			9	774192	1.373_{-5}	1.853_{-3}	+0.380	−0.495
			10	3084588	1.111_{-6}	9.437_{-4}	−1.819	−0.488
1.3	11	1	7	49152	4.128_{-5}	7.300_{-3}		
			8	193548	1.096_{-5}	3.668_{-3}	−0.968	−0.502
			9	774192	4.215_{-6}	1.838_{-3}	−0.689	−0.498
			10	3084588	2.257_{-5}	9.233_{-4}	+1.214	−0.498
1.3	12	1	7	49152	3.120_{-5}	7.308_{-3}		
			8	193548	2.293_{-5}	3.671_{-3}	−0.225	−0.502
			9	774192	1.107_{-5}	1.839_{-3}	−0.525	−0.499
			10	3084588	4.789_{-4}	9.391_{-4}	+2.725	−0.486
1.3	13	1	7	49152	3.634_{-5}	7.304_{-3}		
			8	193548	2.121_{-5}	3.669_{-3}	−0.393	−0.502
			9	774192	1.372_{-5}	1.838_{-3}	−0.314	−0.499
			10	3084588	3.957_{-4}	9.266_{-4}	+2.432	−0.496
1.3	14	1	7	49152	3.456_{-5}	7.306_{-3}		
			8	193548	9.247_{-6}	3.670_{-3}	−0.962	−0.502
			9	774192	4.030_{-5}	1.838_{-3}	+1.062	−0.499
			10	3084588	6.677_{-5}	9.200_{-4}	+0.365	−0.501
1.3	15	1	7	49152	3.251_{-5}	7.305_{-3}		
			8	193548	2.326_{-5}	3.670_{-3}	−0.244	−0.502
			9	774192	2.682_{-6}	1.838_{-3}	−1.558	−0.499
			10	3084588	4.810_{-5}	9.220_{-4}	+2.088	−0.499

Chapter 5

Partition of Unity Method Modelling and Simulation

This modelling and simulation chapter seeks to analyze the previously described experimental data and determine if we can account for and explain the observed data. A number of different mathematical models are used in an attempt to capture and describe what is happening in the fluorescence microscopy experiments. In all cases, an equation or a number of equations are written down and are studied separately from the biology which remains in the background: it is only necessary to return to considering the real biological situation if the equations fail to capture something that is considered important.

The fluorescent protein of interest is assumed to diffuse in the chloroplast, moving from areas of high concentration to areas of low concentration, according to an expression that can be written down (the diffusion term). The photobleaching and binding interactions are modelled using techniques from chemical reaction modelling, in which concentrations of substances influence how quickly a certain change occurs: for example it might be that doubling the concentration will double the rate of the reaction.

The models to follow involve different species, analogous to chemical substances, but the terms representing photobleaching and other processes show exactly the linear behaviour of doubling the concentration of fluorescence causing the rate of reaction to double. Given that the equations capture the phenomena of diffusion and chemical reactions, the equations are termed reaction-diffusion equations.

Estimation and Comparison of Parameters Early efforts to estimate and compare model parameters used an automated approach but it soon became apparent that, given the variability between chloroplasts, modelling photobleaching in a compartment as small as the chloroplast could only justify very rough estimations of parameters and comparisons to published parameters. With this in mind, parameter estimations and comparisons are shown in figures to allow the reader to judge the accuracy of the author's estimations made by eye and described in captions and the main

text.

5.1 The Single-Species FLIP Reaction-Diffusion Model

The stromally localized TP-GFP and membrane anchored Hcf106-GFP are modelled as single-species in a reaction-diffusion model to simulate the fluorescence u in the focal slice domain Ω and the photobleaching experiments

$$\frac{\partial u}{\partial t} - \kappa \Delta u + \alpha u + \beta I(t,x) u = 0$$

With boundary condition $\frac{\partial u}{\partial \boldsymbol{n}} = 0$ where $\boldsymbol{n}$ is the outward pointing normal, κ is the diffusion coefficient, $\alpha \in \mathbb{R}$ is the observational photobleaching factor, β is the FLIP spot bleaching factor and $I(t,x)$ is a spatio-temporal indicator function that is unity only within some bleach region Ω' and only during the spot bleach time interval. Discretizing this equation with $u^h = \sum_{i=1}^{N} q_i(t)\Phi_i$ and using backward Euler time-stepping gives

$$\boldsymbol{M}\boldsymbol{q}(t+\delta t) + \kappa \delta t \boldsymbol{K}\boldsymbol{q}(t+\delta t) + \alpha \delta t \boldsymbol{M}\boldsymbol{q}(t+\delta t) + \delta t \boldsymbol{M}_{\beta}\boldsymbol{q}(t+\delta t) = \boldsymbol{M}\boldsymbol{q}(t)$$

where $\boldsymbol{M}$ is the mass matrix, $\boldsymbol{K}$ is the stiffness matrix and

$$\boldsymbol{M}_{\beta} = \left(\int_{\Omega} \beta I(t,x) \Phi_i \Phi_j \, \mathrm{d}x \right)_{ij}$$

is the spot bleach matrix.

Figure 5.1: Gaussian filtering of FLIP initial condition. The first frame in each row is an initial frame from the small bleach region data. The following five frames on the row are after application of a Gaussian filter with $\sigma = 1, 2, 3, 4, 5$ respectively. The constructs are **(A)** TP-GFP, **(B)** Hcf106-GFP, **(C)** pre23kΔTPP-GFP and **(D)** pre23k-GFP. The scale bar is 5 μm in length.

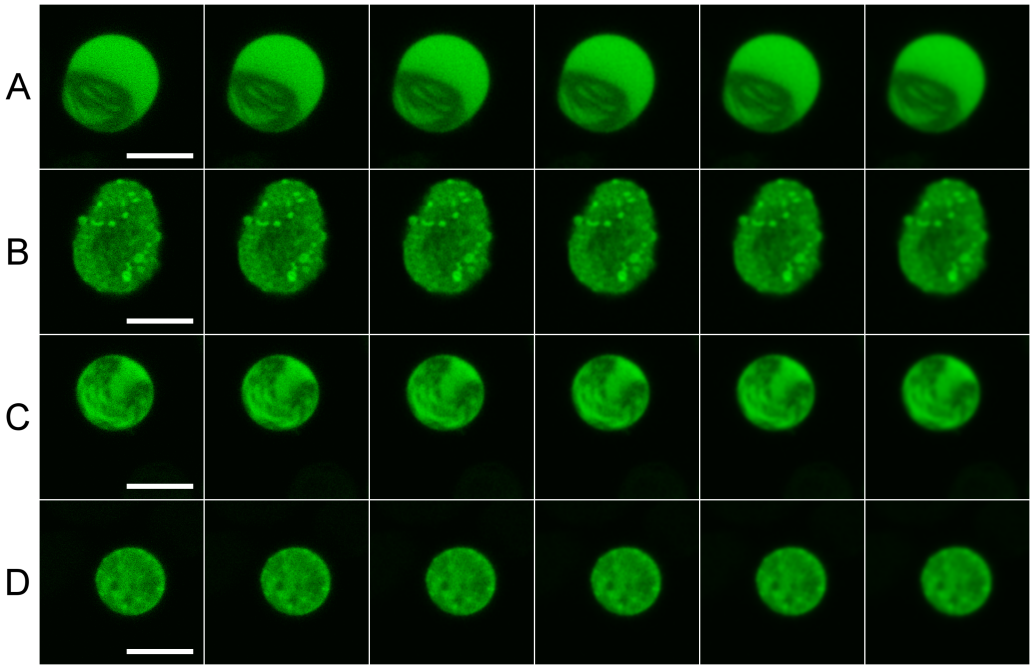

The chloroplast geometry We pick one experimental repetition for each construct to take through further analysis. The geometry of the chloroplast as seen in our confocal slice is extracted and this geometry is used as the domain for a 2D diffusion model of our modified FLIP experiments. A series of five Gaussian filters are applied separately to the initial frame as shown in figure 5.1 and then to the first-bleach frames as shown in figure 5.2. The first columns of images in these figures, where no Gaussian filter has been applied, look reasonably suitable for analysis but bilinear

Figure 5.2: Gaussian filtering must leave the bleach region resolved. The first frame in each row is a first bleach frame from the small bleach region data. The following five frames on the row are after application of a Gaussian filter with $\sigma = 1, 2, 3, 4, 5$ respectively. The constructs are **(A)** TP-GFP, **(B)** Hcf106-GFP, **(C)** pre23kΔTPP-GFP and **(D)** pre23k-GFP. The scale bar is 5 μm in length.

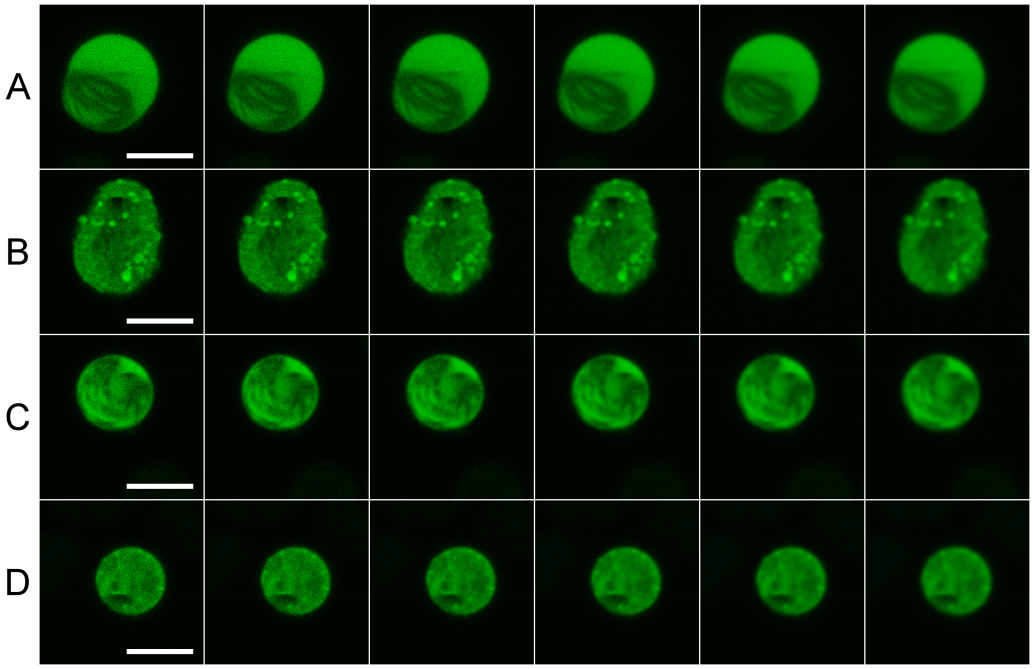

plots in figures 5.3 and 5.4 show that the unfiltered images are very noisy and a close up view would show the domain is covered in spikes. From the bilinear plot figures we pick $\sigma = 4.0$ as a suitable Gaussian filtering parameter.

The Gaussian filtered first frames are thresholded at 5%, 10%, 20% and 30% of the maximum pixel value as shown in figure 5.5. A threshold of 20% is picked as a suitable value and the geometries are extracted using the marching squares algorithm in the Visualization Toolkit (VTK) software

Figure 5.3: Bilinear plot of Gaussian filtered initial conditions. The first bilinear plot in each row is an initial frame from the small bleach region data. The following five bilinear plots on the row are after application of a Gaussian filter with $\sigma = 1, 2, 3, 4, 5$ respectively. The constructs are **(A)** TP-GFP, **(B)** Hcf106-GFP, **(C)** pre23kΔTPP-GFP and **(D)** pre23k-GFP. The parameter $\sigma = 4.0$ is selected for use in continuing analysis. The scale bar is 5 μm in length. The colour scale (omitted to avoid clutter) ranges from red at 100%, green at 50% and down to blue at 0% of maximum intensity.

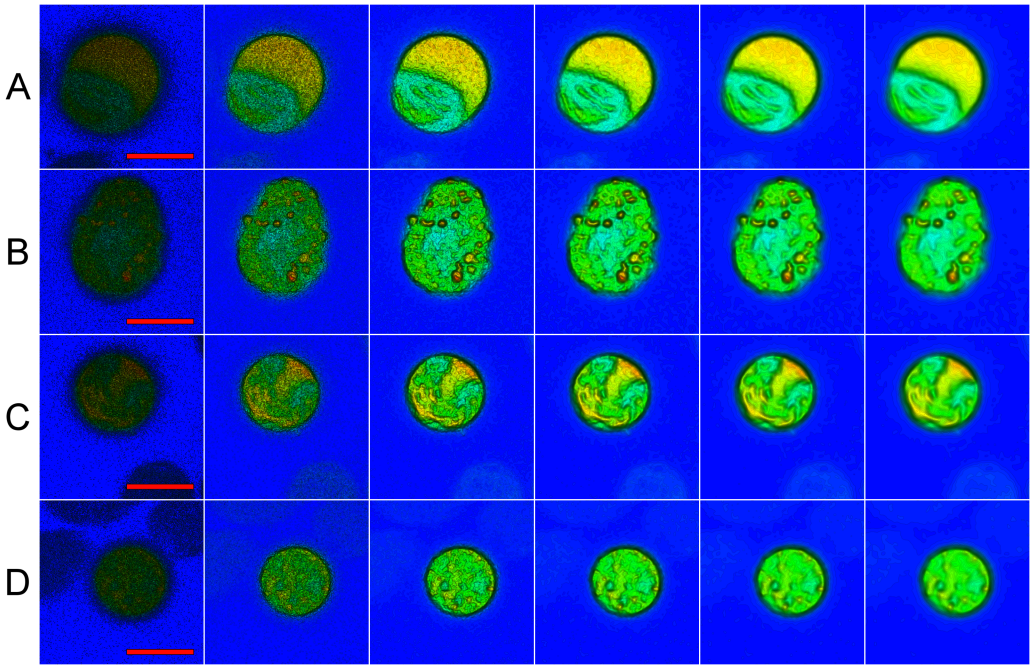

graphical library.

Selection of some parameters For $\beta = 0$ we may work out a suitable global bleach value α. We observe from figure 3.10 that three out of the four observational photobleaching graphs reach approximately 70% after

Figure 5.4: Bilinear plots of Gaussian filtered first bleach frames. The first bilinear in each row is a first bleach frame from the small bleach region data. The following five bilinear plots on the row are after application of a Gaussian filter with $\sigma = 1, 2, 3, 4, 5$ respectively. The constructs are **(A)** TP-GFP, **(B)** Hcf106-GFP, **(C)** pre23kΔTPP-GFP and **(D)** pre23k-GFP. The parameter $\sigma = 4.0$ is selected for use in continuing analysis. The scale bar is 5 μm in length. The colour scale (omitted to avoid clutter) ranges from red at 100%, green at 50% and down to blue at 0% of maximum intensity.

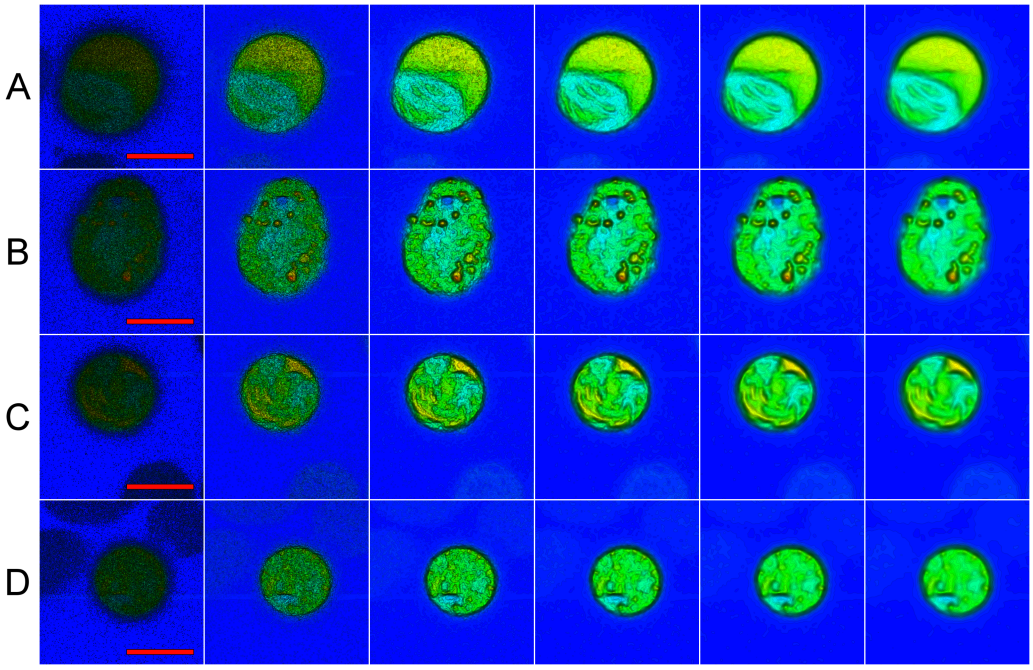

the conclusion of the experiment and from this we may deduce that

$$\alpha = -\frac{\ln(0.7)}{71 \times 0.754} \approx 0.00666259$$

The value of 70% is chosen for convenience. We use table 1.4 to select a range of suitable diffusion parameters to test and these are shown in table 5.1.

Figure 5.5: Thresholding of FLIP initial condition. The first frame in each row is an initial frame from the small bleach region data after application of a Gaussian filter with $\sigma = 4$. The following five frames on the row are after thresholding at respectively 5%, 10%, 20% and 30%. The constructs are **(A)** TP-GFP, **(B)** Hcf106-GFP, **(C)** pre23kΔTPP-GFP and **(D)** pre23k-GFP. The 20% threshold is selected for use in continuing analysis. The scale bar is 5 μm in length.

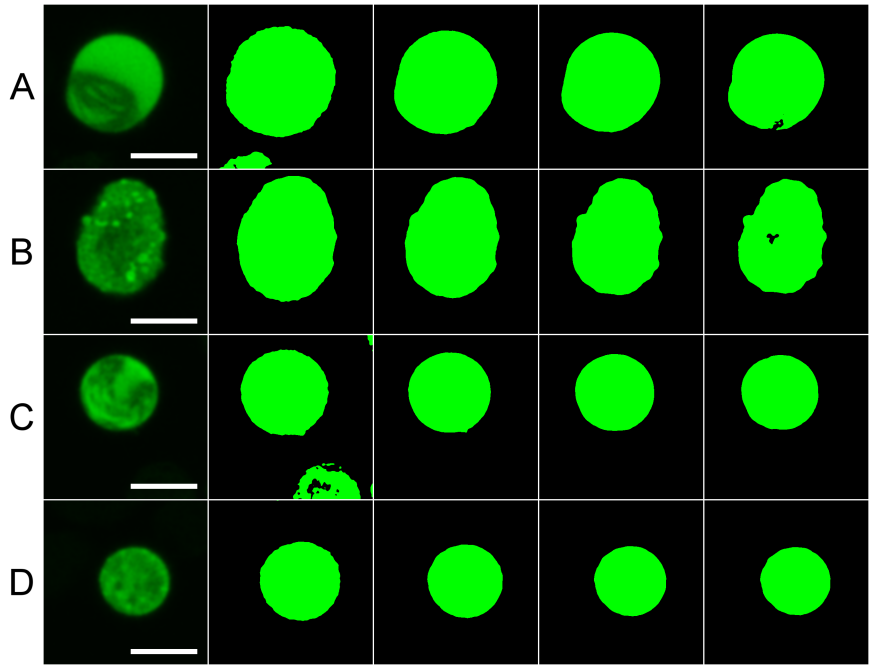

Finding suitable parameters for Hcf106-GFP We choose $\beta = 10^2\alpha$ as a first guess and take values for the diffusion coefficient within the range reported in the literature. The results from a run with $l = 8$ levels of complete refinement are shown in figure 5.6 where we see that **(D)** appears completely unsuitable and the best value appears to be 10^{-11} cm^2 s^{-1} which is the order of magnitude of the diffusion coefficient of thylakoid membrane proteins reported in table 1.4. Comparing figures in the second column in figure 5.6 shows that the value of $\beta = 10^2\alpha$ is perhaps too small so we take $\kappa = 10^{-11}$ cm^2 s^{-1} and try a range of β values in figure 5.7. We see that for

Table 5.1: Diffusion coefficient conversions for simulation. The confocal image of 512×512 pixels is a square with sides of length 12.3 μm, and 1 μm = 10^{-4} cm so we have the following conversions ("px" represents a simulation unit length)

In cm^2s^{-1}	**In px^2s^{-1}**
10^{-11}	1.73273
10^{-10}	17.3273
10^{-9}	173.273
10^{-8}	1732.73

such a low value of κ the spread of the bleach region is diffusion limited and large values of β change little in later frames.

Finding suitable parameters for TP-GFP A similar strategy is adopted for TP-GFP where we immediately eliminate **(B)** $\kappa = 10^{-10}$ in figure 5.8. We try the remaining options $\kappa = 10^{-9}, 10^{-8}$ in turn as shown in figures 5.9, 5.10 which suggest a suitable combination is $\kappa = 10^{-8}$ and $\beta = 10^3\alpha$.

5.2 The Multi-Species FLIP Reaction-Diffusion Model

In order to capture the dynamics of the more complicated Tat substrate constructs pre23kΔTPP-GFP and pre23k-GFP, we move from the single-species

Figure 5.6: PUM FLIP simulation: $\beta = 10^2\alpha, \kappa = 10^{-12}, 10^{-11}, 10^{-10}$ for respectively **(B-D)**. Row **(A)** shows frames taken from one of the Hcf106-GFP data series in order to help determine a suitable value for the diffusion parameter of a membrane-bound species. The columns, from left to right, represent the first frame, first-bleach frame (of 50), last-bleach frame, first post-bleach frame (of 20) and final post-bleach frame, respectively, in the same way as the confocal data has been presented. Rows **(B-D)** are from single-species simulations. The parameter used in row **(B)** is rejected as the bleach region has not spread as much as shown in the data. The parameter used in row **(D)** is rejected as the high mobility causes too great a spread of the bleach region and especially at the end of the sequence. The most suitable value appears to be $\kappa = 10^{-11}$. The simulations shown below and all single-species simulations are carried out with refinement level $l = 7$, cover factor $\alpha_c = 1.1$ and using a product nine-point $q = 9$ Gauss-Legendre rule as the base numerical integration scheme.

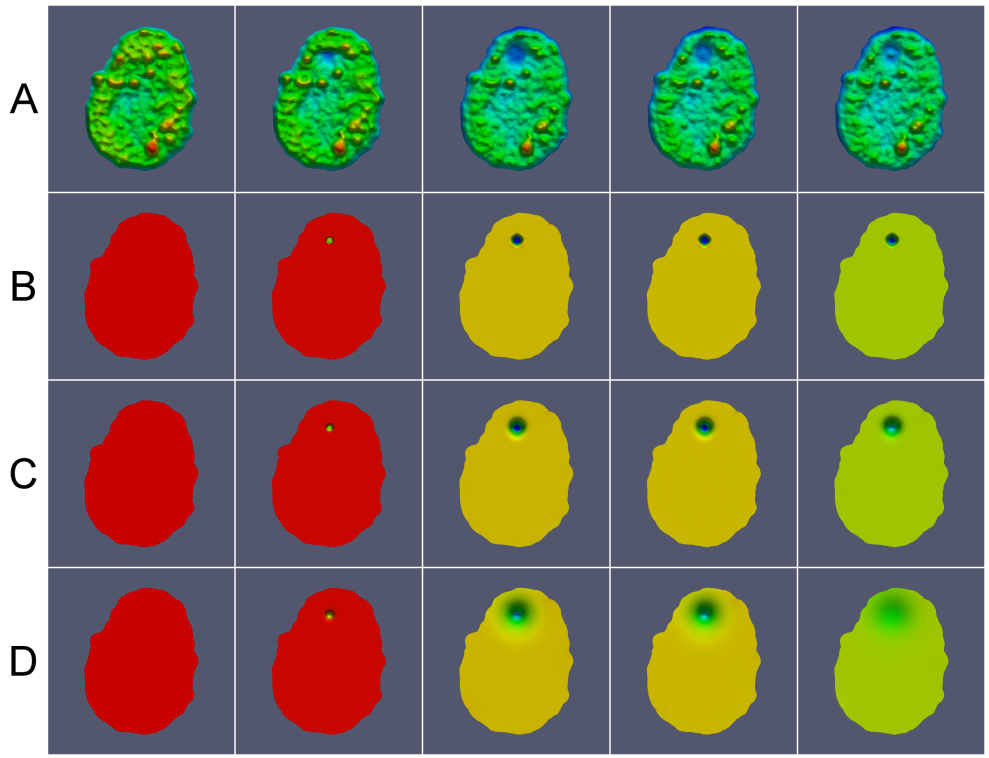

Figure 5.7: PUM FLIP simulation: $\kappa = 10^{-11}, \beta = 10^2\alpha, 10^3\alpha, 10^4\alpha$ for respectively **(B-D)**. Row **(A)** shows frames taken from one of the Hcf106-GFP data series in order to help determine a suitable value for the spot bleach parameter β. Rows **(B-D)** are from single-species simulations using the diffusion parameter $\kappa = 10^{-11}$ chosen in figure 5.6. The spot bleach parameter used in row **(B)** is rejected as the first-bleach frame (column 2) shows too shallow a bleach. The spot bleach parameter used in row **(D)** is rejected as the first-bleach frame (column 2) shows a bleach spot with very low values of fluorescence compared to the data. In searching for a suitable spot bleach parameter for an immobile species, $\beta = 10^3\alpha$ seems suitable but the aim will be to choose β also suitable for mobile species.

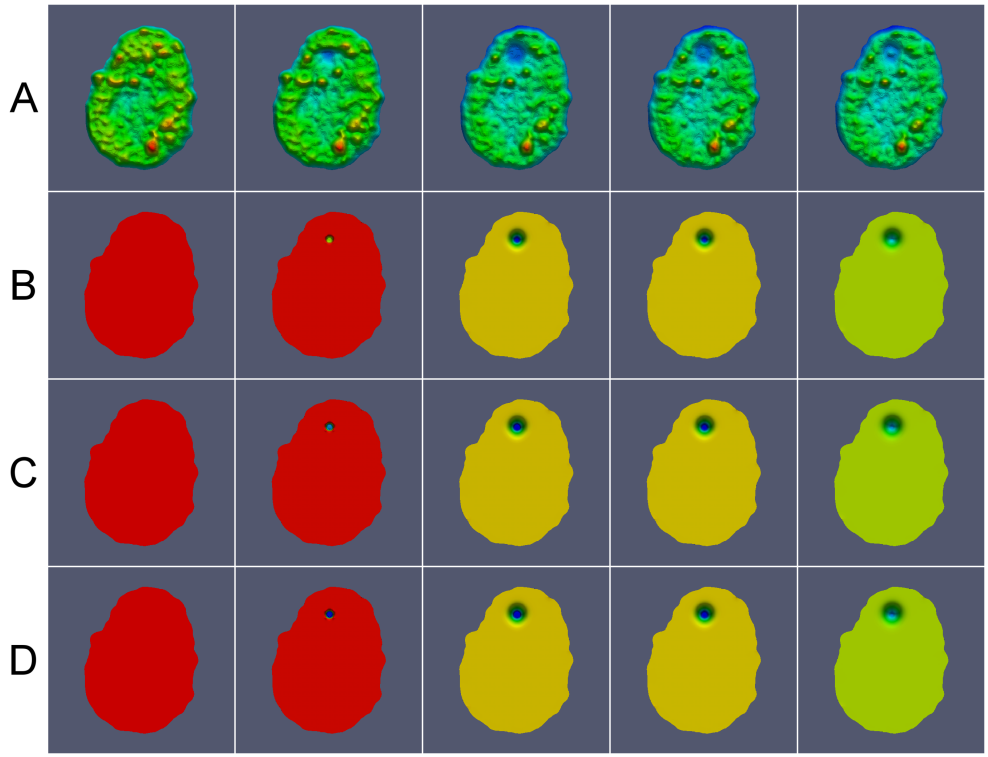

Figure 5.8: PUM FLIP simulation: $\beta = 10^2\alpha, \kappa = 10^{-10}, 10^{-9}, 10^{-8}$ for respectively **(B-D)**. Row **(A)** shows frames taken from one of the TP-GFP data series in order to help determine a suitable value for the apparent diffusion parameter κ and the spot bleach parameter β. Rows **(B-D)** are from single-species simulations. The parameter combination used in rows **(B-C)** are rejected as recovery is incomplete in the first post-bleach frame (column 4). The parameter combination used in **(D)** is rejected as the spot bleach region is insufficiently distinct.

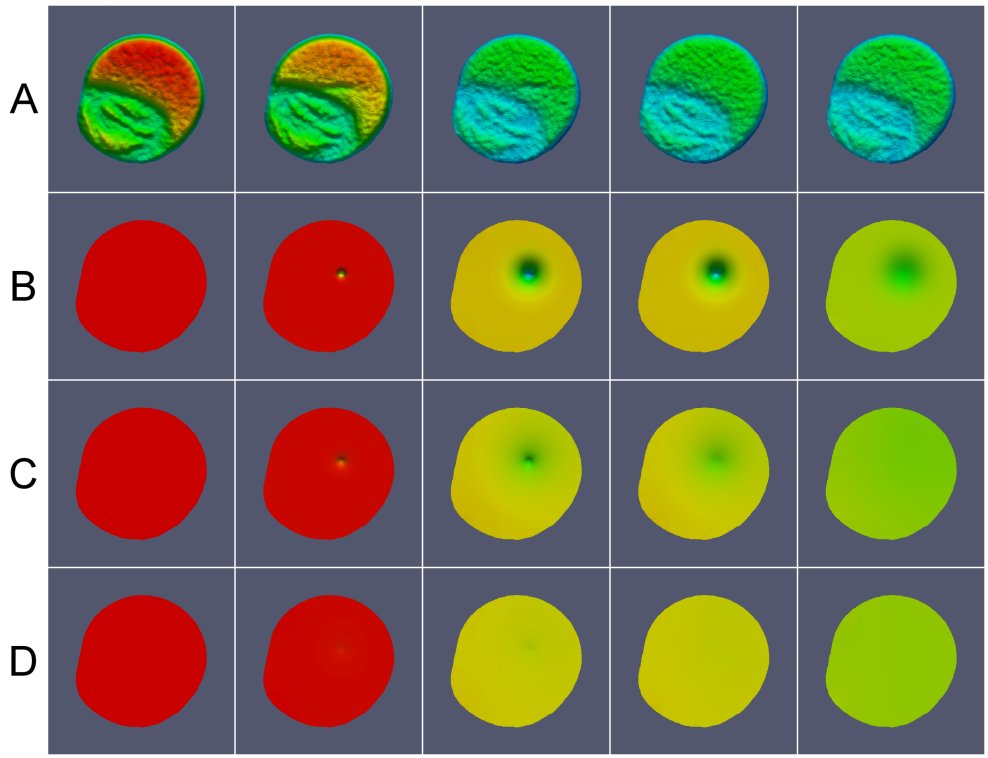

Figure 5.9: PUM FLIP simulation: $\kappa = 10^{-9}, \beta = 10^3\alpha, 10^4\alpha, 10^5\alpha$ for respectively **(B-D)**. Row **(A)** shows frames taken from one of the TP-GFP data series in order to help determine a suitable value for the apparent diffusion parameter κ and the spot bleach parameter β. Rows **(B-D)** are from single-species simulations. The parameter combinations in rows **(B-D)** are rejected for displaying too large a bleach region and incomplete recovery in the first post-bleach frame (column 4).

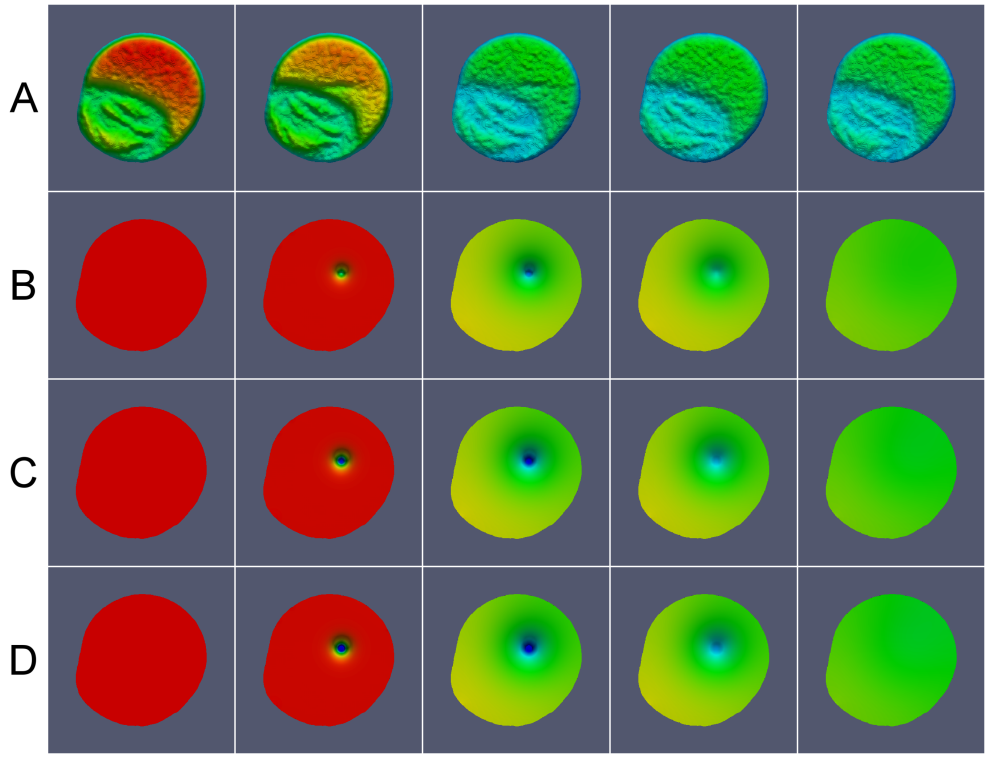

Figure 5.10: PUM FLIP simulation: $\kappa = 10^{-8}, \beta = 10^3\alpha, 10^4\alpha, 10^5\alpha$ for respectively **(B-D)**. Row **(A)** shows frames taken from one of the TP-GFP data series in order to help determine a suitable value for the apparent diffusion parameter κ and the spot bleach parameter β. Rows **(B-D)** are from single-species simulations. The parameter combinations in rows **(C-D)** are rejected for too large a bleach region displayed in the first bleach frame (column 2) and excessive fluorescence depletion from the last-bleach frame onwards (columns 3 to 5). A suitable combination of parameters for a TP-GFP is $\kappa = 10^{-8}$ and $\beta = 10^3\alpha$.

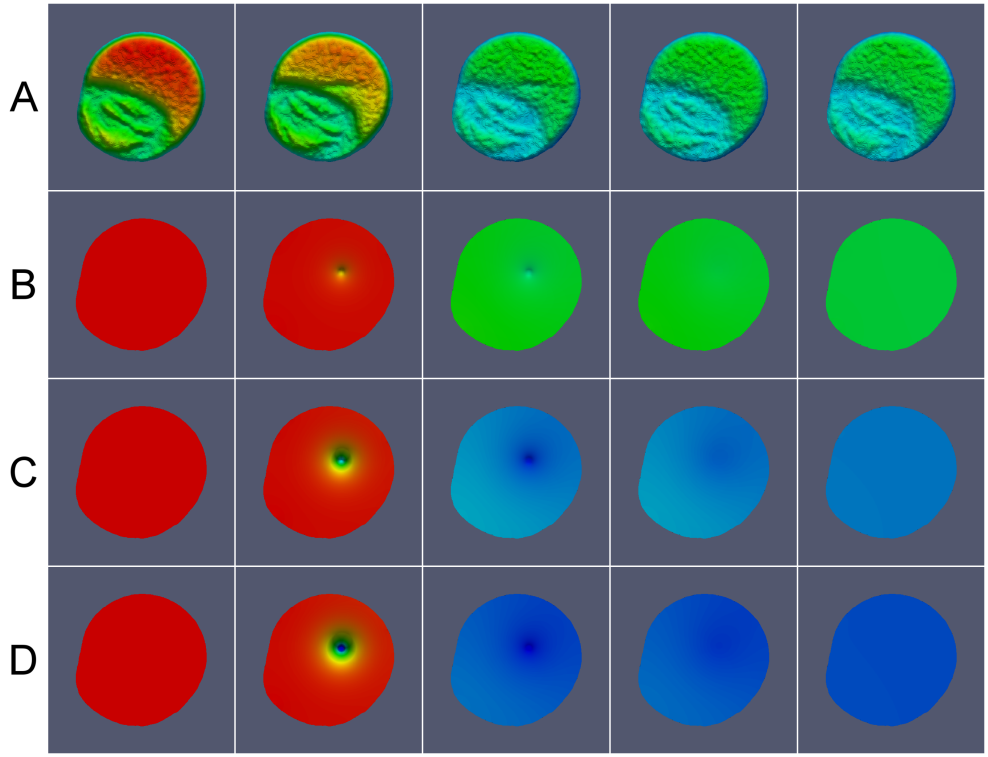

model to a multi-species model and furthermore have two compartments: we model the fluorescent species both in the focal slice compartment, which is observed by the confocal microscope, and a compartment representing the rest of the chloroplast outside this focal slice.

In order to match our data, the confocal images, which are spatially two dimensional, both compartments are domains with two spatial dimensions in the simulation, but both represent domains with three spatial dimensions in the experiment. Within each of the compartments we will model a mobile state corresponding to residence in the stromal phase and not associated with the thylakoid membrane; and a second less mobile (possibly immobile) state representing association with the thylakoid membrane and hence restricted movement. A micro-scale model is used without an explicit spatial representation of the thylakoid membrane system so the movement of the species in our model is homogeneous and isotropic. The discretization of the domains is shown in figure 5.11.

Four fluorescent species S^i with concentrations u^i for $i \in \{1, 2, 3, 4\}$ are modelled. The concentrations of fluorescence in the focal slice compartment Ω_f in respectively the mobile and less mobile states will be u^1 and u^2. The concentrations of the fluorescence in the compartment representing the rest of the chloroplast Ω_r outside the focal slice in the mobile and less mobile states will be u^3 and u^4 respectively.

The actual movement of the fluorescent protein populations and hence

the redistribution of the fluorescence concentration u^i will be assumed to be well-modelled by diffusion at the microscale with diffusion coefficients κ^i. We may take the thylakoid membrane to be completely immobile within the chloroplast and the membrane-bound or membrane-associated fluorescent population to be similarly rendered completely immobile, in which case $\kappa^2 = \kappa^4 = 0$. The alternative is to assume there is some motion of the thylakoid membrane within the chloroplast during the course of the experiment or that the membrane-associated population is able to move following the surface of the thylakoid membrane so that these populations are not completely immobile and $\kappa^2 \neq 0, \kappa^4 \neq 0$. The previous comparisons of single-species simulations to experimental data suggest it is worth allowing for a non-zero diffusion coefficient to model the membrane-associated fluorescent population.

Within each compartment, the possibility of transition from membrane-associated to non-associated states will be modelled by the simple first-order reversible reactions

$$S^1 \underset{a_{21}}{\overset{a_{12}}{\rightleftharpoons}} S^2$$
$$S^3 \underset{a_{43}}{\overset{a_{34}}{\rightleftharpoons}} S^4$$

where a_{ij} is the first-order transition rate from S^i to S^j with a_{ji} defined analogously.

It will be assumed that the thylakoid membrane system is sufficiently

immobile that we do not have to consider its movement between the focal slice and the rest of the chloroplast outside the focal slice so that the interchange of mobile fluorescent populations between the two compartments Ω_f and Ω_r will be governed by the values u^1 and u^3. We choose the form of the flux, or coupling, term in the equation for u^1 between the smaller focal slice compartment and the larger remainder of the chloroplast to be first-order dependent on the difference in concentration $u^3 - u^1$ with a flux parameter a_c. Concentrations in the focal slice are converted to concentrations in the remainder of the chloroplast by multiplication by $|\Omega_f|$, the volume of the focal slice, to get the absolute number of fluorescent molecules of the species; and division by $|\Omega_r|$, the volume of the rest of the chloroplast, to get the concentration in the compartment representing the rest of the chloroplast. Hence the volume adjustment factor c appears in the equation for u^3.

$$c := \frac{|\Omega_f|}{|\Omega_r|} < 1$$

The full set of equations is then

$$\begin{aligned}
\frac{\partial u^1}{\partial t} - \kappa^1 \Delta u^1 + \alpha_f u^1 + \beta_f I(x) u^1 &= -a_{12} u^1 + a_{21} u^2 + a_c (u^3 - u^1) \\
\frac{\partial u^2}{\partial t} - \kappa^2 \Delta u^2 + \alpha_f u^2 + \beta_f I(x) u^2 &= -a_{21} u^2 + a_{12} u^1 \\
\frac{\partial u^3}{\partial t} - \kappa^3 \Delta u^3 + \alpha_r u^3 + \beta_r I(x) u^3 &= -a_{34} u^3 + a_{43} u^4 + c a_c (u^1 - u^3) \\
\frac{\partial u^4}{\partial t} - \kappa^4 \Delta u^4 + \alpha_r u^4 + \beta_r I(x) u^4 &= -a_{43} u^4 + a_{34} u^3
\end{aligned}$$

With zero Neumann boundary conditions in the respective domains $\frac{\partial u^i}{\partial \mathbf{n}} = 0$. The parameters α_f and β_f are the bleaching parameters for the focal slice

with separate parameters α_r and β_r for the rest of the chloroplast outside the focal slice. We carry out a check that the reaction scheme, in the absence of diffusion ($\kappa^i = 0$) and sinks ($\alpha_f = \beta_f = \alpha_r = \beta_r = 0$), conserves the total number of fluorescent molecules

$$|\Omega_f|\left(\frac{\partial u^1}{\partial t} + \frac{\partial u^2}{\partial t}\right) + |\Omega_r|\left(\frac{\partial u^3}{\partial t} + \frac{\partial u^4}{\partial t}\right) = 0$$

The set of four equations are discretized so that a PUM simulation may be carried out. To simplify the presentation, the global bleach terms and spot bleach terms are omitted as their proper handling is no different from the other linear terms.

$$\begin{aligned}
\frac{\partial u^i}{\partial t} - \kappa^i \Delta u^i &= \sum_{j \neq i} a_{ji} u^j - \left(\sum_{j \neq i} a_{ij}\right) u^i + a_c(u^3 - u^1) && \text{for} \quad i = 1 \\
\frac{\partial u^i}{\partial t} - \kappa^i \Delta u^i &= \sum_{j \neq i} a_{ji} u^j - \left(\sum_{j \neq i} a_{ij}\right) u^i && \text{for} \quad i = 2, 4 \\
\frac{\partial u^i}{\partial t} - \kappa^i \Delta u^i &= \sum_{j \neq i} a_{ji} u^j - \left(\sum_{j \neq i} a_{ij}\right) u^i + c a_c(u^1 - u^3) && \text{for} \quad i = 3
\end{aligned}$$

The backward Euler scheme is again used for the time-dependent terms. The coupling term is treated explicitly in contrast to other terms which are treated implicitly where possible for better stability. This is in keeping with the general case when the coupling term may be non-linear and would not

admit an implicit treatment.

$$u^i_{t+\delta t} - \delta t \kappa^i \Delta u^i_{t+\delta t} = u^i_t + \delta t \left(\sum_{j \neq i} a_{ji} u^j_t - u^i_{t+\delta t} \sum_{j \neq i} a_{ij} \right) + a_c (u^3_t - u^1_t) \delta t \quad i = 1$$

$$u^i_{t+\delta t} - \delta t \kappa^i \Delta u^i_{t+\delta t} = u^i_t + \delta t \left(\sum_{j \neq i} a_{ji} u^j_t - u^i_{t+\delta t} \sum_{j \neq i} a_{ij} \right) \quad i = 2, 4$$

$$u^i_{t+\delta t} - \delta t \kappa^i \Delta u^i_{t+\delta t} = u^i_t + \delta t \left(\sum_{j \neq i} a_{ji} u^j_t - u^i_{t+\delta t} \sum_{j \neq i} a_{ij} \right) + c a_c (u^1_t - u^3_t) \delta t \quad i = 3$$

The terms for time $t + \delta t$ are gathered on the left and the terms for time t are gathered on the right.

$$\left(1 + \delta t \sum_{j \neq i} a_{ij} \right) u^i_{t+\delta t} - \delta t \kappa^i \Delta u^i_{t+\delta t} = u^i_t + \delta t \sum_{j \neq i} (a_{ji} u^j_t) + a_c (u^3_t - u^1_t) \delta t \quad i = 1$$

$$\left(1 + \delta t \sum_{j \neq i} a_{ij} \right) u^i_{t+\delta t} - \delta t \kappa^i \Delta u^i_{t+\delta t} = u^i_t + \delta t \sum_{j \neq i} (a_{ji} u^j_t) \quad i = 2, 4$$

$$\left(1 + \delta t \sum_{j \neq i} a_{ij} \right) u^i_{t+\delta t} - \delta t \kappa^i \Delta u^i_{t+\delta t} = u^i_t + \delta t \sum_{j \neq i} (a_{ji} u^j_t) + c a_c (u^1_t - u^3_t) \delta t \quad i = 3$$

The multi-species model greatly increases the number of parameters so we choose some values to give reasonable behaviour. The apparent diffusion coefficient values for the mobile species $\kappa^1 = \kappa^3 = 10^{-8}$ cm^{2}s^{-1} and the immobile species $\kappa^2 = \kappa^4 = 10^{-11}$ cm^{2}s^{-1} determined in the single-species simulations will be retained for the multi-species simulation. The global bleach parameter for the focal plane will be kept at $\alpha_f = 0.00666259$ and

the spot bleach parameter for the focal plane shall be $\beta_f = 10^3\alpha_f$. The corresponding bleach parameters α_r and β_r for the rest of the chloroplast will be either zero or correspond to the focal plane parameters. The coupling parameter is chosen to be $a_c = 0.04$ and the focal slice will be taken as 1% the volume of the chloroplast so $c = 1/99$. For TP-GFP, the binding and unbinding parameters are chosen as $a_{12} = a_{21} = a_{34} = a_{43} = 0$, the initial percentage mobile is 100% and initial percentage immobile is 0%. For Hcf106-GFP, the binding and unbinding parameter s are chosen as $a_{12} = a_{21} = a_{34} = a_{43} = 0$, the initial percentage mobile is 0% and initial percentage immobile is 100%. For pre23kΔTPP-GFP, the binding and unbinding parameters are chosen as $a_{12} = a_{21} = a_{34} = a_{43} = 0.01$, the initial percentage mobile is 10% and initial percentage immobile is 90%. For pre23k-GFP, the binding and unbinding parameters are chosen as $a_{12} = a_{21} = a_{34} = a_{43} = 0.005$, the initial percentage mobile is 40% and initial percentage immobile is 50%.

After spot photobleaching stops in the single-species model, the global observational photobleaching continues to reduce the total fluorescence in the focal slice so the single-species model is unable to reproduce the rise in focal slice fluorescence see in figures 3.10 and 3.18. In contrast, the multi-species model is able to capture a good approximation of the fluoresence depletion profiles as evident in figure 5.12, and applying the observational photobleaching correction to simulation results in figure 5.13 gives a good approximation of the corresponding data-derived figures 3.11 and 3.19.

It was found that despite the fact the laser of the confocal microscope

was focussed on a thin slice within the chloroplast, our simulation suggested there was a considerable amount of out-of-focal-slice bleaching when the case $\alpha_r = \beta_r = 0$, figure 5.15, was compared to $\alpha_r = \alpha_f$ and $\beta_r = \beta_f$, figure 5.12. The significance of fluoresence recovery into the focal slice is reinforced by panel **(B)** of figure 5.13 which matches better the corresponding panel of figures 3.11 and 3.19 than is the case for figure 5.14. For large specimens, out-of-focal-slice bleaching is less significant but we must be especially careful as chloroplasts are at the low size range of biological specimens suitable for light microscopy, and the combination of high magnification and reasonably extended imaging time risks an unfavourable signal to noise ratio.

5.3 The FLIP Inhomogeneous Diffusion Model

We show how PUM may be used to capture the complex geometry of the thylakoid membrane system by employing an inhomogeneous diffusion model (Siggia et al., 2000) with the single-species reaction-diffusion equation as defined before but a modification is made to the diffusion term

$$\frac{\partial u}{\partial t} - \kappa \nabla \cdot (\bar{u} \nabla (u/\bar{u})) + \alpha u + \beta I(t,x) u = 0$$

where $\bar{u}$ is the initial fluorescence distribution describing the inhomogeneity that should be preserved. Taking just the modified diffusion term,

Figure 5.11: Domain discretization and integration points. Spatially two-dimensional, chloroplast domains are shown for **(A)** TP-GFP, **(B)** Hcf106-GFP, **(C)** pre23kΔTPP-GFP and **(D)** pre23k-GFP with the boundary shown in black. A complete refinement to d-binary tree level $l = 4$ has been performed and the unexpanded patches are shown with red borders. The cover factor $\alpha_c = 1.1$ was used and the numerical integration points, shown in blue, are seen to cluster near the edge of the unexpanded patches because integration regions are based on intersections of patches, so that integrands have continuous derivatives on the domain of integration. As a product nine-point $q = 9$ Gauss-Legendre rule is used as the base numerical integration scheme, there are 49 numerical integration points within the region that appears mostly white near the centre of the red-outlined unexpanded patches.

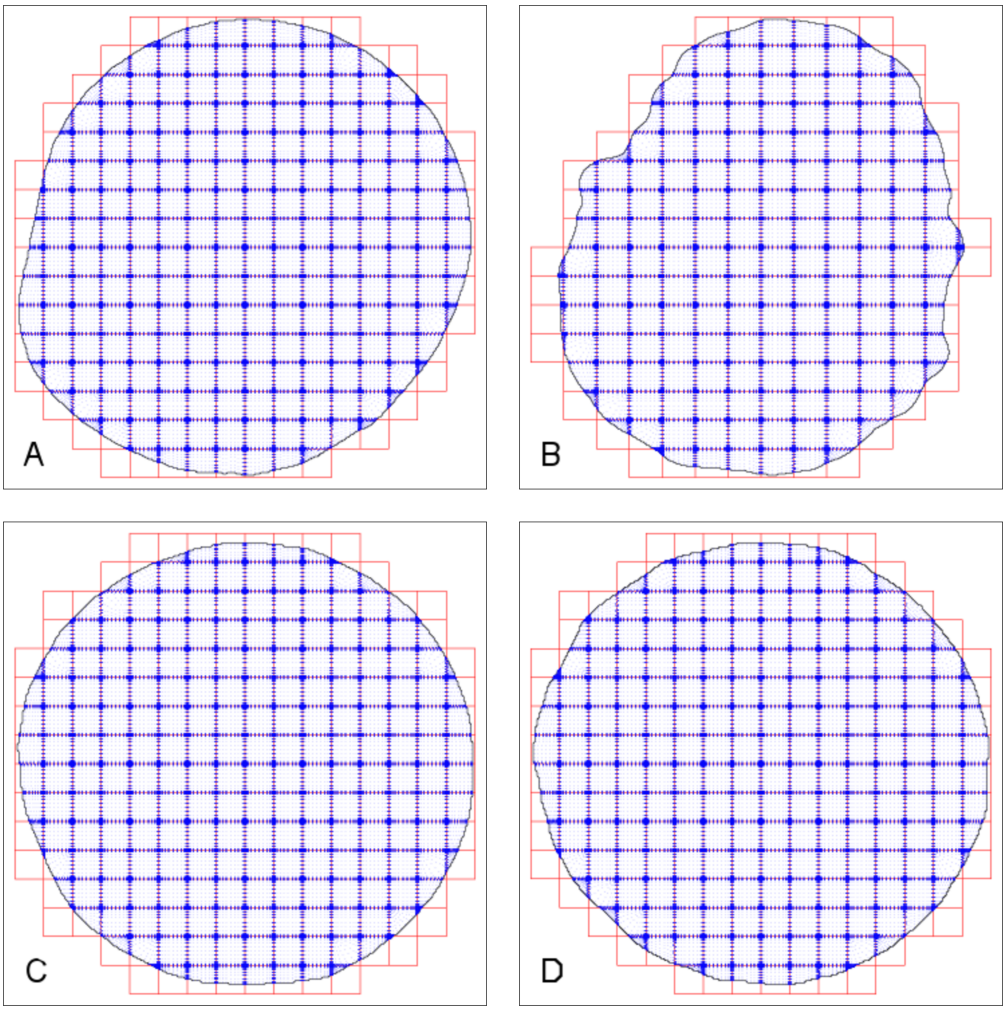

Figure 5.12: Multi-species depletion: fully global bleach. The bleach parameters are the same throughout the chloroplast: $\alpha_r = \alpha_f$ and $\beta_r = \beta_f$. With the observational bleach parameter applying throughout the chloroplast we see similar observation bleach profiles (white points) for all the four species **(A-D)** in agreement with experimental data. The slight curve of the spot photobleaching depletion slope (black points) is apparent in **(A)** and **(D)**. The effect of fluorescence recovery into the focal slice is seen in **(A)**, **(C)** and **(D)**. Spot photobleaching is less pronounced for **(B)** Hcf106-GFP which suggests the spot bleach has a tighter effect in simulation whereas the spot bleach affects a wider area in the experiment perhaps by optical effects or small movements of the sample.

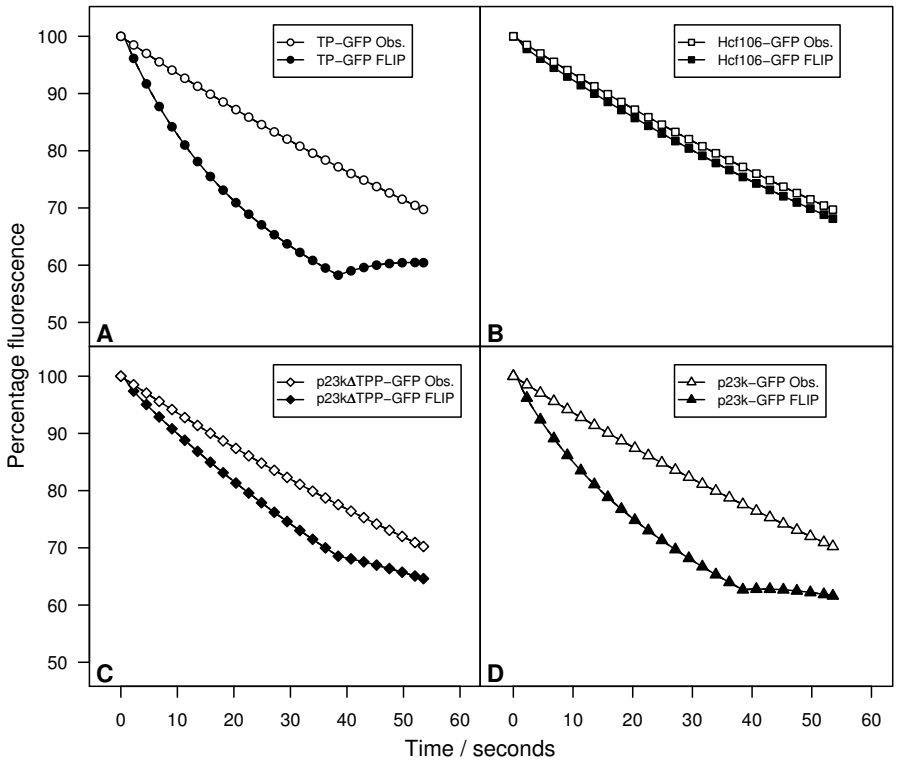

Figure 5.13: Multi-species observation correcting: fully global bleach. The bleach parameters are the same throughout the chloroplast: $\alpha_r = \alpha_f$ and $\beta_r = \beta_f$. The simulated fluorescence profiles with simulated observational photobleaching effect removed are shown in **(A)**. The same quantification of the slope magnitude is made for the simulation profile as for the experimental data profiles and this is shown in **(B)**. The fluorescence loss due to observation (white bar in **(B)**) is larger in the simulation than for the data (see figure 3.11) becase the simulation is unable to capture the initial very sharp drop seen in the data (see figure 3.10), so there is a greater loss in fluorescence in the central portion to reach the desired 70% of remaining fluorescence which is how $\alpha = \alpha_f$ was chosen.

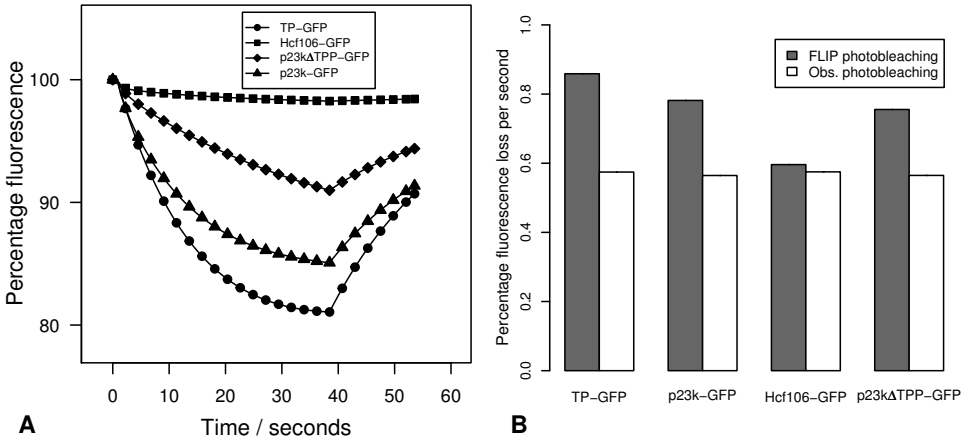

Figure 5.14: Multi-species depletion: focal slice bleach only. The bleach parameters are non-zero in the focal slice and zero in the rest of the chloroplast: $\alpha_r = 0$ and $\beta_r = 0$. The fluorescence loss profile in all four quadrants **(A-D)** are quite similar to figure 5.12 but the observational bleach profiles (white points) show there is greater recovery into the focal slice from outside in **(C-D)** and the curvature this causes is most apparent in **(A)**. The profiles for **(B)** Hcf106-GFP is unchanged as the model does not allow for the immobile fluorescence to move into or out of the focal slice.

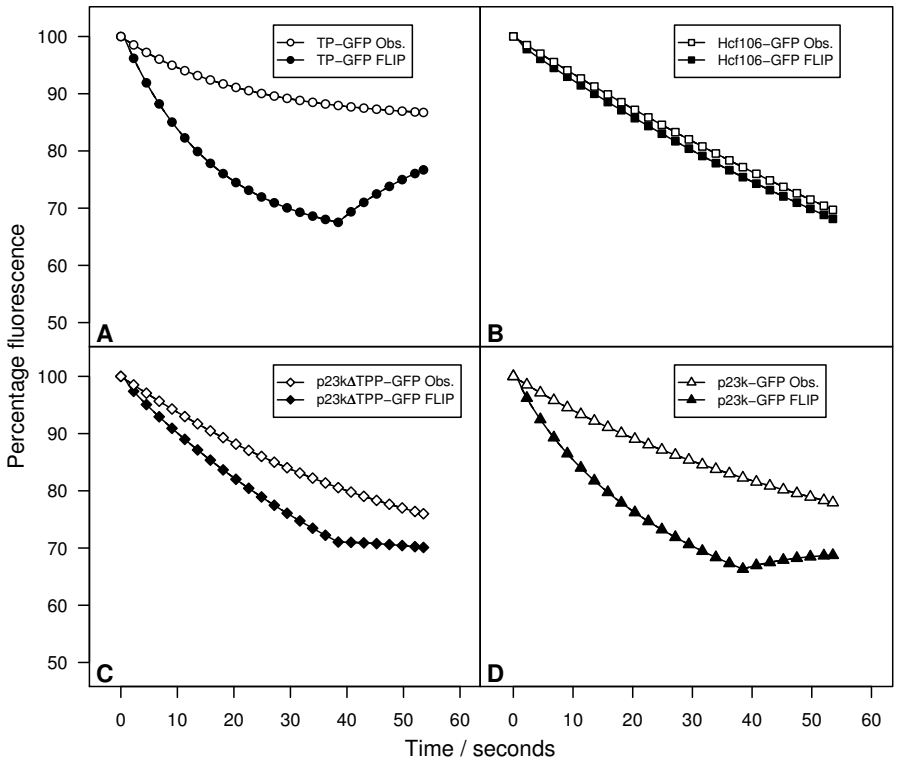

Figure 5.15: Multi-species observation correcting: focal slice bleach only. The bleach parameters are non-zero in the focal slice and zero in the rest of the chloroplast: $\alpha_r = 0$ and $\beta_r = 0$. The general shape of the profiles in quadrant **(A)** are similar to the profiles in the corresponding quadrant of figure 5.13 but quadrant **(B)** shows that there is a much greater range of observational photobleaching magnitudes (white bars) in disagreement with figure 3.11.

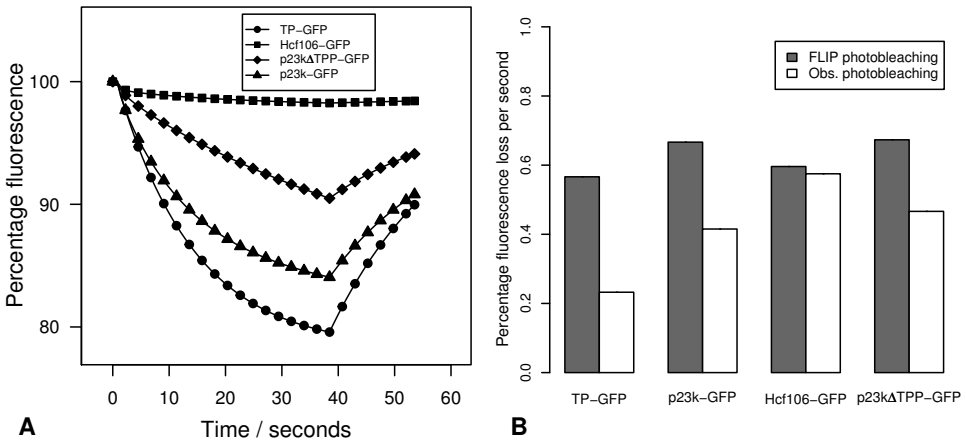

multiplying by a test function v and applying integration by parts and Green's theorem we get

$$\int_\Omega v\nabla\cdot\Big(\bar{u}\nabla(u/\bar{u})\Big)\,\mathrm{d}x - \int_{\partial\Omega} v\Big(\bar{u}\nabla(u/\bar{u})\Big)\cdot\boldsymbol{n}\,\mathrm{d}S + \int_\Omega \nabla v\cdot\Big(\bar{u}\nabla(u/\bar{u})\Big)\,\mathrm{d}x$$

We make use of the equality, for $\bar{u}\neq 0$,

$$\begin{aligned}\bar{u}\nabla(u/\bar{u}) &= \bar{u}\frac{(\nabla u)\bar{u} - u\nabla\bar{u}}{\bar{u}^2}\\ &= \nabla u - (u/\bar{u})\nabla\bar{u}\end{aligned}$$

We take $\frac{\partial u}{\partial n}$ so need only consider the interior integrand

$$\nabla v\cdot\Big(\bar{u}\nabla(u/\bar{u})\Big) = \nabla v\cdot\nabla u - (u/\bar{u})\nabla v\cdot\nabla\bar{u}$$

From this we see that only a slight modification needs to be made to the single-species discretization scheme and we only need an additional matrix

$$\boldsymbol{S} = \left(\int_\Omega \frac{\Phi_j}{\bar{u}}\nabla\Phi_i\cdot\nabla\bar{u}\;\mathrm{d}x\right)_{ij}$$

with

$$\Big(\boldsymbol{M} + \kappa\delta t\boldsymbol{K} + \alpha\delta t\boldsymbol{M} + \delta t\boldsymbol{M}_\beta + \kappa\delta t\boldsymbol{S}\Big)\boldsymbol{q}(t+\delta t) = \boldsymbol{M}\boldsymbol{q}(t)$$

Figure 5.16 shows the use of the inhomogeneous diffusion FLIP model using data from **(A)** the pre23kΔTPP-GFP construct. The structures seen within the chloroplast are preserved in a way that is consistent with the global depletion of fluorescence.

Getting to the stage of being able to present such a comparison is no

easy achievement but this is probably an appropriate point to reflect on the successes and failures along the way and to plan the best way to take our experience forward. The life sciences are demanding ever more complicated models of many different kinds and stochastic considerations are increasingly being brought into models. One pressing need is the ability to handle increasing complexity in a way that allows new functionality to be added to scientific software without harsh performance penalties.

It is hoped that the presentation of our optimized implementation of PUM will prove useful and that it serves to advance not only mesh-free research but also speaks more widely to users of computational spatial methods. Spatio-temporal computation is a highlight of modern research and I look forward to working further with such numerical methods and anticipating what the next big advances might be.

Figure 5.16: PUM inhomogeneous FLIP simulation: $\beta = 10^3\alpha, \kappa = 10^{-10}, 10^{-9}, 10^{-8}$ for respectively **(B-D)**. Row **(A)** shows frames taken from one of the pre23kΔTTP-GFP data series. Rows **(B-D)** are from inhomogeneous diffusion simulations. In contrast to the homogeneity seen in the figures for the single-species simulations, rows **(B-D)** show a better match for the data **(A)**. The spot bleach region is too distinct suggesting that either the bleach parameter β is too high or the inhomogeneous diffusion parameter κ is too low but the results show the potential for capturing features such as local depletion of a region as apparent in the last-bleach frame (column 3) of row **(C)**.

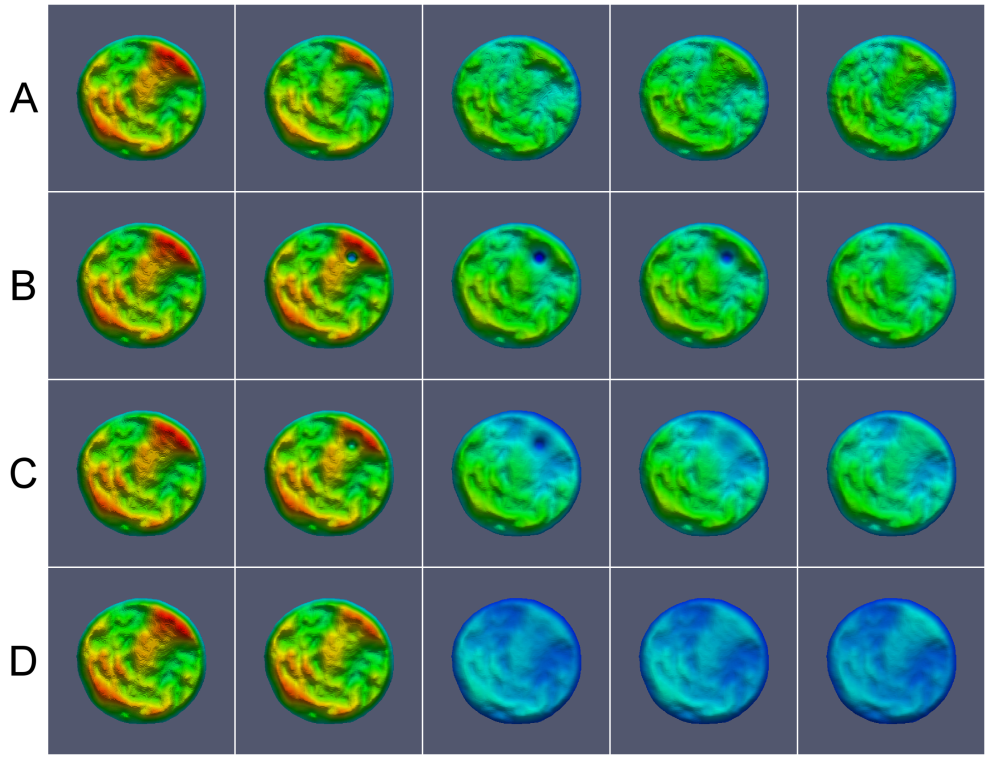

Chapter 6

In vitro Import of Tat-Targeted Fluorescent Proteins

This ambitious chapter looks ahead to laying the foundations for using fluorescence microscopy to probe the dynamics of the actual Tat translocation event together with processes considered in the previous modelling and simulation chapter. A selection of candidate *in vitro* import Tat substrate are considered and biochemical assays are used to assess suitability.

The protoplast transfection work of earlier chapters was developed before my arrival in the laboratory as part of a wider effort to observe early transient stages of Tat protein targeting. This chapter describes some of my initial work on investigating the feasibility of *in vitro* import of Tat-

targeted fluorescent proteins into isolated *Pisum sativum* thylakoids and chloroplasts.

6.1 Purification of Recombinant Tat Substrate

A colleague in the laboratory, James Barnett, provided the construct N-Strep-DmsA-YFP (both `KK` and `RR` variants on the DmsA signal peptide) in the pBAD24 plasmid. The Strep-Tag II (Schmidt et al., 1996), the amino acid tag `WSHPQFEK`, was present to allow purification by affinity chromatography (binding to Strep-Tactin supported on beads of sepharose). The bacterial Tat signal peptide of the catalytic subunit, DmsA, of the enzyme dimethyl sulphoxide (DMSO) reductase (Weiner et al., 1992; Ray et al., 2003) is used to facilitate Tat protein targeting of the yellow fluorescent protein (YFP), our intended Tat substrate. The pBAD24 plasmid confers ampicillin resistance and expression of our construct is regulated by the arabinose-inducible p_{BAD} promoter (Guzman et al., 1995).

6.2 preDmsA and pre23k Signal Peptides for Thylakoid Import

Both KK and RR signal peptide variants of preDmsA-YFP were amplified from N-Strep-preDmsA-YFP in pBAD-24 using primers forPstIpreDmsA and revYFPHindIII (see table 6.1) and subcloned as a PstI-HindIII fragment into PstI-HindIII cut pGEM-4Z. The Strep-tag II was introduced using the primer forInsStrep, its complementary oligonucleotide and the Quick-Change mutagenesis system (Stratagene) according to the protocol provided by the manufacturer to give KK/RR N-Strep-preDmsA-YFP.

Table 6.1: Primers for cloning of preDmsA-YFP constructs in pGEM-4Z and insertion of the Strep-Tag II. The first two primers were provided by a colleague, Eva Klostermann The restriction sites are indicated in the first two sequences and the Strep-Tag II sequence is indicated in the third sequence.

Primer	Sequence
forPstIpreDmsA (forward)	TTC CTG CA|G ATG AAA ACG AAA ATC C
revYFPHindIII (reverse)	GCC A|AG CTT TTA TTT GTA TAG TTC ATC C
forInsStrep	GTC GAC CTG CAG ATG TGG TCG CAC CCA CAG TTT GAA AAA TCG AAT AAA ACG

Both the KK and RR signal peptide variants of pre23k-GFP were amplified from KK/RR pre23k-GFP in pDHA using primers "NcoIpre23k inBAD" and XGFP3 (see table 6.2) and subcloned as an NcoI-XbaI fragment

Table 6.2: Primers for cloning of pre23k-GFP constructs. The NcoI restriction site is indicated in the first primer. The second primer with the XbaI indicated was provided by a colleague, Alessandra di Cola.

Primer	Sequence
NcoIpre23k inBAD	CTG CTG CAG C|CA TGG CAT CTA CAC AAT G
XGFP3	GTC GAC T|CT AGA TTA TTT GTA TAG TTC ATC C

into NcoI-XbaI cut pBAD-24. A restriction enzyme digest was performed on pre23k-GFP pDHA to recover the XbaI pre23k-GFP fragment which was subsequently subcloned into XbaI digested pGEM-4Z.

Table 6.3: Primers for cloning of N-Strep-pre23k-GFP in pGEM-4Z and pBAD-24. The XbaI restriction site and Strep-tag II are indicated for the first; and the ribosome binding site, NcoI restriction site and Strep-tag II are indicated for the second primer.

Primer	Sequence
GNS (pGEM-4Z)	GGT ACC CGG GGA TCC T|CT AGA C ATG TGG TCG CAC CCA CAG TTT GAA AAA TCG AAT GCA TCT ACA CAA TGT TTC TTG C
BNS (pBAD-24)	GCT AGC AGG AGG ATT TCA C|CA TG TGG TCG CAC CCA CAG TTT GAA AAA TCG AAT GCA TCT ACA CAA TGT TTC TTG C

The Quick-Change mutatagenesis system was again used to introduce the Strep-tag II at either the N-terminus or the C-terminus of pre23k-GFP in pGEM-4Z and pre23k-GFP in pBAD-24 using the primers shown in figures 6.3 and 6.4, and their complements.

Table 6.4: Primers for cloning C-Strep-pre23k-GFP in pGEM-4Z and pBAD-24. The XbaI restriction site and Strep-tag II are indicated for the first primer; and the Strep-tag II, stop codon and XbaI restriction site are indicated for the second primer.

Primer	Sequence
GCS (pGEM-4Z)	GGC ATG GAT GAA CTA TAC AAA AAT TCG TGG TCG CAC CCA CAG TTT GAA AAA TAA T|CT AGA GTC GAC CTGC
BCS (pBAD-24)	GGC ATG GAT GAA CTA TAC AAA AAT TCG TGG TCG CAC CCA CAG TTT GAA AAA TAA T|CT AGA GTC GAC CTG C

6.3 Radio-Isotope Labelled Imports

Unsuitability of preDmsA-YFP It was found that the mature YFP was more resistant to digestion with trypsin than either genuine pre23k or pre23k-GFP. Figure 6.1 shows the results of an experiment in which I was helped by a colleague, Peter Cain (hence the repetition with lanes 4, 5, 11 and 12). In lane 3 we see a band resulting from trypsin digestion of genuine pre23k which is suitably smaller than the mature bands common to lanes 4, 5, 6 and 7. Unfortunately there is no such separation with preDmsA-YFP where the thermolysin and trypsin resistant bands in lanes 9 and 10 are seen to co-migrate with putative successfully imported, mature YFP in lanes 11 to 14. Figure 6.2 shows the import of RR pre23k-GFP which was carried out at the same time and no such resistant band is seen in lanes 2 and 3.

Figure 6.3 shows the thylakoid import of the constructs KK/RR preDmsA-YFP and KK/RR N-Strep-DmsA-YFP competing with a test amount of recombinant RR N-Strep-DmsA-YFP. The purpose of this figure is to show that the KK variants are not processed to mature size (lanes 2, 4, 12 and 14) whereas the RR variants are processed to mature size (lanes 7, 9, 17 and 19) but unfortunately a trypsin digest is unsuitable for showing this because of the resistant band that is seen at the position of the mature band (lanes 3, 5, 8, 10, 13, 15, 18 and 20).

Unsuitability of the Strep-tag II for pre23k-GFP Figure 6.4 shows efficient import of RR pre23k-GFP into the chloroplast (lane 9) and into the thylakoid membrane system (lane 12), and the expected failure of the KK variant to reach the thylakoid lumen (lanes 5 and 6). Unfortunately an N-terminal Strep-tag II severely reduces the efficiency of import of N-Strep-pre23k-GFP as shown in figure 6.5 lanes 1 to 6. The efficiency of import for the C-terminal Strep-tag II C-Strep-pre23k-GFP is noticeably better (figure 6.6) but past experience with purification of Tat substrates suggested an N-terminal tag would yield more useful substrate because a C-terminal tag causes unwanted mature GFP to be extracted. In light of the fundamental difficulties the radio-isotope labelled imports highlighted, we did not proceed to expression and purification using the pBAD-24 constructs for *in vitro* import with the intention of observing the import by fluorescence microscopy.

Figure 6.1: Thylakoid import of genuine pre23k and preDmsA-YFP. The putative Tat substrate preDmsA-YFP (lane 8) leaves behind relatively high molecular weight digestion products when separately subjected to thermolysin and trysin digestion (lanes 9 and 10 respectively). Unfortunately these digestion products co-migrate with the putative mature DmsA-YFP (lanes 12 and 14) so the standard import assay is not suitable for analyzing the behaviour of preDmsA-YFP. In contrast, the genuine pre23k protein (lane 1) has only a comparatively low molecular weight trypsin digestion product (lane 3) which may be distinguished from the higher molecular weight mature protein (lanes 5 and 7).
1-7 genuine pre23k
8-14 preDmsA-YFP
1 genuine pre23k translation
2 thermolysin digest of genuine pre23k
3 trypsin digest of genuine pre23k
4 thylakoid fraction after import of pre23k
5 trypsin treated lane 4
6 thylakoid fraction after import of pre23k
7 trypsin treated lane 6
8 RR preDmsA-YFP translation
9 thermolysin digest of RR preDmsA-YFP
10 trypsin digest of RR preDmsA-YFP
11 thylakoid fraction after import of RR preDmsA-YFP
12 trypsin treated lane 11
13 thylakoid fraction after import of RR preDmsA-YFP
14 trypsin treated lane 13
The two molecular weight markers entirely within the figure are 30 kDa and 20.1 kDa.

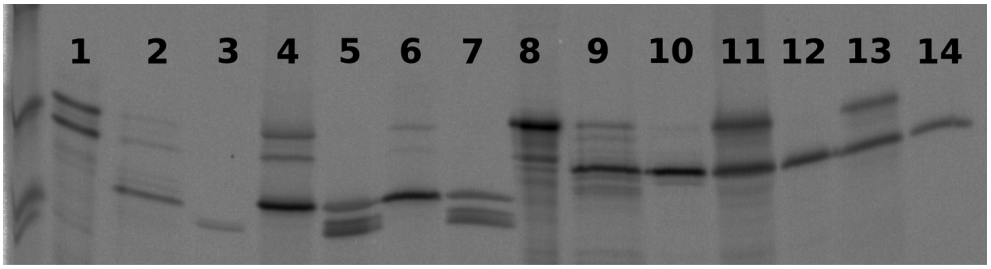

Figure 6.2: Thylakoid import of RR pre23k-GFP. In contrast to preDmsA-YFP in the previous figure, pre23k-GFP demonstrated a much lower level of thermolysin and trypsin resistant digestion products (lanes 2 and 3 respectively).
1 RR pre23k-GFP translation
2 thermolysin digest of RR pre23k-GFP
3 trypsin digest of RR pre23k-GFP
4 thylakoid fraction after import of RR pre23k-GFP
5 trypsin treated lane 4
6 thylakoid fraction after import of RR pre23k-GFP
7 trypsin treated lane 6
The molecular weight markers are 45 kDa, 30 kDa and 20.1 kDa.

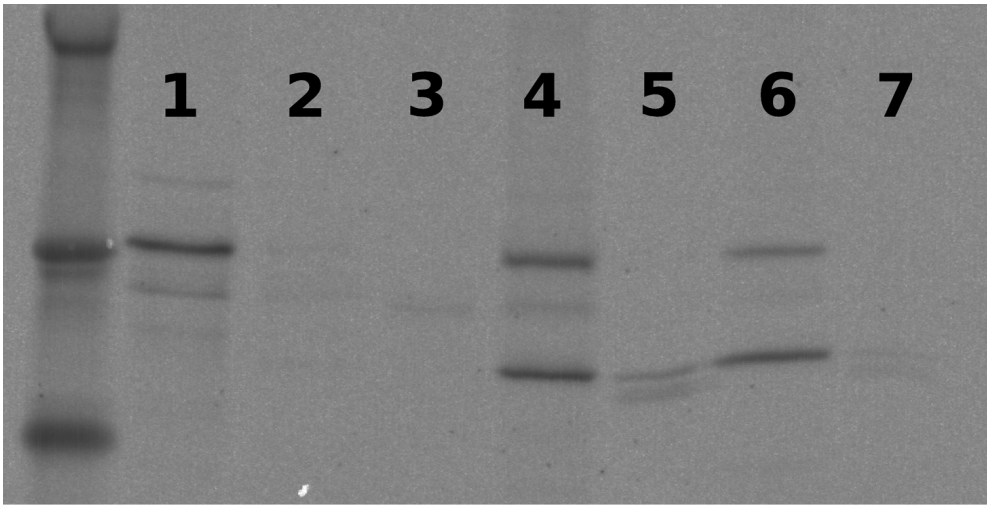

Figure 6.3: Thylakoid import of all variants of preDmsA-YFP. A comparison of the KK preDmsA-YFP mutant after thylakoid import (lane 2), transport-incompetent due to abolition of the conserved twin-arginine motif, with RR preDmsA-YFP after thylakoid import shows a putative mature sized protein (lane 7). Purified recombinant RR preDmsA-YFP was used to compete with *in vitro* translated preDmsA-YFP and a comparison of lanes 7 and 9 shows some evidence of competition. A similar result is seen for RR N-Strep-DmsA-YFP in lanes 17 and 19.
1-10 preDmsA-YFP
11-20 N-Strep-preDmsA-YFP
1 KK preDmsA-YFP translation
2 thylakoid import of KK preDmsA-YFP
3 trypsin treated lane 2
4 thylakoid import of KK preDmsA-YFP competed with recombinant protein
5 trypsin treated lane 4
6 RR preDmsA-YFP translation
7 thylakoid import of RR preDmsA-YFP
8 trypsin treated lane 7
9 thylakoid import of RR preDmsA-YFP competed with recombinant protein
10 trypsin treated lane 9
11 KK N-Strep-preDmsA-YFP translation
12 thylakoid import of KK N-Strep-preDmsA-YFP
13 trypsin treated lane 12
14 thylakoid import of KK N-Strep-preDmsA-YFP competed with recombinant protein
15 trypsin treated lane 14
16 RR N-Strep-preDmsA-YFP translation
17 thylakoid import of RR N-Strep-preDmsA-YFP
18 trypsin treated lane 17
19 thylakoid import of RR N-Strep-preDmsA-YFP competed with recombinant protein
10 trypsin treated lane 19
The molecular weight marker is 30 kDa.

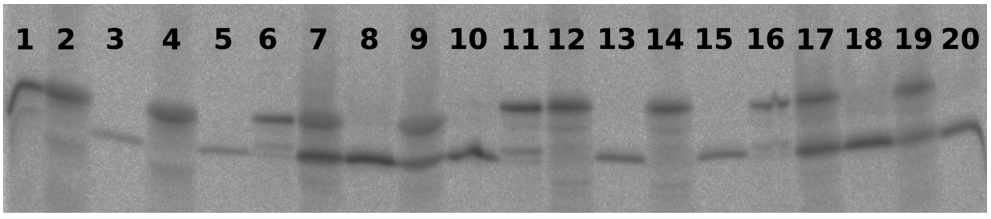

Figure 6.4: Chloroplast import of KK/RR pre23k-GFP. The putative Tat substrate RR pre23k-GFP is seen to be efficiently imported (lanes 11 and 12) so N-terminal and C-terminal Strep-tag II purification tags are added in the expectation of purifying larger amounts of this protein.
1 KK pre23k-GFP translation
2 chloroplast fraction of KK pre23k-GFP import
3 thermolysin treated lane 2
4 stromal fraction of KK pre23k-GFP import
5 thylakoid fraction of KK pre23k-GFP import
6 trypsin treated lane 5
7 RR pre23k-GFP translation
8 chloroplast fraction of RR pre23k-GFP import
9 thermolysin treated lane 8
10 stromal fraction of RR pre23k-GFP import
11 thylakoid fraction of RR pre23k-GFP import
12 trypsin treated lane 11
The molecular weight markers are 45 kDa, 30 kDa and 20.1 kDa.

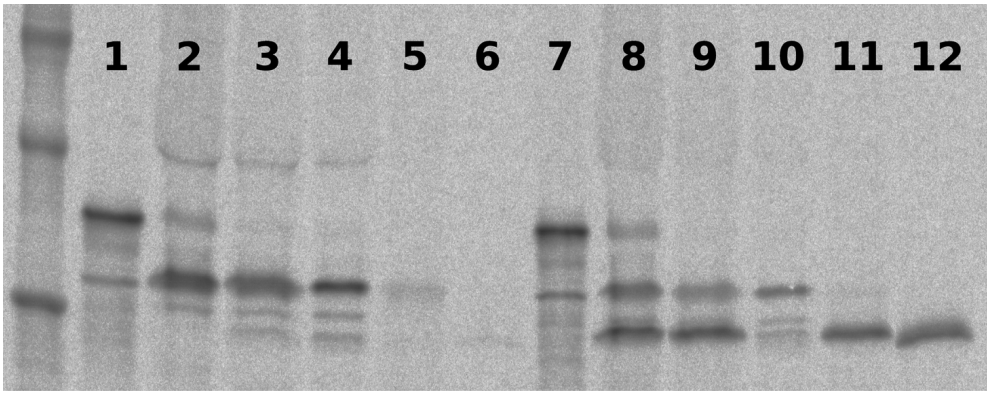

Figure 6.5: Chloroplast import of RR/KK N-Strep-pre23k-GFP. Unfortunately, the addition of an N-terminal Strep-tag II causes severely reduced efficiency of import of RR N-Strep-pre23k-GFP (lane 6). Comparing the intensity of molecular weight marker bands with the previous figure, it can be seen the reduced efficiency is likely to be real and not a result of a difference in exposure.
1 RR N-Strep-pre23k-GFP translation
2 chloroplast fraction of RR N-Strep-pre23k-GFP import
3 thermolysin treated lane 2
4 stromal fraction of RR N-Strep-pre23k-GFP import
5 thylakoid fraction of RR N-Strep-pre23k-GFP import
6 trypsin treated lane 5
7 KK N-Strep-pre23k-GFP translation
8 chloroplast fraction of KK N-Strep-pre23k-GFP import
9 thermolysin treated lane 8
10 stromal fraction of KK N-Strep-pre23k-GFP import
11 thylakoid fraction of KK N-Strep-pre23k-GFP import
12 trypsin treated lane 11
The molecular weight markers are 30 kDa and 20.1 kDa.

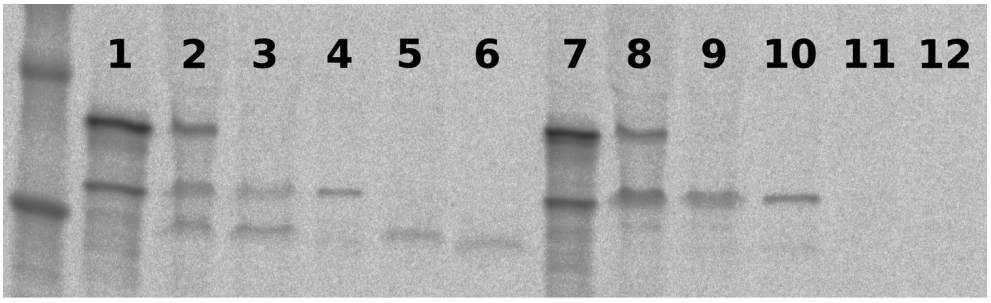

Figure 6.6: Chloroplast import of KK/RR C-Strep-pre23k-GFP. The C-terminal Strep-tag II interferes less with the efficiency of import into the chloroplast (lane 9) and further into the thylakoid lumen (lane 12) but a C-terminal tag is less suitable for protein purification as it will cause unwanted mature-sized protein to be purified in addition to the desired preprotein.

1 KK C-Strep-pre23k-GFP translation
2 chloroplast fraction of KK C-Strep-pre23k-GFP import
3 thermolysin treated lane 2
4 stromal fraction of KK C-Strep-pre23k-GFP import
5 thylakoid fraction of KK C-Strep-pre23k-GFP import
6 trypsin treated lane 5
7 RR C-Strep-pre23k-GFP translation
8 chloroplast fraction of RR C-Strep-pre23k-GFP import
9 thermolysin treated lane 8
10 stromal fraction of RR C-Strep-pre23k-GFP import
11 thylakoid fraction of RR C-Strep-pre23k-GFP import
12 trypsin treated lane 11

The molecular weight markers are 30 kDa and 20.1 kDa.

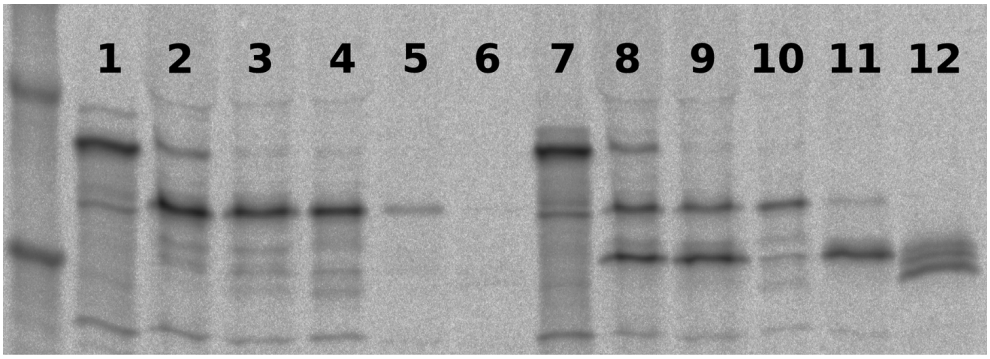

Chapter 7

Discussion and Conclusion

Chloroplast protein targeting is a field of research that relies very much on biochemical methods which give a good idea of the mechanism and later stages of the targeting process. Biochemical methods analyze many thousands of chloroplasts in aggregate in order to arrive at a single result so it is difficult to get an idea of the variability between chloroplasts much less understand what happens in different parts of the same chloroplast.

The work presented addresses the early bulk behaviour of the substrate proteins targeted to the chloroplast twin-arginine translocation pathway using a technique from fluoresence microscopy in order to make measurements at the level of individual chloroplasts. This early bulk behaviour is one of the major unknown stages between protein synthesis and arrival at

the protein's functional destination. This spatial investigation of proteins within the chloroplast is an important addition to knowledge about the internal structure of the chloroplast which derives in the main from a focus on the photosynthetic apparatus of the chloroplast whereas we study instead the protein targeting apparatus.

We analyzed fluoresence loss in photobleaching (FLIP) of fluoresent substrates within the chloroplast in order to give some quantification of how the Tat signal peptide affects the bulk movement. The difficulty of using photobleaching methods and temporal imaging within chloroplasts is severe and close to the limit of what it is possible to image: it can only be hoped that technology will improve to allow better analysis of these small specimens. Greater spatial detail would be of benefit to our understanding of the early stages chloroplast protein targeting: taking more point measurements in two dimensions to give higher resolution images would require a higher rate of image acquisition than is currently practial. High resolution measurements in three spatial dimensions would give us an even better idea of the interaction between the bulk substrate protein and the internal chloroplast structure with a corresponding increase in the difficulty of analysis. Our analysis was limited by the length of time that we could image for as photobleaching was inherent in observation so the highest signal to noise ratio is expected near the beginning of imaging a chloroplast. Related to this is that the total number of image series acquired places a limit on the length of time that can be spent on a single chloroplast. The ability to image multiple chloroplasts in parallel in an

automated way would allow more data to be gathered and more quickly although the effort to establish this level of automation can only be justified as part of a wider strategy for biological imaging.

Photobleaching analyses reported in the literature often give little emphasis to the variability between specimens and measurements so we hope that the inclusion of concisely presented raw images gives the reader a good idea of the variability in the appearance of chloroplasts and highlights the very good reproducibility of whole-chloroplast measurements as shown in the charts and histograms. The data acquired lead naturally to a more indepth analysis to understand what can and cannot be concluded from the data. The novelty of our approach leads us to be cautious in the conclusions that we draw so the modelling and simulation was very important in capturing rigorously an approximation of our experimental system and comparing our assumptions in the model with experimental data.

A significant simplification in the modelling was the assumption that the chloroplast has an intricate internal structure but nevertheless admits parameters that are suitable for describing the movement of our protein in different parts of the chloroplast. The high mobility of substrates necessitated a high rate of image acquisition and did not allow us to simultaneously monitor the photosynthetic pigments of the thylakoid membrane which could have facilitated an explicit treatment of the internal structure.

The single-species modelling and simulation allowed us to capture the

correct orders of magnitude reported for stromal and integral membrane proteins. The multi-species modelling and simulation depletion graphs show we can capture the basic form of the experimental depletion graphs and we were further able to capture an approximation to the rise at the conclusion of spot bleaching when there is fluorescence recovery from outside the focal slice.

The limitations of this two spatial dimensional modelling, without explicitly accounting for the complex nature of the chloroplast internal structure, is shown by the graphs and histograms, figures 3.11 and 3.19, correcting for photobleaching which resemble the experimental counterpart, figure 5.13, without capturing the proper shapes and magnitudes. The inhomogenous diffusion simulation showed one way of approximating the persisting structures and distributions which are made visible but the advancement of modern spatial modelling and simulation suggests it is more appropriate to work towards more detailed three dimensional protein targeting data rather than refining parameters in reduced models.

7.1 Conclusion

The soluble chimeric proteins TP-GFP, pre23kΔTPP-GFP and pre23k-GFP are imported into the chloroplast and mobile in the stroma. The lower spot bleaching rate of pre23kΔTPP-GFP compared to the mature size GFP in the

stroma, after import of TP-GFP and cleavage of the transit peptide, shows reduced mobility caused by the Tat signal peptide and indicates an interaction with the thylakoid membranes. The depletion profiles for the integral membrane protein chimera Hcf106-GFP are striking as the loss in fluorescence is account for almost entirely by observation photobleaching and very little is due to spot photobleaching which indicates highly restricted mobility. Taken together, our data suggest a Tat substrate interaction with the thylakoid membrane that is transient rather than a strong-binding association. The Tat substrate is more likely to bind either directly to the Tat translocase or to the thylakoid membrane nearby before translocation as evidenced by the mobility of all the soluble chimeras rather than diffusion laterally on the thylakoid membrane which would show depletion profiles closer to that of the integral membrane construct.

The implementation of the partition of unity method presented in this thesis was motivated by the need to prototype parallel, high performance components to improve the walltime and refinement levels achievable by our research group's Generic Discretization Framework (GDF) as developed by Martin Eigel and Erwin George (Eigel, 2008; Eigel et al., 2009). It is hoped that the advances and performance improvements detailed earlier will be made available to GDF in the future. In brief, the improvements are parallel execution, redundancy reduction in assembly, integrations calculated by matrix-vector operations, and convergence testing in a single execution. These improvements allow calculation with up to 10 levels of complete refinement, a four level improvement (a factor of $4^4 = 256$ more

patches) on GDF's 6 levels of complete refinement. The parallel implementation presented in this thesis is able to solve a problem with in excess of three million degrees of freedom, a 30 times improvement on GDF's under 100 000 degrees of freedom. (Eigel et al., 2009)

Our work with PUM was carried out in very much the way that we expect other researchers interested in mesh-free methods would proceed. We are three or four levels of spatial refinement below the work carried out by Griebel and Schweitzer but this is to be expected due to their existing expertise in parallel computation and numerical spatial methods. Their prowess was also demonstrated by their implementation of a multilevel solver in comparison to our use of PETSc. Our research emphasis has been different, dispensing with particles being one notable result, and modern computer resources have allowed us to tackle large problems.

This research represents the first tentative steps in modern spatio-temporal analysis in molecular biology. The tools to observe the distribution of a protein and its redistribution have only recently become available and the computational resources for PUM are emerging in the same way that the finite difference method and finite element method had to wait for increasing computer power in the course of their development.

During the course of this research, many different techniques have been brought together to study the spatio-temporal dynamics of Tat substrates in the chloroplast and the achievements and contributions to knowledge

Table 7.1: Achievements and contributions to knowledge.

1. A robust quantitative FLIP procedure is presented that allows the gathering of **spatio-temporal** data series.
2. We show **rare *in vivo* evidence** to allow a nuanced assessment of the conclusion drawn from *in vitro* biochemical data that the signal peptide affects the behaviour and binding of the Tat substrate.
3. A mesh-free method, the Partition of Unity Method has been implemented in a particle-free form that is able to make **direct use of experimental data**.
4. We have presented **implementational optimizations and experience** that will be of interest to other researchers considering PUM or other mesh-free methods.
5. The computations presented show an improvement of walltime achieved by our group from **hours down to minutes** which better shows the potential for PUM.

are summarized in table 1.1. Various compromises have had to be made during the course of the research and these should be considered in light of emerging technologies for future spatio-temporal modelling and simulation. The use of light microscopy to observe dyanmic processes meant that we were unable to resolve the thylakoid membrane in sufficient detail to capture its influence in simulation although we have suggested an alternative way of capturing the inhomogeneity. An *in vitro* import assay of recombinant fluorescent protein targeted to the Tat pathway was not available for studying the translocation process itself although poor resolution of the thylakoid membrane would have been as much an obstruction as the lack of such an assay. Membrane processes have consequently not been studied in the simulation and analysis.

Part III

Back Matter

Appendix A

Basic Results

Product rule for divergence Fix a dimension $d = 1, 2, 3$; let v be a scalar function, and let $w = (w_1, \ldots, w_d)$ be a vector function. The product rule for the divergence $\nabla\cdot$ is

$$\begin{aligned}\nabla \cdot (vw) &= \sum_{i=1}^{d} \frac{\partial (vw_i)}{\partial x_i} \\ &= \sum_{i=1}^{d} \left(\frac{\partial v}{\partial x_i} w_i + v \frac{\partial w_i}{\partial x_i} \right) \\ &= (\nabla v) \cdot w + v \nabla \cdot w\end{aligned}$$

Integration by parts Let u be a scalar function, D be a $d \times d$ matrix and set $w = D\nabla u$ (a vector function) so that we get

$$\nabla \cdot (vD\nabla u) = (\nabla v) \cdot (D\nabla u) + v\nabla.(D\nabla u)$$

so

$$\int_\Omega \nabla \cdot (vD\nabla u)\, \mathrm{d}\Omega = \int_\Omega (\nabla v) \cdot (D\nabla u)\, \mathrm{d}\Omega + \int_\Omega v\nabla \cdot (D\nabla u)\, \mathrm{d}\Omega \qquad \text{(A.1)}$$

Divergence Theorem

$$\int_\Omega \nabla.(vD\nabla u)\, \mathrm{d}\Omega = \int_{\partial\Omega} v(D\nabla u).n\, \mathrm{d}\Omega$$

Where $n(x)$ is the unit normal vector pointing out of Ω at the point x on the boundary of Ω.

Appendix B

Glossary

B.1 Latin Abbreviations and Phrases

a.m. Abbreviation for Latin phrase *"ante meridiem"*, meaning "before noon" (compare with 'p.m.').

a posteriori Latin phrase meaning "what comes later".

a priori Latin phrase meaning "what comes before".

Arte et Labore "By Art and by Labour", Latin motto of the town of Blackburn.

cf. Abbreviation for Latin verb *'confer'* to mean compare (note there is no fullstop between the two letters).

cum laude Latin phrase to mean "with praise".

Disce Prodesse "Learn to be of Service", Latin motto of Queen Elizabeth's Grammar School (established 1509), Blackburn, UK.

e.g. Abbreviation for Latin phrase *"exempli gratia"*, meaning "for example".

et al. Abbreviation for Latin phrase *"et alii"*, meaning "and others" (note there is no fullstop after *'et'*).

etc. Abbreviation for Latin phrase *"et cetera"*, meaning "and the rest" or "and so on".

i.e. Abbreviation for Latin phrase *"id est"*, meaning "that is" or "which is to say"

in vitro Latin phrase; literally "in glass" to mean, for example, in a test tube.

in vivo Latin phrase to denote within the living organism.

magna cum laude Latin phrase meaning "with great praise".

Mens agitat molem "Mind over matter", Latin motto of the University of Warwick (established 1965).

N.B. Abbreviation for Latin phrase *"nota bene"*, meaning "note well!".

p.m. Abbreviation for Latin phrase *"post meridiem"*, meaning "after noon".

P.S. Abbreviation for Latin phrase *"post scriptum"*, meaning "after what has been written".

Q.E.D. Abbreviation for Latin phrase *"quod erat demonstrandum"*, meaning "which was to be proved".

q.v. Abbreviation for Latin phrase *"quod vide"* ("which see") cross-referencing to another part of the book or article.

summa cum laude Latin phrase meaning "with highest praise".

viva Common abbreviation for a *viva voce* examination, the process of testing by oral questioning of a candidate for a degree. (See also "*viva voce*")

viva voce Latin phrase meaning "by live voice".

viz. Abbreviation for Latin word *"videlicit"*, meaning "as befitting" or "as is pleasing to".

B.2 Biological Abbreviations and Glossary

The glossary contains biological terms; explanations of the mathematical notation and terminology is provided in a separate chapter.

ΔpH The proton gradient across a membrane.

$\Delta\psi$ The electrical potential component of the proton motive force.

35S promoter See CaMV 35S promoter.

Å Angstrom – denotes the length 10^{-10} m.

ADP Adenosine Diphosphate.

Agarose Polysaccharide extracted from seaweed.

AMP Adensosine Monophosphate.

Ampicillin An antibiotic.

APS Ammonium Persulphate.

ATP Adenosine Triphosphate.

Beta vulgaris The beetroot plant.

BN-PAGE Blue native polyacrylamide gel electrophoresis.

BSA Bovine Serum Albumin

CaMV Cauliflower mosaic virus.

CaMV 35S promoter Promoter of the 35S RNA of CaMV (see also CaMV).

Chloroplast Organelle responsible for photosynthesis in plant cells (as a particular example, we isolate chloroplast from the leaves of young "pea plants").

Confocal Term referring to the exclusion of light from unwanted planes of the sample and ensuring light arriving at the detector originates from a small region localised around the point of interest.

Covalent Bond Molecular orbital of valence electrons shared between two atoms allowing the associated nuclei to remain associated.

cpTatC Chloroplast TatC homologue.

Dalton The atomic mass unit.

DH5α Strain of *Escherichia coli*.

DmsA Catalytic subunit of DMSO reductase.

DMSO Dimethyl Sulphoxide.

DNase Deoxyribonuclease.

E. coli Abbreviation for *Escherichia coli*.

FACS Fluorescence-Activated Cell Sorting.

FLIP Fluorescence Loss In Photobleaching.

FRAP Fluorescence Recovery After Photobleaching.

GFP Green Fluorescent Protein. (*A. victoria*: 238 amino acids, 714 base pairs).

GFPmut3* Variant of GFP (238 amino acids, 714 base pairs).

Hcf106 High-chlorophyll fluorescence protein. TatB homologue.

HEPES The organic chemical buffer 4-2-hydroxyethyl-1-piperazineethanesulfonic acid.

HM HEPES Magnesium buffer (see also HEPES).

HS HEPES Sorbitol buffer (see also HEPES).

Integral Membrane Protein

Laser Acronym for "Light Amplification by Stimulated Emission of Radiation" but accepted as a word in its own right.

LB Growth medium.

M Symbol for the unit of concentration, Molar (see also Molar).

Molar One mole per litre.

Membrane Protein

mRNA Messenger Ribonucleic Acid (see also RNA).

PAGE Polyacrylamide Gel Electrophoresis.

pH Potential of hydrogen; defined to be $-\log_{10}[H^+]$, where $[H^+]$ is the concentration of hydrogen ions in units of Molar.

Pisum sativum The garden pea plant.

RCF Relative centrifugal force.

RNA Ribonucleic acid.

rpm Revolutions per minute.

Rubisco Ribulose-1,5-bisphosphate carboxylase/oxygenase.

RuBP Ribulose-1,5-bisphosphate.

SDS Sodium dodecyl sulphate - anionic detergent which can bind to the backbone of polypeptides to maintain them in an unfolded conformation, and confers a negative charge roughly proportional to the length of the polypeptide chain

SDS-PAGE Sodium dodecyl sulphate polyacrylamide gel electrophoresis (see also SDS, Polyacrylamide, and Electrophoresis).

Sepharose Gel filtration media based on agarose.

SI Le Système International d'Unités (French) - International System of Units.

Surfactant Chemical capable of lowering the surface tension of a liquid in which the chemical is dissolved.

Svedberg unit (S) Non-SI unit named for Swedish chemist Theodor Svedberg (1884-1971). One Svedberg is 10^{-13} seconds. (see also SI)

tat The operon of *E. coli* coding for the gene products necessary for the Twin-Arginine Translocation pathway.

Tat Twin-Arginine Translocation.

tatA Gene for the TatA gene product.

TatA An integral membrane component of the Tat pathway in *Escherichia coli*.

TEMED Tetramethyldiamine.

Tha4 Thylakoid assembly protein. TatA homologue.

Thylakoid Complicated arrangements of folded membranes, in either plant chloroplasts or photosynthesizing uni-cellular organisms, allowing electron transfer reactions to occur.

Translation Term used to refer to the protein produced by cell-free methods from mRNA.

Transmembrane Adjective meaning spanning the membrane of discussion (for example, a 'transmembrane protein').

Tris Tris(hydroxymethyl)aminemethane.

tRNA Transfer RNA (also see RNA).

Trypsin A protease.

UV Ultra-violet electromagnetic waves.

YFP Yellow fluorescent protein

B.3 Mathematical and Computational

:= Notation specifying the left-hand side is defined to be equal to the right-hand side.

$|\cdot|$ Euclidean length.

$\|\cdot\|$ A norm.

α_c The cover factor.

φ_i The i-th partition of unity function.

Φ_i The i-th PUM basis function for some PUM function space.

Ψ_i The i-th PUM basis function for some PUM function space; especially to denote a test function.

ABI Application Binary Interface.

ANOVA Analysis of variance.

API Application Programming Interface.

Argument Dependent Lookup A function that is not found during normal lookup will be subject to an expanded lookup according to function's argument types.

Banach Space A normed vector space which is complete.

Barton-Nackman Trick C++ programming idiom where a class template has in-class friend function definitions that produce non-template, non-member functions. Named for John Barton and Lee Nackman.

BLAS Basic Linear Algebra Subprograms, a numerical software library written in Fortran 77.

C Programming language developed by Dennis Ritchie at Bell Telephone Laboratories.

C++ Programming language based on C and created by Bjarne Stroustrup.

CLI Command Line Interface.

CPU Central Processing Unit.

Curiously Recurring Template Pattern (CRTP) C++ programming idiom of a class A deriving from a class template instantiation with A as one of the template arguments. Coined by Jim Coplien.

Design Patterns Software engineering strategies that may be used to solve many different problems.

Divergence The divergence of a vector function $u = (u_1, \ldots, u_d)$ is $\nabla \cdot u := \partial_{x_1} u_1 + \ldots + \partial_{x_d} u_d$.

GCC GNU Compiler Collection.

GNU Recursive acronym for "GNU's Not Unix".

Gradient The gradient of a scalar function f is $\nabla f := (\partial_{x_1} f, \ldots, \partial_{x_d} f)$.

FEM Finite Element Method, a class of methods for the numerical solution of PDEs.

Fortran Programming language originally developed by IBM with language support for matrices and vectors: popular for numerical applications.

Hilbert Space An inner product space which is complete with respect to the norm defined by the inner product.

Koenig Lookup Named for Andrew Koenig - see Argument Dependent Lookup.

LAPACK Linear Algebra Package, a numerical software library written in Fortran 77.

Linux Collaboratively developed computer kernel created by Linus Torvalds in 1991.

M A number $M \in \mathbb{N}$ used to denote the number of test functions.

Mathworks Logo The logo for Mathworks, the owner of MATLAB, is an approximation of the first eigenfunction of the wave equation in an L-shaped domain.

Mesh-free Adjective meaning a finite element mesh is not used.

MPI Message Passing Interface, an API for distributed memory parallelization.

$\mathbb{N}$ The set of natural numbers (does not include zero).

N A number $N \in \mathbb{N}$ used to denote the number of trial functions.

Non-Virtual Interface (NVI)

OpenMP Open Multi-Processing, an API for shared memory parallelization.

p The local basis order.

PDE Partial Differential Equation.

PETSc Portable, Extensible Toolkit for Scientific Computation; library developed at the Argonne National Laboratory, Argonne, Illinois.

PUM The Partition of Unity Method; a mesh-free method for the numerical solution of PDEs.

$\mathbf{q}$ In bold, the vector of coefficients q_i, otherwise the quadrature order.

Q_{ij} Coefficient of the PUM test function which is the product of the i-th partition of unity function and the j-th local function.

q_i Coefficient of i-th PUM test function in the single sum representation.

$\mathbb{R}$ The set of real numbers.

Resource Allocation Is Initialization (RAII)

STL The C++ Standard Template Library.

SUNDIALS Suite of Nonlinear and Differential/Algebraic Equation Solvers; library developed at the Lawrence Livermore National Laboratory, Livermore, California, USA.

Template Metaprogramming

Test Functions Functions used to generate a linear subspace of functions used to minimize the error of an approximation: the error is made orthogonal to the test functions.

Trial Functions Functions used to generate a linear subspace of functions in which an approximation is sought to the solution of a problem of interest.

Undefined Behaviour The outcome of the statement(s) in the source code is not specified by the programming language standard appropriate to the source code.

Upwind Scheme Discretization approach that takes into account the asymmetric evolution of a function in time due to some convection term: contrast with a symmetric approximation in space.

Bibliography

Robert A. Adams. *Sobolev Spaces.*, volume 65 of *Pure and applied mathematics; a series of monographs and textbooks*. Academic Press, **1975**. 41, 42

Meriem Alami, **Iris Lüke**, **Sandra Deitermann**, **Gottfried Eisner**, **Hans-Georg Koch**, **Joseph Brunner**, and **Matthias Müller**. Differential interactions between a twin-arginine signal peptide and its translocase in *Escherichia coli*. *Mol Cell*, **12**(4):937–946, **2003**. 13

Stuart C H Allen, **Claire M L Barrett**, **Nicola Ray**, and **Colin Robinson**. Essential cytoplasmic domains in the *Escherichia coli* TatC protein. *J Biol Chem*, **277**(12):10362–10366, **2002**. doi:10.1074/jbc.M109135200. 9

Anton Arkhipov, **Jana Hüve**, **Martin Kahms**, **Reiner Peters**, and **Klaus Schulten**. Continuous fluorescence microphotolysis and correlation spectroscopy using 4Pi microscopy. *Biophys J*, **93**(11):4006–4017, **2007**. doi:10.1529/biophysj.107.107805. 29

D. Axelrod, **D. E. Koppel**, **J. Schlessinger**, **E. Elson**, and **W. W. Webb**. Mobility measurement by analysis of fluorescence photobleaching recovery kinetics. *Biophys J*, **16**(9):1055–1069, **1976**. 27, 28

I. Babuška, **U. Banerjee**, and **J. E. Osborn**. Meshless and generalized finite element methods: a survey of some major results. In **Michael Griebel** and **Marc A. Schweitzer**, editors, *Meshfree Methods for Partial Differential Equations*, volume 26 of *Lecture Notes in Computational Science and Engineering*, pages 1–20. Springer, **2002**. 116

I. Babuška and **J. M. Melenk**. The partition of unity method. *Int J Numer Meth Eng*, **40**:727–758, **1997**. 30, 32, 38, 40

Claire M. L. Barrett, **Nicola Ray**, **Joanne D. Thomas**, **Colin Robinson**, and **Albert Bolhuis**. Quantitative export of a reporter protein, GFP, by the twin-arginine translocation pathway in *Escherichia coli*. *Biochem Biophys Res Commun*, **304**(2):279–284, **2003**. 67

Joël Beaudouin, **Felipe Mora-Bermúdez**, **Thorsten Klee**, **Nathalie Daigle**, and **Jan Ellenberg**. Dissecting the contribution of diffusion and interac-

tions to the mobility of nuclear proteins. *Biophys J*, **90**(6):1878–1894, **2006**. doi:10.1529/biophysj.105.071241. 36

T. Belytschko, **Y. Krongauz**, **D. Organ**, **M. Fleming**, and **P. Krysl**. Meshless methods: an overview and recent developments. *Comput Methods Appl Engrg*, **139**:3–47, **1996**. 30, 31

T. Belytschko, **Y. Y. Lu**, and **L. Gu**. Element-free Galerkin methods. *Int J Numer Meth Eng*, **37**:229–256, **1994**. 32, 37

B. C. Berks. A common export pathway for proteins binding complex redox cofactors? *Mol Microbiol*, **22**(3):393–404, **1996**. 6

Ben C Berks, **Tracy Palmer**, and **Frank Sargent**. Protein targeting by the bacterial twin-arginine translocation (Tat) pathway. *Curr Opin Microbiol*, **8**(2):174–181, **2005**. doi:10.1016/j.mib.2005.02.010. 14

Natascha Blaudeck, **Peter Kreutzenbeck**, **Matthias Müller**, **Georg A Sprenger**, and **Roland Freudl**. Isolation and characterization of bifunctional *Escherichia coli* TatA mutant proteins that allow efficient tat-dependent protein translocation in the absence of TatB. *J Biol Chem*, **280**(5):3426–3432, **2005**. doi:10.1074/jbc.M411210200. 18

E. G. Bogsch, **F. Sargent**, **N. R. Stanley**, **B. C. Berks**, **C. Robinson**, and **T. Palmer**. An essential component of a novel bacterial protein export system with homologues in plastids and mitochondria. *J Biol Chem*, **273**(29):18003–18006, **1998**. 7

A. Bolhuis, **E. G. Bogsch**, and **C. Robinson**. Subunit interactions in the twin-arginine translocase complex of *Escherichia coli*. *FEBS Lett*, **472**(1):88–92, **2000**. 13

A. Bolhuis, **J. E. Mathers**, **J. D. Thomas**, **C. M. Barrett**, and **C. Robinson**. TatB and TatC form a functional and structural unit of the twin-arginine translocase from *Escherichia coli*. *J Biol Chem*, **276**(23):20213–20219, **2001**. doi:10.1074/jbc.M100682200. 13, 14

James H. Bramble and **Miloš Zlámal**. Triangular elements in the finite element method. *Mathematics of Computation*, **24**(112):809–820, **1970**. 31

Haïm Brezis. Partial differential equations in the 20th century. *Advances in Mathematics*, **135**:76–144, **1998**. 41

S. Brink, **E. G. Bogsch**, **W. R. Edwards**, **P. J. Hynds**, and **C. Robinson**. Targeting of thylakoid proteins by the ΔpH-driven twin-arginine translocation pathway requires a specific signal in the hydrophobic domain in conjunction with the twin-arginine motif. *FEBS Lett*, **434**(3):425–430, **1998**. 6

Thomas Brüser and **Carsten Sanders**. An alternative model of the twin arginine translocation system. *Microbiol Res*, **158**(1):7–17, **2003**. 15

Grant Buchanan, **Erik de Leeuw**, **Nicola R Stanley**, **Margaret Wexler**, **Ben C Berks**, **Frank Sargent**, and **Tracy Palmer**. Functional complexity of

the twin-arginine translocase TatC component revealed by site-directed mutagenesis. *Mol Microbiol*, **43**(6):1457–1470, **2002**. 8

A. Carpinteri, **G. Ferro**, and **G. Ventura**. The partition of unity quadrature in meshless methods. *Int J Numer Meth Engng*, **54**:987–1006, **2002**. doi: 10.1002/nme.455. 100

A. M. Chaddock, **A. Mant**, **I. Karnauchov**, **S. Brink**, **R. G. Herrmann**, **R. B. Klösgen**, and **C. Robinson**. A new type of signal peptide: central role of a twin-arginine motif in transfer signals for the ΔpH-dependent thylakoidal protein translocase. *EMBO J*, **14**(12):2715–2722, **1995**. 5, 6, 26

Catherine S Chan, **Marian R Zlomislic**, **D. Peter Tieleman**, and **Raymond J Turner**. The tata subunit of escherichia coli twin-arginine translocase has an n-in topology. *Biochemistry*, **46**(25):7396–7404, **2007**. doi:10.1021/bi7005288. 16

Sonya A. Clark and **Steven M. Theg**. A folded protein can be transported across the chloroplast envelope and thylakoid membranes. *Molecular Biology of the Cell*, **8**:923–934, **1997**. 9, 26

K. Cline, **W. F. Ettinger**, and **S. M. Theg**. Protein-specific energy requirements for protein transport across or into thylakoid membranes. Two lumenal proteins are transported in the absence of ATP. *J Biol Chem*, **267**(4):2688–2696, **1992**. 4, 5

K. Cline and **R. Henry**. Import and routing of nucleus-encoded chloroplast proteins. *Annu Rev Cell Dev Biol*, **12**:1–26, **1996**. doi:10.1146/annurev.cellbio.12.1.1. 3, 4

K. Cline, **R. Henry**, **C. Li**, and **J. Yuan**. Multiple pathways for protein transport into or across the thylakoid membrane. *EMBO J*, **12**(11):4105–4114, **1993**. 5

K. Cline and **H. Mori**. Thylakoid ΔpH-dependent precursor proteins bind to a cpTatC-Hcf106 complex before Tha4-dependent transport. *J Cell Biol*, **154**(4):719–729, **2001**. doi:10.1083/jcb.200105149. 13, 67

Kenneth Cline and **Michael McCaffery**. Evidence for a dynamic and transient pathway through the TAT protein transport machinery. *EMBO J*, **26**(13):3039–3049, **2007**. doi:10.1038/sj.emboj.7601759. 16

Ray W. Clough. Original formulation of the finite element method. *Finite Elements in Analysis and Design*, **7**:89–101, **1990**. 95

N. B. Cole, **C. L. Smith**, **N. Sciaky**, **M. Terasaki**, **M. Edidin**, and **J. Lippincott-Schwartz**. Diffusional mobility of Golgi proteins in membranes of living cells. *Science*, **273**(5276):797–801, **1996**. 22, 23, 27

Elena Consoli, **Roberta Croce**, **David D Dunlap**, and **Laura Finzi**. Diffusion of light-harvesting complex II in the thylakoid membranes. *EMBO Rep*, **6**(8):782–786, **2005**. doi:10.1038/sj.embor.7400464. 34

R. Courant. Variational methods for the solution of problems of equilib-

rium and vibrations. *Bull. Amer. Math. Soc.*, **49**:1–23, **1943**. 31, 45, 47

A. M. Creighton, **A. Hulford**, **A. Mant**, **D. Robinson**, and **C. Robinson**. A monomeric, tightly folded stromal intermediate on the ΔpH-dependent thylakoidal protein transport pathway. *J Biol Chem*, **270**(4):1663–1669, **1995**. 9

S. Cristóbal, **J. W. de Gier**, **H. Nielsen**, and **G. von Heijne**. Competition between Sec- and TAT-dependent protein translocation in *Escherichia coli*. *EMBO J*, **18**(11):2982–2990, **1999**. doi:10.1093/emboj/18.11.2982. 6

Carole Dabney-Smith, **Hiroki Mori**, and **Kenneth Cline**. Oligomers of Tha4 organize at the thylakoid Tat translocase during protein transport. *J Biol Chem*, **281**(9):5476–5483, **2006**. doi:10.1074/jbc.M512453200. 15, 67

M. J. Dayel, **E. F. Hom**, and **A. S. Verkman**. Diffusion of green fluorescent protein in the aqueous-phase lumen of endoplasmic reticulum. *Biophys J*, **76**(5):2843–2851, **1999**. 34

A. Delon, **Y. Usson**, **J. Derouard**, **T. Biben**, and **C. Souchier**. Continuous photobleaching in vesicles and living cells: a measure of diffusion and compartmentation. *Biophys J*, **90**(7):2548–2562, **2006**. doi:10.1529/biophysj.105.069815. 29

Alessandra di Cola, **Shaun Bailey**, and **Colin Robinson**. The thylakoid ΔpH/ΔΨ are not required for the initial stages of Tat-dependent protein transport in tobacco protoplasts. *J Biol Chem*, **280**(50):41165–41170, **2005**. doi:10.1074/jbc.M509215200. 20

Alessandra di Cola and **Colin Robinson**. Large-scale translocation reversal within the thylakoid Tat system *in vivo*. *J Cell Biol*, **171**(2):281–289, **2005**. doi:10.1083/jcb.200502067. 26, 67, 69

C. Armando Duarte. A review of some meshless methods to solve partial differential equations. Technical Report 95-06, Texas Institute for Computational and Applied Mathematics (TICAM), The University of Texas at Austin, **1995**. 31

C. Armando Duarte and **J. T. Oden**. *Hp* clouds – a meshless method to solve boundary-value problems. Technical Report 95-05, Texas Institute for Computational and Applied Mathematics (TICAM), The University of Texas at Austin, **1995**. 32

C. Armando Duarte and **J. Tinsley Oden**. *H-p* clouds – an *h-p* meshless method. *Numer. Methods Partial Diff. Equations*, **12**(6):673–705, **1996**. doi:DOI:10.1002/(SICI)1098-2426(199611)12:6⟨673::AID-NUM3⟩3.0.CO;2-P. 37

Alexandra Dubini and **Frank Sargent**. Assembly of Tat-dependent [NiFe] hydrogenases: identification of precursor-binding accessory proteins. *FEBS Lett*, **549**(1-3):141–146, **2003**. 11

Yu V. Egorov and **M. A. Shubin**. *Foundations of the Classical Theory of*

Partial Differential Equations. Springer-Verlag, second edition, **1998**. ISBN 3-540-63825-3. 41

M. Eigel, **E. George**, and **M. Kirkilionis**. A mesh-free partition of unity method for diffusion equations on complex domains. *IMA Journal of Numerical Analysis*, **2009**. doi:10.1093/imanum/drn053. 116, 178, 179

Martin Eigel. *An Adaptive Meshfree Method for Reaction-Diffusion Processes on Complex Domains. Applications in Cell Biology.* Ph.D. thesis, The University of Warwick, **2008**. 178

M. B. Elowitz, **M. G. Surette**, **P. E. Wolf**, **J. B. Stock**, and **S. Leibler**. Protein mobility in the cytoplasm of *Escherichia coli*. *J Bacteriol*, **181**(1):197–203, **1999**. 34

T. Endo, **M. Kawakami**, **A. Goto**, **T. America**, **P. Weisbeek**, and **M. Nakai**. Chloroplast protein import. chloroplast envelopes and thylakoids have different abilities to unfold proteins. *Eur J Biochem*, **225**(1):403–409, **1994**. 10

E. Endress, **S. Weigelt**, **G. Reents**, and **T. M. Bayerl**. Derivation of a closed form analytical expression for fluorescence recovery after photo bleaching in the case of continuous bleaching during read out. *Eur Phys J E Soft Matter*, **16**(1):81–87, **2005**. doi:10.1140/epje/e2005-00010-5. 29, 35

T. J. Feder, **I. Brust-Mascher**, **J. P. Slattery**, **B. Baird**, and **W. W. Webb**. Constrained diffusion or immobile fraction on cell surfaces: a new interpretation. *Biophys J*, **70**(6):2767–2773, **1996**. 28

V. Fincher, **M. McCaffery**, and **K. Cline**. Evidence for a loop mechanism of protein transport by the thylakoid ΔpH pathway. *FEBS Lett*, **423**(1):66–70, **1998**. 15

U. I. Flügge and **G. Hinz**. Energy dependence of protein translocation into chloroplasts. *Eur J Biochem*, **160**(3):563–570, **1986**. 4

Thomas-Peter Fries and **Hermann-Georg Matthies**. Classification and overview of meshfree methods. Technical Report 2003-3, Institute of Scientific Computing, Technical University Braunschweig, **2004**. 31

Thomas-Peter Fries and **Hermann Georg Matthies**. Mesh-free Petrov-Galerkin methods for the incompressible Navier-Stokes equations. In *Meshfree Methods for Partial Differential Equations II*, volume 43, pages 39–54. Springer, **2005**. 46

L. D. Frye and **M. Edidin**. The rapid intermixing of cell surface antigens after formation of mouse-human heterokaryons. *J Cell Sci*, **7**(2):319–335, **1970**. 21, 27

Gadella, **van der Krogt GN**, and **Bisseling**. GFP-based FRET microscopy in living plant cells. *Trends Plant Sci*, **4**(7):287–291, **1999**. 23

R. A. Gingold and **J. J. Monaghan**. Smoothed particle hydrodynamics: theory and application to non-spherical stars. *Mon. Not. R. astr. Soc.*,

181:375–389, **1977**. 32, 37

Ulrich Gohlke, **Lee Pullan**, **Christopher A McDevitt**, **Ida Porcelli**, **Erik de Leeuw**, **Tracy Palmer**, **Helen R Saibil**, and **Ben C Berks**. The TatA component of the twin-arginine protein transport system forms channel complexes of variable diameter. *Proc Natl Acad Sci U S A*, **102**(30):10482–10486, **2005**. doi:10.1073/pnas.0503558102. 15

Kamila Gouffi, **Claire-Lise Santini**, and **Long-Fei Wu**. Topology determination and functional analysis of the *Escherichia coli* TatC protein. *FEBS Lett*, **525**(1-3):65–70, **2002**. 16

M. Griebel, **P. Oswald**, and **M. A. Schweitzer**. A particle-partition of unity method – Part VI: a *p*-robust multilevel solver. In **M. Griebel** and **M. A. Schweitzer**, editors, *Meshfree Methods for Partial Differential Equations II.*, volume 43 of *Lecture Notes in Computational Science and Engineering*, pages 71–43. Springer, **2005**. 39

M. Griebel and **M. A. Schweitzer**. A particle-partition of unity method for the solution of elliptic, parabolic and hyperbolic PDE. *SIAM J Sci Comp*, **22**:853–890, **2000**. 32, 39

M. Griebel and **M. A. Schweitzer**. A particle-partition of unity method – Part VII: adaptvity. In **M. Griebel** and **M. A. Schweitzer**, editors, *Meshfree Methods for Partial Differential Equations III.*, volume 57 of *Lecture Notes in Computational Science and Engineering*. Springer, **2006**. 39

Michael Griebel and **Marc Alexander Schweitzer**. A particle-partition of unity method – Part II: efficient cover construction and reliable integration. *SIAM J Sci Comp*, **23**(5):1655–1682, **2002**a. 33, 39

Michael Griebel and **Marc Alexander Schweitzer**. A particle-partition of unity method – Part III: a multilevel solver. *SIAM J Sci Comp*, **24**(2):377–407, **2002**b. 33, 39

Michael Griebel and **Marc Alexander Schweitzer**. A particle-partition of unity method – Part IV: parallelization. In **Michael Griebel** and **Marc Alexander Schweitzer**, editors, *Meshfree Methods for Partial Differential Equations.*, volume 26 of *Lecture notes in Computational Science and Engineering*, pages 161–192. Springer, **2002**c. 39, 116

Michael Griebel and **Marc Alexander Schweitzer**. A particle-partition of unity method – Part V: boundary conditions. In **S. Hildebrandt** and **H. Karcher**, editors, *Geometric analysis and nonlinear partial differential equations.*, pages 517–540. Springer, **2002**d. 39

L. M. Guzman, **D. Belin**, **M. J. Carson**, and **J. Beckwith**. Tight regulation, modulation, and high-level expression by vectors containing the arabinose PBAD promoter. *J Bacteriol*, **177**(14):4121–4130, **1995**. 163

Richard Hacker. Certification of Algorithm 112: position of point relative to polygon. *Communications of the ACM*, **5**(12):606, **1962**. 115

Guy M Hagen, **Deborah A Roess**, **Gildardo Cruz de León**, and **B. George Barisas**. High probe intensity photobleaching measurement of lateral diffusion in cell membranes. *J Fluoresc*, **15**(6):873–882, **2005**. doi:10.1007/s10895-005-0012-5. 35

Kostas Hatzixanthis, **Thomas A Clarke**, **Arthur Oubrie**, **David J Richardson**, **Raymond J Turner**, and **Frank Sargent**. Signal peptide-chaperone interactions on the twin-arginine protein transport pathway. *Proc Natl Acad Sci U S A*, **102**(24):8460–8465, **2005**. doi:10.1073/pnas.0500737102. 11

U. Haupts, **S. Maiti**, **P. Schwille**, and **W. W. Webb**. Dynamics of fluorescence fluctuations in green fluorescent protein observed by fluorescence correlation spectroscopy. *Proc Natl Acad Sci U S A*, **95**(23):13573–13578, **1998**. 23

Matthew G Hicks, **Erik de Leeuw**, **Ida Porcelli**, **Grant Buchanan**, **Ben C Berks**, and **Tracy Palmer**. The *Escherichia coli* twin-arginine translocase: conserved residues of TatA and TatB family components involved in protein transport. *FEBS Lett*, **539**(1-3):61–67, **2003**. 18

Bo Hou, **Stefan Frielingsdorf**, and **Ralf Bernd Klösgen**. Unassisted membrane insertion as the initial step in ΔpH/Tat-dependent protein transport. *J Mol Biol*, **355**(5):957–967, **2006**. doi:10.1016/j.jmb.2005.11.029. 15, 20

Chang-Deng Hu, **Yurii Chinenov**, and **Tom K Kerppola**. Visualization of interactions among bZIP and Rel family proteins in living cells using bimolecular fluorescence complementation. *Mol Cell*, **9**(4):789–798, **2002**. 24

P. J. Hynds, **D. Robinson**, and **C. Robinson**. The sec-independent twin-arginine translocation system can transport both tightly folded and malfolded proteins across the thylakoid membrane. *J Biol Chem*, **273**(52):34868–34874, **1998**. 9, 10, 11

Rachael L Jack, **Grant Buchanan**, **Alexandra Dubini**, **Kostas Hatzixanthis**, **Tracy Palmer**, and **Frank Sargent**. Coordinating assembly and export of complex bacterial proteins. *EMBO J*, **23**(20):3962–3972, **2004**. doi:10.1038/sj.emboj.7600409. 11

Paul Jarvis and **Colin Robinson**. Mechanisms of protein import and routing in chloroplasts. *Curr. Biol.*, **14**:1064–1077, **2004**. 4, 25

T. Jascur, **D. P. Goldenberg**, **D. Vestweber**, and **G. Schatz**. Sequential translocation of an artificial precursor protein across the two mitochondrial membranes. *J Biol Chem*, **267**(19):13636–13641, **1992**. 10

J. D. Jongbloed, **U. Martin**, **H. Antelmann**, **M. Hecker**, **H. Tjalsma**, **G. Venema**, **S. Bron**, **J. M. van Dijl**, and **J. Müller**. TatC is a specificity determinant for protein secretion via the twin-arginine translocation path-

way. *J Biol Chem*, **275**(52):41350–41357, **2000**. doi:10.1074/jbc.M004887200. 17

Jan D H Jongbloed, **Ulrike Grieger**, **Haike Antelmann**, **Michael Hecker**, **Reindert Nijland**, **Sierd Bron**, and **Jan Maarten van Dijl**. Two minimal Tat translocases in *Bacillus*. *Mol Microbiol*, **54**(5):1319–1325, **2004**. doi:10.1111/j.1365-2958.2004.04341.x. 17, 18

K. Keegstra and **K. Cline**. Protein import and routing systems of chloroplasts. *Plant Cell*, **11**(4):557–570, **1999**. 4, 5

Sophie De Keersmaeker, **Lieve Van Mellaert**, **Elke Lammertyn**, **Kristof Vrancken**, **Jozef Anné**, and **Nick Geukens**. Functional analysis of TatA and TatB in *Streptomyces lividans*. *Biochem Biophys Res Commun*, **335**(3):973–982, **2005**. doi:10.1016/j.bbrc.2005.07.165. 18

Helmut Kirchhoff. Significance of protein crowding, order and mobility for photosynthetic membrane functions. *Biochem Soc Trans*, **36**(Pt 5):967–970, **2008**. doi:10.1042/BST0360967. 34

U. Kubitscheck, **P. Wedekind**, and **R. Peters**. Three-dimensional diffusion measurements by scanning microphotolysis. *J Microsc*, **192**(Pt 2):126–138, **1998**. 28

R. H. Köhler, **P. Schwille**, **W. W. Webb**, and **M. R. Hanson**. Active protein transport through plastid tubules: velocity quantified by fluorescence correlation spectroscopy. *J Cell Sci*, **113 (Pt 22)**:3921–3930, **2000**. 34

J. R. Lakowicz, **H. Szmacinski**, **K. Nowaczyk**, **K. W. Berndt**, and **M. Johnson**. Fluorescence lifetime imaging. *Anal Biochem*, **202**(2):316–330, **1992**. 23

P. Lancaster and **K. Salkauskas**. Surfaces generated by moving least squares methods. *Math Comput*, **37**(155):141–158, **1981**. 37

Philip A Lee, **Grant Buchanan**, **Nicola R Stanley**, **Ben C Berks**, and **Tracy Palmer**. Truncation analysis of TatA and TatB defines the minimal functional units required for protein translocation. *J Bacteriol*, **184**(21):5871–5879, **2002**. 8

Erik de Leeuw, **Thierry Granjon**, **Ida Porcelli**, **Meriem Alami**, **Stephen B Carr**, **Matthias Müller**, **Frank Sargent**, **Tracy Palmer**, and **Ben C Berks**. Oligomeric properties and signal peptide binding by *Escherichia coli* Tat protein transport complexes. *J Mol Biol*, **322**(5):1135–1146, **2002**. 14

Dario Leister. Chloroplast research in the genomic age. *Trends Genet*, **19**(1):47–56, **2003**. 3

Shaofan Li and **Wing Kam Liu**. Meshfree and particle methods and their applications. *Appl Mech Rev*, **55**(1):1–34, **2002**. doi:10.1115/1.1431547. 30, 31

Ute Lindenstrauss, **Cristina F R O Matos**, **Wenke Graubner**, **Colin Robinson**, and **Thomas Brüser**. Malfolded recombinant Tat substrates are Tat-

independently degraded in *Escherichia coli*. *FEBS Lett*, **584**(16):3644–3648, **2010**. doi:10.1016/j.febslet.2010.07.039. 11

J. Lippincott-Schwartz, **E. Snapp**, and **A. Kenworthy**. Studying protein dynamics in living cells. *Nat Rev Mol Cell Biol*, **2**(6):444–456, **2001**. doi: 10.1038/35073068. 21

Wing Kam Liu, **Sukky Jun**, **Shaofan Li**, **Jonathan Adee**, and **Ted Belytschko**. Reproducing kernel particle methods for structural dynamics. *Int J Numer Meth Eng*, **38**:1655–1679, **1995**. 32, 37

A. Lopez, **L. Dupou**, **A. Altibelli**, **J. Trotard**, and **J. F. Tocanne**. Fluorescence recovery after photobleaching (FRAP) experiments under conditions of uniform disk illumination. Critical comparison of analytical solutions, and a new mathematical method for calculation of diffusion coefficient D. *Biophys J*, **53**(6):963–970, **1988**. 27, 28

Brian Luft, **Vadim Shapiro**, and **Igor Tsukanov**. Geometrically adaptive numerical integration. In *Proceedings of the 2008 ACM Symposium on Solid and Physical Modeling.*, pages 147–157. ACM New York, NY, USA, **2008**. ISBN 978-1-60558-106-2. doi:10.1145/1364901.1364923. 111

X. Ma and **K. Cline**. Precursors bind to specific sites on thylakoid membranes prior to transport on the ΔpH protein translocation system. *J Biol Chem*, **275**(14):10016–10022, **2000**. 12, 13, 15

S. Maiti, **U. Haupts**, and **W. W. Webb**. Fluorescence correlation spectroscopy: diagnostics for sparse molecules. *Proc Natl Acad Sci U S A*, **94**(22):11753–11757, **1997**. 23

A. Mant, **I. Schmidt**, **R. G. Herrmann**, **C. Robinson**, and **R. B. Klösgen**. Sec-dependent thylakoid protein translocation. ΔpH requirement is dictated by passenger protein and ATP concentration. *J Biol Chem*, **270**(40):23275–23281, **1995**. 6

J. P. Marques, **I. Dudeck**, and **R. B. Klösgen**. Targeting of EGFP chimeras within chloroplasts. *Mol Genet Genomics*, **269**(3):381–387, **2003**. doi: 10.1007/s00438-003-0846-y. 26, 67

João Pedro Marques, **Martin Hartmut Schattat**, **Gerd Hause**, **Ingrid Dudeck**, and **Ralf Bernd Klösgen**. *In vivo* transport of folded EGFP by the ΔpH/TAT-dependent pathway in chloroplasts of *Arabidopsis thaliana*. *J Exp Bot*, **55**(403):1697–1706, **2004**. doi:10.1093/jxb/erh191. 26, 67

Cristina F R O Matos, **Alessandra Di Cola**, and **Colin Robinson**. TatD is a central component of a Tat translocon-initiated quality control system for exported FeS proteins in *Escherichia coli*. *EMBO Rep*, **10**(5):474–479, **2009**. doi:10.1038/embor.2009.34. 11

Cristina F R O Matos, **Colin Robinson**, and **Alessandra Di Cola**. The Tat system proofreads FeS protein substrates and directly initiates the disposal of rejected molecules. *EMBO J*, **27**(15):2055–2063, **2008**. doi:

10.1038/emboj.2008.132. 11

Christopher A McDevitt, **Grant Buchanan**, **Frank Sargent**, **Tracy Palmer**, and **Ben C Berks**. Subunit composition and *in vivo* substrate-binding characteristics of *Escherichia coli* Tat protein complexes expressed at native levels. *FEBS J*, **273**(24):5656–5668, **2006**. doi:10.1111/j.1742-4658.2006.05554.x. 14

J. M. Melenk and **I. Babuška**. The partition of unity finite element method: basic theory and applications. *Comput. Methods Appl. Mech. Engrg.*, **139**:289–314, **1996**. doi:doi:10.1016/S0045-7825(96)01087-0. 32, 37, 38

Jens Markus Melenk. *On Generalized Finite Element Methods*. Ph.D. thesis, The University of Maryland, **1995**. 32, 38

Miguel San Miguel, **Rachel Marrington**, **P. Mark Rodger**, **Alison Rodger**, and **Colin Robinson**. An *Escherichia coli* twin-arginine signal peptide switches between helical and unstructured conformations depending on the hydrophobicity of the environment. *Eur J Biochem*, **270**(16):3345–3352, **2003**. 14

J. J. Monaghan. An introduction to SPH. *Computer Physics Communications*, **48**(1):89–96, **1988**. doi:10.1016/0010-4655(88)90026-4. 32

H. Mori, **E. J. Summer**, and **K. Cline**. Chloroplast TatC plays a direct role in thylakoid ΔpH-dependent protein transport. *FEBS Lett*, **501**(1):65–68, **2001**. 8

Hiroki Mori and **Kenneth Cline**. A twin arginine signal peptide and the pH gradient trigger reversible assembly of the thylakoid ΔpH/Tat translocase. *J Cell Biol*, **157**(2):205–210, **2002**. doi:10.1083/jcb.200202048. 14, 15

R. M. Mould and **C. Robinson**. A proton gradient is required for the transport of two lumenal oxygen-evolving proteins across the thylakoid membrane. *J Biol Chem*, **266**(19):12189–12193, **1991**. 26

R. M. Mould, **J. B. Shackleton**, and **C. Robinson**. Transport of proteins into chloroplasts. Requirements for the efficient import of two lumenal oxygen-evolving complex proteins into isolated thylakoids. *J Biol Chem*, **266**(26):17286–17289, **1991**a. 5

Ruth M. Mould, **Jamie B. Shackleton**, and **Colin Robinson**. Transport of proteins into chloroplasts. *The Journal of Biological Chemistry*, **266**(26):17286–17289, **1991**b. 4, 26

Conrad W Mullineaux, **Anja Nenninger**, **Nicola Ray**, and **Colin Robinson**. Diffusion of green fluorescent protein in three cell environments in *Escherichia coli*. *J Bacteriol*, **188**(10):3442–3448, **2006**. doi:10.1128/JB.188.10.3442-3448.2006. 26, 34, 67

B. Nayroles, **G. Touzot**, and **P. Villon**. Generalizing the finite element method: diffuse approximation and diffuse elements. *Comput. Mech.*,

10(5):307–318, **1992**. doi:10.1007/BF00364252. 32, 37

Walter Neupert and **Johannes M Herrmann**. Translocation of proteins into mitochondria. *Annu Rev Biochem*, **76**:723–749, **2007**. doi:10.1146/annurev.biochem.76.052705.163409. 3

W. V. Ng, **S. P. Kennedy**, **G. G. Mahairas**, **B. Berquist**, **M. Pan**, **H. D. Shukla**, **S. R. Lasky**, **N. S. Baliga**, **V. Thorsson**, **J. Sbrogna**, **S. Swartzell**, **D. Weir**, **J. Hall**, **T. A. Dahl**, **R. Welti**, **Y. A. Goo**, **B. Leithauser**, **K. Keller**, **R. Cruz**, **M. J. Danson**, **D. W. Hough**, **D. G. Maddocks**, **P. E. Jablonski**, **M. P. Krebs**, **C. M. Angevine**, **H. Dale**, **T. A. Isenbarger**, **R. F. Peck**, **M. Pohlschroder**, **J. L. Spudich**, **K. W. Jung**, **M. Alam**, **T. Freitas**, **S. Hou**, **C. J. Daniels**, **P. P. Dennis**, **A. D. Omer**, **H. Ebhardt**, **T. M. Lowe**, **P. Liang**, **M. Riley**, **L. Hood**, and **S. DasSarma**. Genome sequence of *Halobacterium* species NRC-1. *Proc Natl Acad Sci U S A*, **97**(22):12176–12181, **2000**. doi:10.1073/pnas.190337797. 18

Joanne Oates, **Claire M L Barrett**, **James P Barnett**, **Katheryne G Byrne**, **Albert Bolhuis**, and **Colin Robinson**. The *Escherichia coli* twin-arginine translocation apparatus incorporates a distinct form of TatABC complex, spectrum of modular TatA complexes and minor TatAB complex. *J Mol Biol*, **346**(1):295–305, **2005**. doi:10.1016/j.jmb.2004.11.047. 13, 14, 15

J. Tinsley Oden. Historical comments on finite elements. In *Proceedings of the ACM conference on history of scientific and numerical computation*, pages 125–130. Association for Computing Machinery, ACM New York, NY, USA, **1987**. ISBN 0-89791-229-2. 31

OpenMP. *OpenMP Application Program Interface. Version 3.0*. OpenMP Architecture Review Board, **2008**. 64

A. Partikian, **B. Olveczky**, **R. Swaminathan**, **Y. Li**, and **A. S. Verkman**. Rapid diffusion of green fluorescent protein in the mitochondrial matrix. *J Cell Biol*, **140**(4):821–829, **1998**. 34

George H Patterson and **Jennifer Lippincott-Schwartz**. A photoactivatable GFP for selective photolabeling of proteins and cells. *Science*, **297**(5588):1873–1877, **2002**. doi:10.1126/science.1074952. 22

E. Pedrazzini, **G. Giovinazzo**, **A. Bielli**, **M. de Virgilio**, **L. Frigerio**, **M. Pesca**, **F. Faoro**, **R. Bollini**, **A. Ceriotti**, and **A. Vitale**. Protein quality control along the route to the plant vacuole. *Plant Cell*, **9**(10):1869–1880, **1997**. doi:10.1105/tpc.9.10.1869. 57

Emanuela Pedrazzini, **Giovanna Giovinazzo**, **Roberto Bollini**, **Aldo Ceriotti**, and **Allessandro Vitale**. Binding of BiP to an assembly-defective protein in plant cells. *The Plant Journal*, **5**(1):103–110, **1994**. 55, 56

N. Periasamy and **A. S. Verkman**. Analysis of fluorophore diffusion by continuous distributions of diffusion coefficients: application to photobleaching measurements of multicomponent and anomalous diffusion.

Biophys J, **75**(1):557–567, **1998**. 35

R. Peters, **J. Peters**, **K. H. Tews**, and **W. Bühr**. A microfluorimetric study of translational diffusion in erythrocyte membranes. *Biochim Biophys Acta*, **367**(3):282–294, **1974**. 22, 27, 28

Reiner Peters, **Axel Brünger**, and **Klaus Schulten**. Continuous fluorescence microphotolysis: a sensitive method for study of diffusion processes in single cells. *Proc Natl Acad Sci U S A*, **78**(2):962–966, **1981**. 23, 27, 29

Ovidiu I Pop, **Martin Westermann**, **Rudolf Volkmer-Engert**, **Daniela Schulz**, **Cornelius Lemke**, **Sandra Schreiber**, **Roman Gerlach**, **Reinhard Wetzker**, and **Jörg P Müller**. Sequence-specific binding of prePhoD to soluble TatAd indicates protein-mediated targeting of the Tat export in *Bacillus subtilis*. *J Biol Chem*, **278**(40):38428–38436, **2003**. doi: 10.1074/jbc.M306516200. 18

Ida Porcelli, **Erik de Leeuw**, **Russell Wallis**, **Els van den Brink-van der Laan**, **Ben de Kruijff**, **B. A. Wallace**, **Tracy Palmer**, and **Ben C Berks**. Characterization and membrane assembly of the TatA component of the *Escherichia coli* twin-arginine protein transport system. *Biochemistry*, **41**(46):13690–13697, **2002**. 14, 16

Thomas J Pucadyil and **Amitabha Chattopadhyay**. Confocal fluorescence recovery after photobleaching of green fluorescent protein in solution. *J Fluoresc*, **16**(1):87–94, **2006**. doi:10.1007/s10895-005-0019-y. 34

H. L. Race, **R. G. Herrmann**, and **W. Martin**. Why have organelles retained genomes? *Trends Genet*, **15**(9):364–370, **1999**. 3

Nicola Ray, **Joanne Oates**, **Raymond J Turner**, and **Colin Robinson**. DmsD is required for the biogenesis of DMSO reductase in *Escherichia coli* but not for the interaction of the DmsA signal peptide with the Tat apparatus. *FEBS Lett*, **534**(1-3):156–160, **2003**. 163

C. Robinson and **A. Bolhuis**. Protein targeting by the twin-arginine translocation pathway. *Nat Rev Mol Cell Biol*, **2**(5):350–356, **2001**. doi: 10.1038/35073038. 12, 19

C. Robinson and **R. B. Klösgen**. Targeting of proteins into and across the thylakoid membrane–a multitude of mechanisms. *Plant Mol Biol*, **26**(1):15–24, **1994**. 5

Colin Robinson and **Albert Bolhuis**. Tat-dependent protein targeting in prokaryotes and chloroplasts. *Biochim Biophys Acta*, **1694**(1-3):135–147, **2004**. doi:10.1016/j.bbamcr.2004.03.010. 14

A. Rodrigue, **A. Chanal**, **K. Beck**, **M. Müller**, and **L. F. Wu**. Co-translocation of a periplasmic enzyme complex by a hitchhiker mechanism through the bacterial Tat pathway. *J Biol Chem*, **274**(19):13223–13228, **1999**. 9, 10

R. Wesley Rose, **Thomas Brüser**, **Jessica C Kissinger**, and **Mechthild Pohlschröder**. Adaptation of protein secretion to extremely high-salt conditions by extensive use of the twin-arginine translocation pathway. *Mol Microbiol*, **45**(4):943–950, **2002**. 19

Youcef Saad and **Martin H. Schultz**. GMRES: a generalized minimal residual algorithm for solving nonsymmetric linear systems. *SIAM J Sci Stat Comput*, **7**(3):856–859, **1986**. 115

C. L. Santini, **B. Ize**, **A. Chanal**, **M. Müller**, **G. Giordano**, and **L. F. Wu**. A novel sec-independent periplasmic protein translocation pathway in *Escherichia coli*. *EMBO J*, **17**(1):101–112, **1998**. doi:10.1093/emboj/17.1.101. 9, 10

F. Sargent, **E. G. Bogsch**, **N. R. Stanley**, **M. Wexler**, **C. Robinson**, **B. C. Berks**, and **T. Palmer**. Overlapping functions of components of a bacterial Sec-independent protein export pathway. *EMBO J*, **17**(13):3640–3650, **1998**. doi:10.1093/emboj/17.13.3640. 7, 8

F. Sargent, **U. Gohlke**, **E. De Leeuw**, **N. R. Stanley**, **T. Palmer**, **H. R. Saibil**, and **B. C. Berks**. Purified components of the *Escherichia coli* Tat protein transport system form a double-layered ring structure. *Eur J Biochem*, **268**(12):3361–3367, **2001**. 13

F. Sargent, **N. R. Stanley**, **B. C. Berks**, and **T. Palmer**. Sec-independent protein translocation in *Escherichia coli*. A distinct and pivotal role for the TatB protein. *J Biol Chem*, **274**(51):36073–36082, **1999**. 12, 13

Ivo F Sbalzarini, **Arnold Hayer**, **Ari Helenius**, and **Petros Koumoutsakos**. Simulations of (an)isotropic diffusion on curved biological surfaces. *Biophys J*, **90**(3):878–885, **2006**. doi:10.1529/biophysj.105.073809. 36

Ivo F Sbalzarini, **Anna Mezzacasa**, **Ari Helenius**, and **Petros Koumoutsakos**. Effects of organelle shape on fluorescence recovery after photobleaching. *Biophys J*, **89**(3):1482–1492, **2005**. doi:10.1529/biophysj.104.057885. 22, 36

T. G. Schmidt, **J. Koepke**, **R. Frank**, and **A. Skerra**. Molecular interaction between the Strep-tag affinity peptide and its cognate target, Streptavidin. *J Mol Biol*, **255**(5):753–766, **1996**. doi:1006/jmbi.1996.0061. 163

Martin H. Schultz. Rayleigh-Ritz-Galerkin methods for multidimensional problems. *SIAM J. Numer. Anal.*, **6**(4):523–538, **1969**. 45

Danja Schünemann. Mechanisms of protein import into thylakoids of chloroplasts. *Biol Chem*, **388**(9):907–915, **2007**. doi:10.1515/BC.2007.111. 67

M. A. Schweitzer. *A parallel multilevel partition of unity method for elliptic partial differential equations.*, volume 29 of *Lecture Notes in Computational Science and Engineering*. Springer, **2003**. 39

M. A. Schweitzer. An algebraic treatment of essential boundary conditions

in the particle-partition of unity method. *SIAM J Sci Comp*, **2008**a. 39

M. A. Schweitzer. A particle-partition of unity method – Part VIII: hierarchical enrichment. In *Lecture Notes in Computational Science and Engineering*, volume 65, pages 277–299. Springer, **2008**b. 39

Marc Alexander Schweitzer. An adaptive *hp*-version of the multilevel particle-partition of unity method. *Comput. Methods Appl. Mech. Engrg.*, **2008**c. doi:10.1016/j.cma.2008.01.009. 39

A. M. Settles and **R. Martienssen**. Old and new pathways of protein export in chloroplasts and bacteria. *Trends Cell Biol*, **8**(12):494–501, **1998**. 8

A. M. Settles, **A. Yonetani**, **A. Baron**, **D. R. Bush**, **K. Cline**, and **R. Martienssen**. Sec-independent protein translocation by the maize Hcf106 protein. *Science*, **278**(5342):1467–1470, **1997**. 7, 16

Anitha Shanmugham, **Harro W Wong Fong Sang**, **Yves J M Bollen**, and **Holger Lill**. Membrane binding of twin arginine preproteins as an early step in translocation. *Biochemistry*, **45**(7):2243–2249, **2006**. doi:10.1021/bi052188a. 15

Donald Shepard. A two-dimensional interpolation function for irregularly-spaced data. In *Proceedings of the 1968 23rd ACM National Conference*, pages 517–524. Association for Computing Machinery, Association for Computing Machinery, **1968**. doi:10.1145/800186.810616. 37, 40

E. D. Siggia, **J. Lippincott-Schwartz**, and **S. Bekiranov**. Diffusion in inhomogeneous media: theory and simulations applied to whole cell photobleach recovery. *Biophys J*, **79**(4):1761–1770, **2000**. 153

Jürgen Soll and **Enrico Schleiff**. Protein import into chloroplasts. *Nat Rev Mol Cell Biol*, **5**(3):198–208, **2004**. doi:10.1038/nrm1333. 3

D. M. Soumpasis. Theoretical analysis of fluorescence photobleaching recovery experiments. *Biophys J*, **41**(1):95–97, **1983**. 22, 28

Edward Spence, **Mary Sarcina**, **Nicola Ray**, **Simon Geir Møller**, **Conrad W. Mullineaux**, and **Colin Robinson**. Membrane-specific targeting of green fluorescent protein by the Tat pathway in the cyanobacterium *Synechocystis* PCC6803. *Molecular Microbiology*, **48**(6):1481–1489, **2003**. 26

L. Andrew Staehelin. Chloroplast structure: from chlorophyll granules to supra-molecular architecture of thylakoid membranes. *Photosynth Res*, **76**(1-3):185–196, **2003**. doi:10.1023/A:1024994525586. 3

N. R. Stanley, **T. Palmer**, and **B. C. Berks**. The twin arginine consensus motif of Tat signal peptides is involved in Sec-independent protein targeting in escherichia coli. *J Biol Chem*, **275**(16):11591–11596, **2000**. 7

Gilbert Strang and **George J. Fix**. *An analysis of the finite element method.* Series in Automatic Computation. Prentice-Hall, **1973**. 31, 43, 44

S. Subramani, **A. Koller**, and **W. B. Snyder**. Import of peroxisomal matrix and membrane proteins. *Annu Rev Biochem*, **69**:399–418, **2000**. doi:10.1146/annurev.biochem.69.1.399. 3

M. Sugiura. The chloroplast chromosomes in land plants. *Annu Rev Cell Biol*, **5**:51–70, **1989**. doi:10.1146/annurev.cb.05.110189.000411. 3

E. J. Summer, **H. Mori**, **A. M. Settles**, and **K. Cline**. The thylakoid ΔpH-dependent pathway machinery facilitates RR-independent N-tail protein integration. *J Biol Chem*, **275**(31):23483–23490, **2000**. doi:10.1074/jbc.M004137200. 12

R. Swaminathan, **C. P. Hoang**, and **A. S. Verkman**. Photobleaching recovery and anisotropy decay of green fluorescent protein GFP-S65T in solution and cells: cytoplasmic viscosity probed by green fluorescent protein translational and rotational diffusion. *Biophys J*, **72**(4):1900–1907, **1997**. 34

B. R. Terry, **E. K. Matthews**, and **J. Haseloff**. Molecular characterisation of recombinant green fluorescent protein by fluorescence correlation microscopy. *Biochem Biophys Res Commun*, **217**(1):21–27, **1995**. 34

Joanna D. Thomas, **Richard A. Daniel**, **Jeff Errington**, and **Colin Robinson**. Export of active green fluorescent protein to the periplasm by the twin-arginine translocase (Tat) pathway in *Escherichia coli*. *Molecular Microbiology*, **39**(1):47–53, **2001**. 26, 67

Lloyd N. Trefethen and **David Bau III**. *Numerical Linear Algebra*. SIAM, **1997**. ISBN 0-89871-361-7. 115

R. Y. Tsien. The green fluorescent protein. *Annu Rev Biochem*, **67**:509–544, **1998**. doi:10.1146/annurev.biochem.67.1.509. 21

R. Voelker and **A. Barkan**. Two nuclear mutations disrupt distinct pathways for targeting proteins to the chloroplast thylakoid. *EMBO J*, **14**(16):3905–3914, **1995**. 7

Lea Vojta, **Jürgen Soll**, and **Bettina Bölter**. Protein transport in chloroplasts – targeting to the intermembrane space. *FEBS J*, **274**(19):5043–5054, **2007**. doi:10.1111/j.1742-4658.2007.06023.x. 4

Malte Wachsmuth, **Thomas Weidemann**, **Gabriele Müller**, **Urs W. Hoffmann-Rohrer**, **Tobias A. Knoch**, **Waldemar Waldeck**, and **Jörg Langowski**. Analyzing intracellular binding and diffusion with continuous fluorescence photobleaching. *Biophys J*, **84**(5):3353–3363, **2003**. 29, 36

M. B. Walker, **L. M. Roy**, **E. Coleman**, **R. Voelker**, and **A. Barkan**. The maize *tha4* gene functions in Sec-independent protein transport in chloroplasts and is related to *hcf106*, *tatA*, and *tatB*. *J Cell Biol*, **147**(2):267–276, **1999**. 7, 16

Michael Walter, **Christina Chaban**, **Katia Schütze**, **Oliver Batistic**, **Katrin Weckermann**, **Christian Näke**, **Dragica Blazevic**, **Christopher Grefen**,

Karin Schumacher, **Claudia Oecking**, **Klaus Harter**, and **Jörg Kudla**. Visualization of protein interactions in living plant cells using bimolecular fluorescence complementation. *Plant J*, **40**(3):428–438, **2004**. doi: 10.1111/j.1365-313X.2004.02219.x. 24

P. Wedekind, **U. Kubitscheck**, **O. Heinrich**, and **R. Peters**. Line-scanning microphotolysis for diffraction-limited measurements of lateral diffusion. *Biophys J*, **71**(3):1621–1632, **1996**. 27

J. H. Weiner, **P. T. Bilous**, **G. M. Shaw**, **S. P. Lubitz**, **L. Frost**, **G. H. Thomas**, **J. A. Cole**, and **R. J. Turner**. A novel and ubiquitous system for membrane targeting and secretion of cofactor-containing proteins. *Cell*, **93**(1):93–101, **1998**. 7

J. H. Weiner, **R. A. Rothery**, **D. Sambasivarao**, and **C. A. Trieber**. Molecular analysis of dimethylsulfoxide reductase: a complex iron-sulfur molybdoenzyme of *Escherichia coli*. *Biochim Biophys Acta*, **1102**(1):1–18, **1992**. 163

Matthias Weiss. Challenges and artifacts in quantitative photobleaching experiments. *Traffic*, **5**(9):662–671, **2004**. doi:10.1111/j.1600-0854.2004.00215.x. 35

Martin Westermann, **Ovidiu I Pop**, **Roman Gerlach**, **Thomas R Appel**, **Wiebke Schlörmann**, **Sandra Schreiber**, and **Jörg P Müller**. The TatAd component of the *Bacillus subtilis* twin-arginine protein transport system forms homo-multimeric complexes in its cytosolic and membrane embedded localisation. *Biochim Biophys Acta*, **1758**(4):443–451, **2006**. doi: 10.1016/j.bbamem.2006.03.018. 18

M. Wexler, **F. Sargent**, **R. L. Jack**, **N. R. Stanley**, **E. G. Bogsch**, **C. Robinson**, **B. C. Berks**, and **T. Palmer**. TatD is a cytoplasmic protein with DNase activity. No requirement for TatD family proteins in sec-independent protein export. *J Biol Chem*, **275**(22):16717–16722, **2000**. doi:10.1074/jbc.M000800200. 8

J. White and **E. Stelzer**. Photobleaching GFP reveals protein dynamics inside live cells. *Trends Cell Biol*, **9**(2):61–65, **1999**. 21

William Wickner and **Randy Schekman**. Protein translocation across biological membranes. *Science*, **310**(5753):1452–1456, **2005**. doi:10.1126/science.1113752. 3

David A Widdick, **Robyn T Eijlander**, **Jan Maarten van Dijl**, **Oscar P Kuipers**, and **Tracy Palmer**. A facile reporter system for the experimental identification of twin-arginine translocation (Tat) signal peptides from all kingdoms of life. *J Mol Biol*, **375**(3):595–603, **2008**. doi:10.1016/j.jmb.2007.11.002. 17

L. F. Wu, **B. Ize**, **A. Chanal**, **Y. Quentin**, and **G. Fichant**. Bacterial twin-arginine signal peptide-dependent protein translocation pathway: evo-

lution and mechanism. *J Mol Microbiol Biotechnol*, **2**(2):179–189, **2000**. 17

Ming-Ren Yen, **Yi-Hsiung Tseng**, **Erin H Nguyen**, **Long-Fe Wu**, and **Milton H Saier**. Sequence and phylogenetic analyses of the twin-arginine targeting (Tat) protein export system. *Arch Microbiol*, **177**(6):441–450, **2002**. doi:10.1007/s00203-002-0408-4. 17

O. C. Zienkiewicz, **R. L. Taylor**, and **J. Z. Zhu**. *The Finite Element Method: Its Basis and Fundamentals.* Elsevier Butterworth-Heinemann, sixth edition, **2006**. ISBN 0-7506-6320-0. 31, 43, 44